

UNIVERSITÄT OSNABRÜCK

---

**Electronic, optical and transport properties  
of ultrathin cobalt ferrite films on MgO(001)**

---

A thesis submitted in partial fulfilment of the requirements for the degree of

*Master of Science in Physics*

Author: Sven BERLEKAMP

Matriculation Number: 959295

First Examiner: Prof. Dr. Joachim WOLLSCHLÄGER

Second Examiner: Dr. Karsten KÜPPER

August 17, 2021



# Contents

|          |   |           |
|----------|---|-----------|
| <b>1</b> | <b>Introduction</b>   | <b>1</b>  |
| <b>2</b> | <b>Theoretical background</b>                               | <b>3</b>  |
| 2.1      | Crystal structure . . . . .                                 | 3         |
| 2.1.1    | Reciprocal lattice . . . . .                                | 5         |
| 2.1.2    | Planes and directions . . . . .                             | 6         |
| 2.1.3    | Film growth and reactive molecular beam epitaxy . . . . .   | 7         |
| 2.2      | Low energy electron diffraction - LEED . . . . .            | 8         |
| 2.3      | Photoelectron spectroscopy - PES . . . . .                  | 10        |
| 2.3.1    | Basics of XPS . . . . .                                     | 10        |
| 2.3.2    | Spectra and features . . . . .                              | 11        |
| 2.3.3    | Quantitative analysis and intensity equations . . . . .     | 13        |
| 2.4      | Transport mechanisms in semiconductors . . . . .            | 14        |
| 2.4.1    | Localized states . . . . .                                  | 14        |
| 2.4.2    | Temperature-dependent transport mechanisms . . . . .        | 15        |
| 2.5      | Thin film optics . . . . .                                  | 17        |
| 2.5.1    | Direct and indirect band gaps . . . . .                     | 18        |
| 2.5.2    | Tauc plots . . . . .  | 19        |
| 2.5.3    | X-ray reflectivity - XRR . . . . .                          | 21        |
| <b>3</b> | <b>Material system</b>                                      | <b>23</b> |
| 3.1      | Magnesium oxide - MgO . . . . .                             | 23        |
| 3.2      | Cobalt ferrite - CoFe <sub>2</sub> O <sub>4</sub> . . . . . | 23        |
| <b>4</b> | <b>Experimental setup</b>                                   | <b>27</b> |
| 4.1      | Ultra high vacuum system . . . . .                          | 27        |
| 4.2      | Sample preparation . . . . .                                | 28        |
| 4.3      | XPS setup . . . . .   | 29        |
| 4.4      | LEED setup . . . . .  | 30        |
| 4.5      | XRR setup . . . . .   | 31        |
| 4.6      | UV-Vis setup . . . . .                                      | 31        |
| 4.7      | Van der Pauw setup . . . . .                                | 32        |

|          |   |           |
|----------|---|-----------|
| <b>5</b> | <b>Properties of ultrathin <math>\text{Co}_x\text{Fe}_{3-x}\text{O}_4</math> films on <math>\text{MgO}(001)</math> depending on the Co content <math>x</math></b> | <b>35</b> |
| 5.1      | XPS results . . . . .   | 35        |
| 5.1.1    | Analysis of the Fe 3p and Co 3p core-level spectra . . . . .  | 35        |
| 5.1.2    | Qualitative analysis of the Fe 2p core-level spectra . . . . .  | 37        |
| 5.1.3    | Qualitative analysis of the Co 2p core-level spectra . . . . .  | 39        |
| 5.1.4    | Qualitative analysis of the valence band . . . . .  | 40        |
| 5.2      | LEED results . . . . .  | 42        |
| 5.3      | XRR results . . . . .   | 43        |
| 5.4      | UV-Vis results . . . . .  | 45        |
| 5.4.1    | Determination of direct and indirect band transitions . . . . .   | 46        |
| 5.5      | Temperature dependent sheet resistivity . . . . .   | 49        |
| 5.5.1    | Hopping mechanisms . . . . .  | 51        |
| <b>6</b> | <b>Properties of Co-rich cobalt ferrite ultrathin films depending on the <math>\text{O}_2</math> reactive atmosphere during RMBE</b>                              | <b>53</b> |
| 6.1      | XPS results . . . . .   | 53        |
| 6.2      | LEED results . . . . .  | 57        |
| 6.3      | XRR results . . . . .   | 58        |
| 6.4      | UV-Vis results . . . . .  | 58        |
| 6.5      | Temperature dependent sheet resistivity . . . . .   | 60        |
| <b>7</b> | <b>Summary and outlook</b>  | <b>61</b> |



# 1. Introduction

Cobalt ferrite is generating much interest in current research due to its promising properties, such as its semiconducting transport behaviour, its tunable optical bandgap in the visible range and its high bulk Curie temperature of 793 K [3, 44, 55]. In consequence, cobalt ferrite is widely used in a variety of applications, including magnetic sensors or magnetic tunnel junctions [36, 8]. In particular, ultrathin cobalt ferrite films are extremely interesting candidates as efficient spin-filters in spintronics [25], which is a growing field in physics that exploits the spin-dependent charge carrier transport in solids. In spintronics, therefore, not only the charge is used to transport information, but also the electron spin, thus opening up the possibility of a new generation of faster and more energy-efficient devices [9].

The spin-filter effect originates from the exchange splitting of the energy levels in the conduction band of a magnetic insulator. As a consequence, the tunnel barrier heights in spin-filters are not the same for spin-up and spin-down electrons. This in turn leads to a higher tunneling probability for either spin-up or spin-down electrons, generating a spin-polarized current [36]. Spin-filters may function with an efficiency of 100%, but so far only spin polarizations of  $-8\%$  [25] have been achieved for cobalt ferrites. In order to increase the spin-filtering efficiency of cobalt ferrite, precise knowledge of the electronic, optical and transport properties is essential.

For this reason, the properties of ultrathin cobalt ferrite films are investigated in this work. The films are grown on magnesium oxide (MgO) by reactive molecular beam epitaxy. MgO serves as a substrate due to the low lattice mismatch of  $-0.37\%$ . In addition, MgO is transparent [17], which allows optical investigations, such as UV-Vis spectroscopy. Since the properties of cobalt ferrite can vary strongly with the stoichiometry, the first part of this work investigates the properties of cobalt ferrite ultrathin films as a function of the cobalt content. Additionally, the second part of this work investigates the influence of the oxygen atmosphere during the evaporation process on the properties of Co-rich cobalt ferrite.

The thesis is divided into multiple chapters. Chapters 2 and 3 deal with the theoretical background and the material system, respectively. Thereafter, Chapter 4 describes and explains the experimental setups. In Chapter 5, the influence of the cobalt content on the properties of cobalt ferrite is investigated and discussed and in Chapter 6, the influence of the oxygen content on the properties of Co-rich cobalt ferrite is studied. Chapter 7 will then briefly summarize the main results, followed by an outlook in which further possible experiments and research are mentioned.



## 2. Theoretical background

In this chapter, the theoretical background for this thesis is briefly explained. The fundamentals of the applied measurement methods are presented, as well as the principles of electronic, optical and transport properties of solids.

### 2.1 Crystal structure

A crystal is a periodic arrangement of identical structural units. The structural unit is called basis and the arrangement rule, i.e. the way the structural units are arranged to each other, is called lattice. The basis can consist of a single atom, or even complex macromolecules.

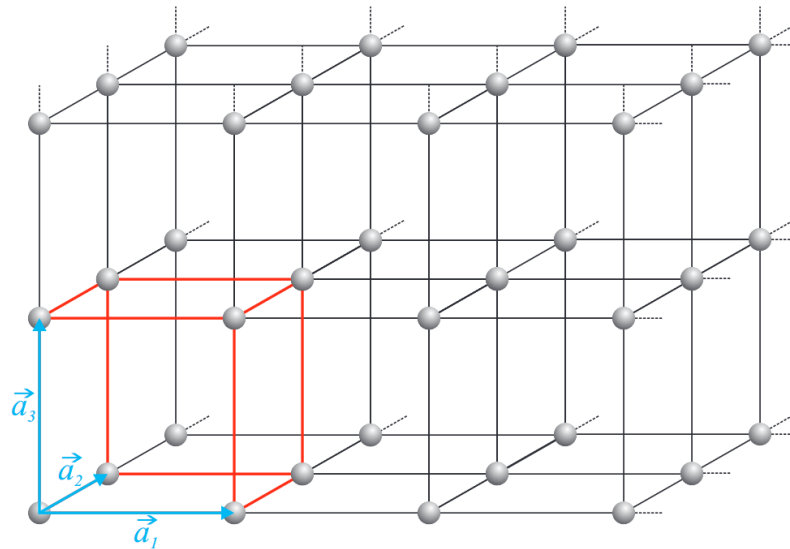


**Figure 2.1:** Schematic representation of a crystal lattice. The spheres represent a mono-atomic basis and the connecting lines represent the chemical bonds. The unit vectors  $\vec{a}_i$  (blue) define the unit cell (red). Taken from [54].

The point lattice (also called Bravais lattice) is an infinite lattice of mathematical points. Each point has the same physical properties and is invariant to translation. The point lattice is mathematically described by

$$\vec{R} = \sum_{i=1}^3 n_i \vec{a}_i, \quad (2.1)$$

where  $\vec{a}_i$  are the linear independent lattice vectors and  $n_i$  are integers. The absolute values of  $\vec{a}_i$  are called lattice constants. The lattice vectors  $\vec{a}_i$  define a parallelepiped whose volume is defined by the scalar triple product

$$V_C = (\vec{a}_1 \times \vec{a}_2) \cdot \vec{a}_3. \quad (2.2)$$

The parallelepiped is called a unit cell. If the volume of the unit cell  $V_C$  is minimal, the unit cell is called primitive. The whole crystal can be formed by translating the unit cell in the three spatial dimensions [12].

Crystalline surfaces can be considered two-dimensional objects and therefore, the corresponding lattice can sufficiently be described with only two lattice vectors  $\vec{a}_1$  and  $\vec{a}_2$ . The set of all possible integer linear combinations of these two vectors form the two-dimensional lattice, thus Eq. (2.1) can be rewritten as

$$\vec{R}_s = \sum_{i=1}^2 n_i \vec{a}_i \quad (2.3)$$

All crystalline surface structures can be divided into five main groups, called two-dimensional Bravais lattices (cf. Fig. 2.2), which are classified by the lattice vectors  $|\vec{a}_1|$  and  $|\vec{a}_2|$  and by the angle  $\theta$  between them.

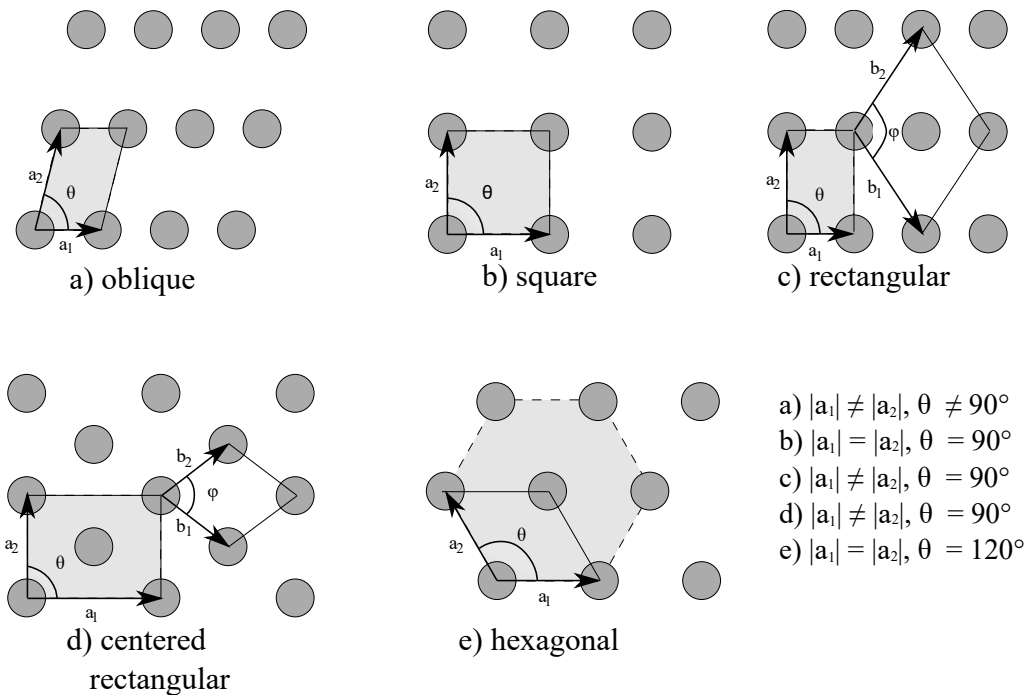


**Figure 2.2:** The five two-dimensional Bravais lattices. The spheres represent a monoatomic basis and the vectors  $\vec{a}_1$  and  $\vec{a}_2$  define the unit cell (grey). Note that there are sometimes several ways to define the unit cell.

The crystal structure of the surface may differ from the underlying structure of the bulk material. For this reason, the term superstructure is commonly used. The reason for structural deviation from the bulk is the absence of neighbouring atoms on the surface. There are unsaturated, dangling bonds,

which are energetically unfavourable. This leads to a reorganization of the surface atoms called surface reconstruction. As a result, the surface structure can no longer be described by the vectors  $\vec{a}_i$ . New vectors  $\vec{a}_i^S$  must be defined to characterize the superstructure. There are basically two notations with which superstructures can be described:

The first notation is the matrix notation, which links the vectors  $\vec{a}_i^S$  and  $\vec{a}_i$  via the matrix

$$G = \begin{pmatrix} G_{11} & G_{12} \\ G_{21} & G_{22} \end{pmatrix}. \quad (2.4)$$

Hence, the vectors  $\vec{a}_i^S$  can then be written as

$$\vec{a}_1^S = G_{11}\vec{a}_1 + G_{12}\vec{a}_2 \quad (2.5)$$

$$\vec{a}_2^S = G_{21}\vec{a}_1 + G_{22}\vec{a}_2. \quad (2.6)$$

Alternatively, the so-called Wood notation can be used to describe superstructures. In this notation, the lengths of the unit vectors of the superstructure are given as a multiple of the lengths of the unit vectors of the bulk material. A rotation angle  $\phi$  describes the rotation  $R$  of the superstructure unit vectors compared to the bulk unit vectors. The exact notation is

$$X(hkl)c(m \times n) - R\phi. \quad (2.7)$$

$X$  describes the material (e.g. Mg) and  $(hkl)$  are the Miller indices which denote the orientation of the surface (cf. Sec. 2.1.2).  $c$  is optional and indicates a possible centering of the unit cell. Note that Wood's notation can only describe superstructures whose unit vectors are rotated by the same angle with respect to the corresponding bulk unit vectors. Matrix notation, however, is applicable to all superstructures [32].

### 2.1.1 Reciprocal lattice

For the diffraction of electrons, the concept of the reciprocal lattice is of great importance since the diffraction pattern can be considered an image of the reciprocal lattice. For this reason, the basics shall be explained briefly.

The three-dimensional reciprocal lattice can be formulated analogously to Eq. (2.1) as follows:

$$\vec{G}_{hkl} = h\vec{a}_1^* + k\vec{a}_2^* + l\vec{a}_3^*. \quad (2.8)$$

Here,  $h$ ,  $k$  and  $l$  are integers  $(0, \pm 1, \pm 2, \dots)$  and  $\vec{a}_i^*$  are the unit vectors in the reciprocal space. These are related to the unit vectors in real space via

$$\vec{a}_1^* = \frac{\vec{a}_2 \times \vec{a}_3}{\vec{a}_1 \cdot (\vec{a}_2 \times \vec{a}_3)}, \quad \vec{a}_2^* = \frac{\vec{a}_3 \times \vec{a}_1}{\vec{a}_1 \cdot (\vec{a}_2 \times \vec{a}_3)} \quad \text{and} \quad \vec{a}_3^* = \frac{\vec{a}_1 \times \vec{a}_2}{\vec{a}_1 \cdot (\vec{a}_2 \times \vec{a}_3)}. \quad (2.9)$$

For two-dimensional surfaces,  $\vec{G}_{hkl}$  must be reduced by one component. Therefore Eq. (2.8) is transformed to

$$\vec{G}_{hk} = h\vec{a}_1^* + k\vec{a}_2^* \quad (2.10)$$

The calculation of the reciprocal unit vectors can then be carried out using

$$\vec{a}_1^* = \frac{\vec{a}_2 \times \vec{n}}{\vec{a}_1 \cdot (\vec{a}_2 \times \vec{n})} \quad \text{and} \quad \vec{a}_2^* = \frac{\vec{n} \times \vec{a}_1}{\vec{a}_1 \cdot (\vec{a}_2 \times \vec{n})}. \quad (2.11)$$

Here  $\vec{n}$  is the normal vector perpendicular to the surface. From these equations, it can be seen that the reciprocal vectors  $\vec{a}_1^*$  and  $\vec{a}_2^*$  lie in the same plane as the real-space vectors  $\vec{a}_1$  and  $\vec{a}_2$ . Furthermore,  $\vec{a}_1^*$  is perpendicular to  $\vec{a}_2$  and  $\vec{a}_2^*$  is perpendicular to  $\vec{a}_1$  [12].

In contrast to the three-dimensional case, where the reciprocal lattice consists of a 3D array of lattice points (Fig. 2.3 a)), the two-dimensional case lacks the vector component perpendicular to the surface. For this reason, the perpendicular vector component has a vanishing length. This means that the reciprocal lattice points perpendicular to the surface are infinitely close to each other and therefore the lattice points in real space are infinitely far apart. This results in so-called diffraction rods (Fig. 2.3 b)) [32].

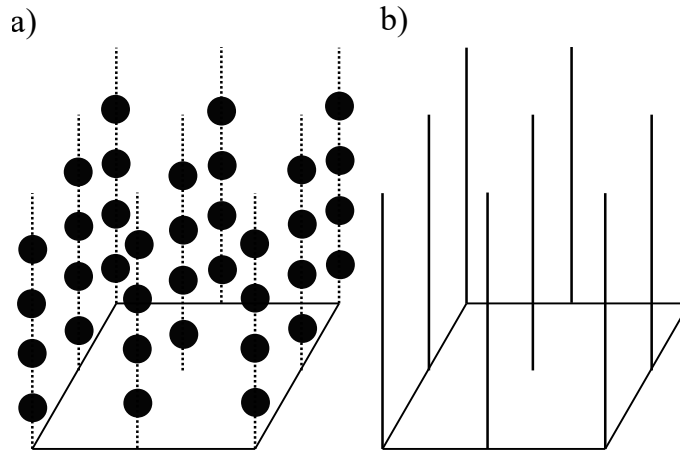


**Figure 2.3:** Reciprocal lattices for an ideal 3D crystal a) and an ideal 2D surface b)

### 2.1.2 Planes and directions

Planes and directions in the crystal are described by the so-called Miller indices. These are a triplet of numbers  $(hkl)$ , which classifies the orientation of a plane. The triple is determined as follows:

- Determine the points of intersection of the plane with the crystallographic axes in units of the lattice constants  $a_1, a_2, a_3$
- Form the reciprocal and multiply each fraction by the same number to produce the smallest possible integer triple.
- If there is no intersection with an axes, the Miller Index is 0.
- If the intersection point is in the negative range, then the corresponding index is marked with a bar above the index, e.g.  $(4\bar{2}0)$ .

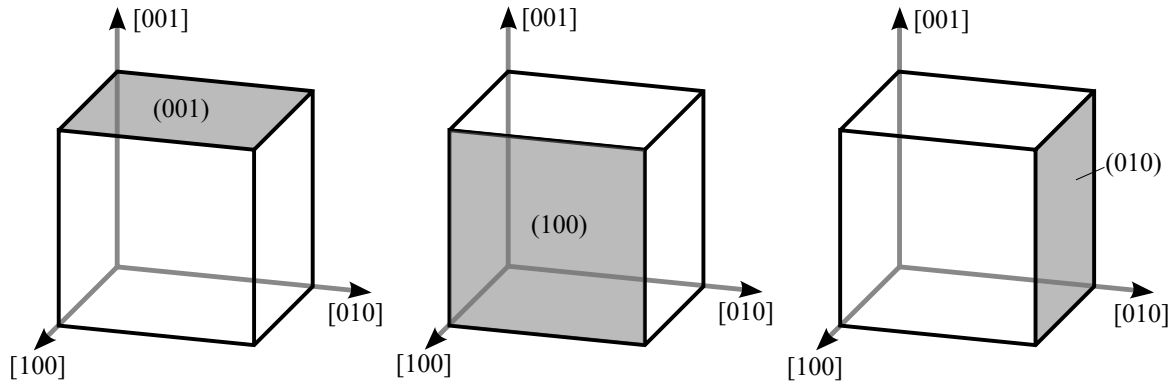


**Figure 2.4:** Examples of different planes and directions in a crystal described by their Miller indices.

Fig. 2.4 shows different crystal planes and their Miller indices. Often many planes in the crystal are equivalent. The total of all planes equivalent to  $(hkl)$  are marked with curly brackets  $\{hkl\}$ .

Directions in the crystal are also described by a triplet of numbers. Let  $\vec{R} = l\vec{a}_1 + m\vec{a}_2 + n\vec{a}_3$  be any direction in the crystal. The triplet  $[uvw]$  classifies the direction, if the triplet  $uvw$  is the smallest integer triplet with the same ratio as the vector components  $lmn$ . For instance, the Miller tuple  $[\bar{1}24]$  is associated with the crystal direction  $\vec{R} = -4\vec{a}_1 + 8\vec{a}_2 + 16\vec{a}_3$  [12].

### 2.1.3 Film growth and reactive molecular beam epitaxy

The growth of crystalline films on crystalline substrates is called epitaxy if at least one crystallographic orientation of the film corresponds to a crystallographic axis of the substrate. If film and substrate are made of the same material, it is called homoepitaxy, otherwise it is called heteroepitaxy.

Heteroepitaxy is usually accompanied by a lattice mismatch between film and substrate. The lattice mismatch  $\varepsilon$  can be described by

$$\varepsilon = \frac{a_f - a_s}{a_s}. \quad (2.12)$$

$a_f$  and  $a_s$  is the lattice constant of the film and of the substrate, respectively. There are two ways to compensate the lattice mismatch: pseudomorphic growth and growth with formation of misfit dislocations.

Small mismatches are compensated by pseudomorphic growth. The in-plane lattice periodicity of the epitaxial layer adapts to the periodicity of the substrate. Usually, this is also accompanied by a change in the lattice periodicity in the perpendicular direction. For higher lattices mismatches it is energetically more favorable to compensate the lattice mismatch by the formation of misfit dislocations. Fig. 2.5 shows schematically the pseudomorphic growth and growth accompanied by the formation of dislocations.

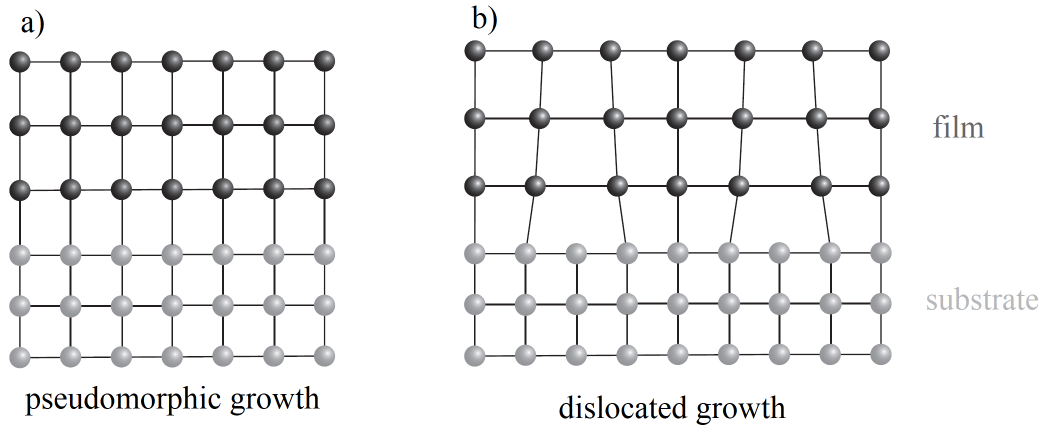


**Figure 2.5:** Schematic view of atomic arrangements in epitaxial growth modes: a) pseudomorphic, lattice matched growth and b) growth with formation of misfit dislocations. Taken and adapted from [54].

Molecular beam epitaxy (MBE) is a physical vapor deposition technique to prepare epitaxial films. A directed thermal atomic or molecular beam deposits the material onto the substrate. The process usually takes place under ultra high vacuum (UHV) conditions to prevent surface contamination. In addition, this ensures that the molecular beams can be incident on the substrate without colliding with inadvertent particles. The substrate is usually heated during evaporation, which leads to a better mobility of the particles on the surface and thus to a better surface ordering. To obtain more complex films with multiple chemical constituents, particle beams of different chemical elements can be combined. For the preparation of oxidic metal films, molecular oxygen can be let into the reaction chamber, which is then referred to as reactive molecular beam epitaxy (RMBE) [32].

## 2.2 Low energy electron diffraction - LEED

Low energy electron diffraction (LEED) is a frequently used method to study the structure and morphology of crystalline surfaces. The basis of this method is the electron wavelength, which is given by

$$\lambda_e = \frac{h}{\sqrt{2m_e E_{kin}}}. \quad (2.13)$$

Here  $h$  and  $m_e$  are the Planck constant and the electron mass, respectively.  $E_{kin}$  is the kinetic energy of the electrons. In a LEED measurement, the electrons typically have an energy between 50 eV and 300 eV, which corresponds to an electron wavelength of approximately 1 Å to 2 Å. Diffraction



phenomena occur because the electron's wavelength is of the same order of magnitude as interatomic distances. The electron waves are diffracted at the surface and subsequently the diffracted waves interfere constructively and destructively, resulting in a diffraction pattern that can be used to obtain structural information about the surface.

Due to the strong interaction of electrons and matter, the penetration depth of the electrons is only a few monolayers. Therefore, this method is well suited for structural surface examination, while bulk properties can hardly be studied as a result of the low penetration depth [32].

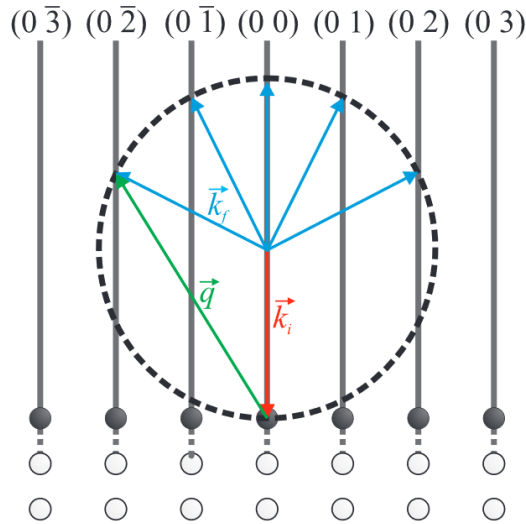


**Figure 2.6:** Ewald sphere in two dimensions. The initial electrons (red) hit the surface normally at the (00) lattice rod. The sphere (dotted line) is defined by all possible positions for the wave vector  $k_f$ . The Laue condition is fulfilled when  $k_f$  terminates on the intersection of the Ewald sphere and the diffraction rod. Taken from [23].

The diffraction pattern is the result of constructive and destructive interferences of the diffracted beams. Thus, it is in essence an intensity profile. An intensity maximum (constructive interference) occurs when the lateral Laue conditions

$$\vec{q} \cdot \vec{a}_1 = 2\pi h, \quad (2.14)$$

$$\vec{q} \cdot \vec{a}_2 = 2\pi k \quad (2.15)$$

are fulfilled. Here,  $\vec{q} = \vec{k}_i - \vec{k}_f$  is the scattering vector defined as the difference of incident wave  $\vec{k}_i$  vector and diffracted wave vector  $\vec{k}_f$ .

Under the assumption that only elastic scattering is considered, the lateral Laue conditions (Eq. (2.14)-(2.15)) can be considered a selection rule. This rule can be illustrated by the Ewald sphere (cf. Fig. 2.6). First, the reciprocal lattice rods of the crystal surface are drawn. The incident wave vector  $\vec{k}_i$  is chosen to terminate at the (00) lattice rod. The length of the wave vector is known to be  $|\vec{k}_i| = \frac{2\pi}{\lambda_e}$ . Now a sphere can be drawn along the origin of the incident wave vector with a radius of  $|\vec{k}_i|$ .

An intensity maximum occurs exactly when the sphere intersects a reciprocal lattice rod, meaning that Eq. (2.14)-(2.15) are fulfilled [12, 32].

### LEED pattern analysis

From a LEED pattern, a lot of information about the structure of the surface can be obtained. From the spot sharpness together with the background intensity conclusions can be made about the ordering of the surface atoms. Clearly defined spots with low background intensity suggest a well ordering of surface atoms. In contrast, a disordered defect-rich surface shows weak, smeared spots with high background intensity. The surface ordering can be quantified with an intensity profile along the spots. The profile can be approximated using a Lorentz function and its FWHM can be used to evaluate the width of the spots. Furthermore, the surface geometry can be analyzed. Using the arrangement of the spots, the lattice structure and also the superstructure can be determined [32].

## 2.3 Photoelectron spectroscopy - PES

Photoelectron spectroscopy (PES) is a frequently used technique to analyze the chemical composition as well as the electronic structure of surfaces and near-surface regions. Different types of PES can be distinguished according to the photon energy used for electron excitation.

Ultraviolet photoelectron spectroscopy (UPS) uses photons in the ultraviolet range (10 - 50 eV) as an excitation source. Consequently, no electrons close to the nucleus can be excited but only the weakly bonded valence electrons. For this reason, the method is particularly suitable for investigating the valence band or molecular orbitals. In Soft X-ray photoelectron spectroscopy (XPS), X-ray photons with an energy of about 100 eV to 2 keV are used to excite surface electrons. Since the excitation energy in this case is much higher than the excitation energy used in UPS, electrons close to the nucleus can also be excited, providing information about the electronic structure of the deep core levels.

Furthermore hard (high-energy) X-ray photoelectron spectroscopy (HAXPES) is another type of PES in which high-energy X-ray photons ( $E_{ph} > 2 \text{ keV}$ ) serve as an excitation source. Photoelectrons emitted in HAXPES have a higher kinetic energy and therefore a higher IMFP, resulting in a greater information depth.

Note, however, that the energy ranges are not clearly defined and the subdivision mentioned above is often a matter of convention and viewpoint [32]. In this thesis, the prepared samples are qualitatively and quantitatively examined using XPS with an excitation energy of 1253.6 eV (Mg anode) and 1486.6 eV (Al anode).

### 2.3.1 Basics of XPS

In XPS, the sample is irradiated with X-rays. If an X-ray photon hits an electron close to the nucleus, this electron can be released from the material, provided that the condition

$$h\nu \geq E_B + \theta \quad (2.16)$$

is fulfilled.  $E_B$  is the electron's binding energy and  $\theta$  is the material-specific work function.  $h\nu$  is the photon energy. The emitted photoelectrons are detected as a function of their kinetic energy, resulting in the XP spectrum. Neglecting scattering effects, the conservation of energy

$$E_{kin} = h\nu - E_B - \theta \quad (2.17)$$

holds true.  $E_{kin}$  is the electron's kinetic energy. The binding energy  $E_B$  is defined as the difference between the Fermi energy  $E_F$  of the material and the electron energy of the orbital from which the electron originates. The work function  $\theta$  is related to the vacuum energy  $E_V$  through  $\theta = E_V - E_F$  [32]. Fig. 2.7 illustrates the photoemission process schematically.

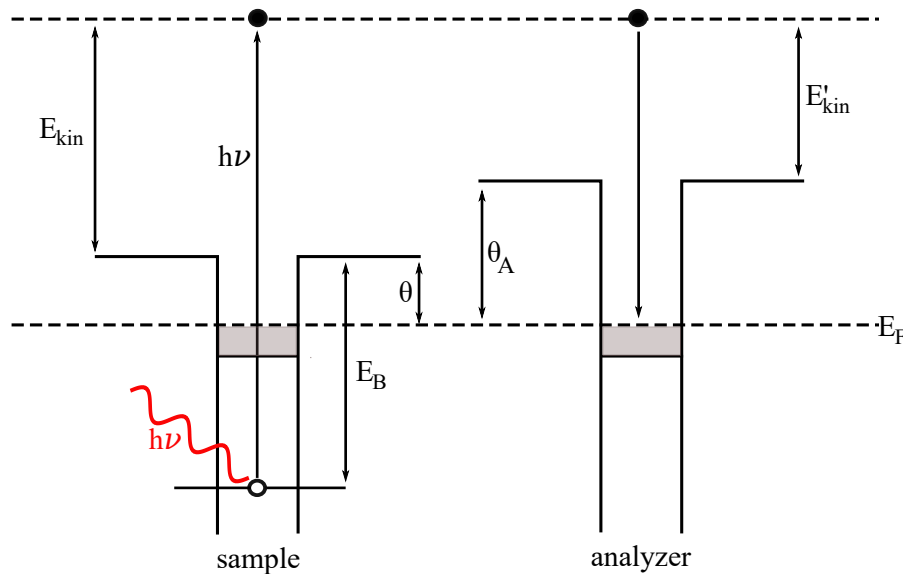


**Figure 2.7:** Schematic energy level diagram of the photoemission process. A photon with the energy  $h\nu$  is absorbed by an electron with the binding energy  $E_B$ . The electron leaves the solid by overcoming the work function  $\theta$  and can then be detected by the analyzer. The analyzer itself is characterized by the work function  $\theta_A$ .

The analyzer's work function  $\theta_A$  must also be taken into account and therefore Eq. (2.17) must be corrected to

$$E'_{kin} = E_{kin} + (\theta - \theta_A) = h\nu - E_B - \theta_A. \quad (2.18)$$

$E'_{kin}$  is the corrected value of kinetic energy. Thus, if the work function of the analyzer  $\theta_A$  as well as the photon energy  $h\nu$  are known, the binding energy  $E_B$  can be derived.  $E_B$  is unique to each element and provides information about the orbital from which the photoelectron was emitted.  $\theta_A$  can be determined by calibrating the Fermi edge of a reference sample to a well known peak [32].

### 2.3.2 Spectra and features

Both quantitative and qualitative information can be extracted from an XP spectrum. The binding energy gives information about the orbital and atom from which the photoelectron was emitted. The

intensity ratio of the XP peaks can be used to determine the amount of atomic species relative to each other. Thus, the stoichiometry of the sample can be determined, assuming a homogeneously ordered surface. In addition, conclusions about the ionization state of the different ions of the sample can be drawn from binding energies and the from satellite peaks [32].

XP peaks are labeled by quantum numbers that describe the orbital from which the photoelectrons were emitted. The nomenclature

$$Xnl_j \quad (2.19)$$

is widely used.  $X$  denotes the element and  $n$ ,  $l$  and  $j$  are the main quantum number, the azimuthal quantum number and the total angular momentum quantum number, respectively. The azimuthal quantum number  $l$  can take the values  $0, 1, 2, \dots, n-1$ . For historical reasons, these are denoted by the letters s, p, d, f. The total angular momentum quantum number  $j$  can take the values  $j = l \pm s = l \pm 1/2$ .  $s$  is the spin quantum number of the electron with  $s = 1/2$ . As an example, the XP peak Fe  $2p_{3/2}$  is caused by photoelectrons originating from the iron orbital  $n = 2$ ,  $l = 1$  and  $j = 3/2$  [14].

It is often observed that XP peaks show a doublet structure. The reason for this is the spin orbit coupling. In this coupling an interaction of the electron's magnetic orbital moment with its spin magnetic moment occurs. The electron spin can only be parallel or antiparallel to the magnetic orbital moment. For this reason two peaks can be observed, one for each spin orientation. A splitting can therefore only be observed for electrons with  $l > 0$ , since for  $l = 0$  the orbital moment is zero. However, the strength of the splitting depends inversely on the distance cubed ( $r^{-3}$ ) of the electron from the nucleus. Because of this reason, many splittings can not be resolved. The intensity ratio of the doublets can be calculated via

$$\frac{I_{l+1/2}}{I_{l-1/2}} = \frac{l+1}{l}. \quad (2.20)$$

$I_{l+1/2}$  and  $I_{l-1/2}$  are the intensities of the XP peaks with the azimuthal quantum number  $l$  in the spin-up state and the spin-down state, respectively. For example, the intensity ratio of the Fe  $2p_{3/2}$  XP peak and Fe  $2p_{1/2}$  XP peak is 2 [32].

### Shake-up and shake-off process

A large number of peaks are accompanied by secondary peaks, also called satellites, on the higher binding energy side due to e.g., intraatomic excitations. The emitted photoelectron can excite another electron in the atom to a higher energy level. In the process, the photoelectron loses part of its energy. This process creates a *shake-up* satellite on the higher binding energy side of the main peak. Since the energy levels in the atom are discrete, the energy of the *shake-up* is also discrete.

Another process is the *shake-off* transition. In this transition, another electron is excited by an emitted photoelectron. In contrast to the *shake-up* process, this electron is not excited to a higher level but is excited into the continuum. The *shake-off* satellites can have a wide range of energies, which is why the *shake-off* feature is often hidden in the background of the spectrum [14].

### Charge transfer process

In the XP spectra of transition metal oxides further satellites can be observed, which are caused by charge transfer processes. For example, the iron oxide FeO undergoes an electron transfer from the O 2p orbital to the Fe 3d orbital. The required energy is given by

$$\Delta = E(3d^{n+1}\underline{L}) - E(3d^nL). \quad (2.21)$$

Here,  $n$  denotes the number of electrons in the orbital and  $\underline{L}$  and  $L$  represent the ligand hole and the oxygen ligand from which the electron is emitted, respectively [2].

### Auger process

Another important feature in XP spectra are the Auger lines. In an Auger process, an electron close to the nucleus is released. The resulting hole is then filled by an electron from a higher shell. The atom is still in an excited state and the additional energy can be released by ejecting an electron from a higher shell. The released Auger electron is also detected in XP spectroscopy. For example, if an electron is released from the K-shell by the X-ray photon and the resulting hole is filled by an electron from the L-shell above, then an electron from the M-shell could be emitted as an Auger electron. This transition would be labeled KLM-transition [32].

### 2.3.3 Quantitative analysis and intensity equations

The analysis of the peak intensity, more precisely the analysis of the area under the peaks, provides quantitative information about the chemical composition at the surfaces. First, the background, which is caused by inelastic scattered photoelectrons, must be subtracted from the primary spectrum. The subtraction of the background can be executed conveniently with the methods of Tougaard [56] or Shirley [47].

If the spectrum is composed of clearly defined and separated peaks, it is sufficient to simply integrate the area under the peaks. Often, however, the individual peaks are very close together, meaning that they are no longer clearly separated from each other. In this case, the overall spectrum must be split into its individual components to obtain the individual contributions. The spectrum must therefore be modeled as accurately as possible in the energy range under consideration.

The integrated intensity of a film of thickness  $d$  can be calculated by

$$I_i^j = S_i^j \int_0^d \exp\left\{\frac{-z}{\lambda'}\right\} dz = S_i^j \lambda' \left(1 - \exp\left\{\frac{-d}{\lambda'}\right\}\right), \quad (2.22)$$

assuming that the photoelectrons move in a straight line out of the solid [30].  $\lambda' = \lambda \cos \phi$  is the effective inelastic mean free path (IMFP) of the electrons and  $\phi$  is the angle between the surface normal and the detector.  $z$  is the depth of the emitted photoelectron measured from the surface. Further,

$$S_i^j = \Phi(h\nu) \cdot \sigma_i^j(h\nu) \cdot A \cdot D(E) \cdot N_i \quad (2.23)$$

is the photoemission spectroscopy constant for element  $i$  and inner shell orbital  $j$ .  $\Phi$ ,  $\sigma_i^j$  and  $A$  are the X-ray flux, the photoionization cross section and the analyzed sample area, respectively.  $D$  is the spectrometer efficiency for a given kinetic energy  $E$  and  $N_i$  is the number of atoms per unit volume [30].

Some terms like the flux  $\Phi$  and the analyzed area  $A$  in Eq. (2.23) depend only on the used spectrometer, therefore these terms can be considered constant and thus, cancel out if the intensity ratio of different XP peak areas is considered. Modern XP spectrometers usually operate in the so-called fixed analyzer transmission (FAT) mode, which means that the photoelectrons entering the spectrometer are retarded by a lens system to a specific pass energy  $E_p$  before entering the analyzer. This results in an energy-independent resolution [38]. Thus, only the efficiency of the collection lenses, which is often provided by the manufacturer, has to be considered within the parameter  $D(E)$ . The IMFP  $\lambda$  can be determined using the TPP-2M equation [52]. If the analyzed orbitals  $j$  of element  $A$  and element  $B$  are at a similar binding energy, the IMFP is approximately the same and can be neglected. The orbital specific photoionization cross section  $\sigma_i^j$  is tabulated and can be looked up in the work of Scofield [42].

Taking all this into consideration, it is plausible to estimate the content of element A relative to element B by

$$\frac{I_A}{I_A + I_B} = \frac{A_A^j / \sigma_A^j}{A_A^j / \sigma_A^j + A_B^j / \sigma_B^j}. \quad (2.24)$$

$A_A^j$  and  $A_B^j$  are the background corrected peak areas of element A and element B.  $j$  denotes the orbital from which the photoelectrons are emitted. Therefore, to determine the surface composition, it is sufficient to determine the respective peak areas and to look up the respective photoionization cross sections, provided that the aforementioned assumptions apply.

## 2.4 Transport mechanisms in semiconductors

In semiconducting materials, a distinction can be made between band conduction and hopping transport. In band conduction, charge carriers are excited into a delocalized band, whereas in hopping transport the charge carriers *hop* from one localized state to the next. In ferrites, conduction is mainly due to charger carrier hopping [7]. This, to understand hopping transport in ferrites in more detail, it is necessary to discuss the nature of localized states first.

### 2.4.1 Localized states

In semiconductors, there are often a large number of localized states, whose origin are impurities like dopant ions or vacancies. Localized states are characterized by the fact that the wave functions of these states are concentrated in a confined region. Outside this region, the wave function decays exponentially, which means that individual localized wave functions do not overlap and therefore cannot be represented as Bloch waves [11].

In general, the envelop of the wave function  $\psi$  decays exponentially according to

$$\psi \rightarrow f(r) \exp\left\{\frac{-r}{L}\right\} \quad \text{as} \quad r \rightarrow \infty. \quad (2.25)$$

$f$  is a pre-factor which depends on the position  $r$  and  $L$  denotes the localization length. The localization length characterizes the size of the space region in which the wave function of an electron, moving in an impurity potential, is not exponentially small [10]. Localized states are often modelled as a three-dimensional potential well. With this assumption, the localization length  $L$  can be determined by

$$L = \frac{\hbar}{\sqrt{2m|E|}}. \quad (2.26)$$

$E$  is the electron's energy measured from the upper edge of the well. Localized states will contribute to transport processes at finite temperatures as carriers hop from occupied to free states [11].

### 2.4.2 Temperature-dependent transport mechanisms

The temperature-dependent electrical resistivity in semiconductors can be described by the universal equation

$$\rho = \rho_0 \exp\left\{\left(\frac{E_t}{k_B T}\right)^\beta\right\}. \quad (2.27)$$

$\rho_0$  and  $E_t$  are a pre-factor and the transition energy, respectively.  $k_B$  is the Boltzmann constant and  $\beta$  characterizes the type of conduction. For band conduction  $\beta = 1$  and  $E_t$  corresponds to the thermal activation energy which is necessary to lift a charge carrier from the valence or impurity band to the conduction band [3].

In comparison to band conduction, hopping conduction is characterized by the transport of charge carriers through localized states in the vicinity of the Fermi level, because e.g., the thermal energy is insufficient to excite charge carriers from the impurity band into the conduction band. Still, it might be possible that the energy is sufficient to transport a charge carrier from a defect state to an unoccupied defect state. In this case there are three basic types of conduction mechanisms, which are discussed in the following.

#### Nearest-neighbour hopping

Nearest-neighbour-hopping (NNH) (cf. Fig. 2.8) is a hopping process that describes the hopping to neighbouring localized states. The probability of nearest-neighbour-hopping can be expressed as

$$P_{hop} \propto \exp\left\{-\frac{2r}{L} - \frac{\Delta E_{NNH}}{k_B T}\right\}. \quad (2.28)$$

$L$ ,  $r$ ,  $k_B$ ,  $T$  and  $\Delta E_{NNH}$  are the localization length, the hopping distance, the Boltzmann constant, the temperature and the energy separation between the initial state and the final state, respectively [59].

From Eq. (2.28) it directly follows that the probability of NNH is highest at high temperatures. When the temperature decreases, the second term within the exponential function becomes large and finally a freeze-out of the nearest-neighbour-hopping follows.

In NNH conduction the conductivity is described by Eq. (2.27) with  $\beta = 1$ . Therefore, NNH obeys, just like band conduction, a simple Arrhenius-like law [3].

### Variable-range hopping

Variable-range hopping (VRH) (cf. Fig. 2.8) describes the process of one charge carrier hopping to another localized state which is farther away than the neighbouring states. The hopping process will take place in the vicinity of the Fermi level. Assuming a constant density of states (DOS) near the Fermi level, Mott pointed out [28], that VRH can be described in analogy to Eq. (2.27) by

$$\rho = \rho_0 \exp \left\{ \left( \frac{T_M}{T} \right)^{1/(d+1)} \right\} \quad \text{with} \quad T_M = \frac{1}{\text{DOS}(E_F) a_B^d}. \quad (2.29)$$

$d$  is the dimension of the system and  $a_B$  is the Bohr radius.  $T_M$  is the so-called Mott temperature [11].

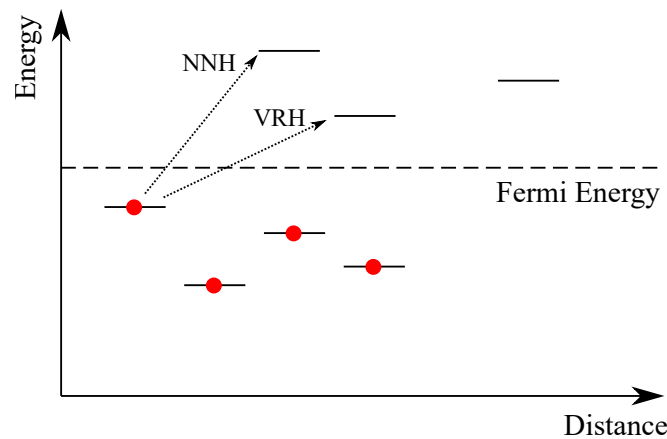


**Figure 2.8:** Schematic energy diagram showing both nearest-neighbour hopping and variable-range hopping. The red dots represent charge carriers in localized states. The dashed line indicates the Fermi energy. As an example, two hopping processes (NNH and VRH) are marked with arrows. NNH is characterized by a larger energy difference between initial and final state compared to the VRH process. The spatial distance of the states for the VRH process is larger.

Mott-VRH (cf. Eq. (2.29)) is only applicable when Coulomb interactions between localized charge carriers are negligible. However, at low enough temperatures and for highly disordered systems, the density of states (DOS) near the Fermi level is not constant but behaves according to

$$\text{DOS}(E) \propto (E - E_F)^2 \quad (2.30)$$

due to Coulomb interactions [48]. Consequently, the DOS vanishes when the energy tends to the Fermi energy (cf. Fig. 2.9). When an electron is hopping from one localized state to another the



system has to overcome the Coulomb gap energy  $E_{CG}$ . Efros-Shklovskii variable-range hopping (ES-VRH) takes into account this Coulomb gap. It can be described by Eq. (2.27) with  $\beta = 1/2$ .

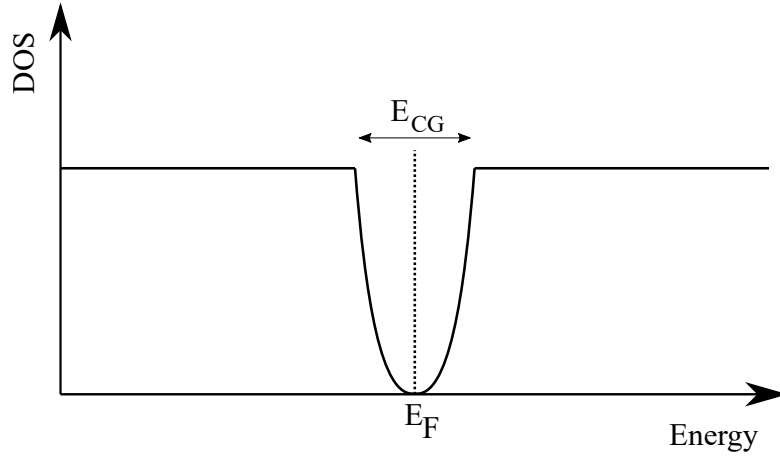


**Figure 2.9:** Schematic illustration of the Coulomb gap. In the vicinity of the Fermi level the DOS vanishes. The energy gap is characterized by  $E_{CG}$ .

## 2.5 Thin film optics

When light is irradiated onto a material, part of the light can be transmitted, which means that the light enters and leaves the material in a well-defined direction. In this regard, the transmission  $T$  can be defined as the ratio between the transmitted intensity  $I_T$  and the intensity of the incoming light  $I_0$  as

$$T = \frac{I_T}{I_0}. \quad (2.31)$$

Another part of the light can be reflected. Similarly, the reflection  $R$  is defined as the ratio between reflected intensity  $I_R$  and incoming intensity  $I_0$  as

$$R = \frac{I_R}{I_0}. \quad (2.32)$$

If the material is not absorbing and does not diffusely scatter, then

$$T + R = 1, \quad (2.33)$$

since the energy conservation holds true. However, in most materials, part of the irradiated light is also absorbed as well as scattered. In this case, the general energy conservation is given by

$$T + R + S + A = 1, \quad (2.34)$$

where

$$S = \frac{I_S}{I_0} \quad \text{and} \quad A = \frac{I_A}{I_0}. \quad (2.35)$$

$I_S$  is the intensity of the diffusely scattered light and  $S$  is the so-called optical scatter.  $A$  and  $I_A$  are the absorptance and the absorbed intensity, respectively. In this work, the absorption of a real

film-substrate system surrounded by air is investigated, which is an important factor for the optical properties of a material.

Fig. 2.10 schematically shows a film-substrate system irradiated with an initial intensity  $I_0$ . The reflected intensity  $I_R$  as well as the transmitted intensity  $I_T$  can be measured, using an integrating sphere (cf. Sec. 4.6). The energy-dependent absorption coefficient  $\alpha$ , which describes the exponential attenuation of light as it travels through a medium, can be determined for a film deposited on a transparent substrate by

$$\alpha = \frac{1}{d_{film}} \ln \left( \frac{1-R}{T} \right). \quad (2.36)$$

$d_{film}$  denotes the thickness of the thin film and  $R$  and  $T$  are the reflection and transmission of the film-substrate system, respectively [3].

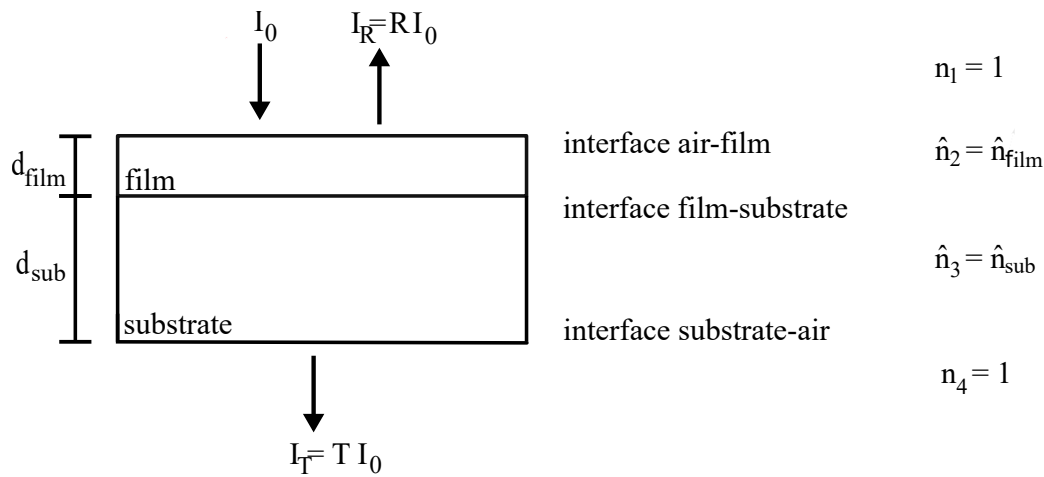


**Figure 2.10:** Schematic representation of a thin film with thickness  $d_{film}$  on a thick transparent substrate with thickness  $d_{sub}$ . The whole system is in an air environment with a non-complex refractive index of 1. The refractive indices of the film and the substrate may be complex. The reflected intensity  $I_R$  and the transmitted intensity  $I_T$  are usually measured as a function of wavelength.

### 2.5.1 Direct and indirect band gaps

The optical band gap can be determined using optical absorption and Tauc plots (cf. Sec. 2.5.2). A band gap is the energy range where no electronic states exist. The term often refers to the energy difference between the top of the valence band (TVB) and the bottom of the conduction band (BCB). Therefore, the band gap also refers to the energy which is required to excite an electron from the valence band to the conduction band. In an  $E(k)$  diagram, the TVB and the BCB are not always at the same momentum vector  $k$ . According to this, there is a distinction between a direct band gap and an indirect band gap. In a direct band gap, the TVB and the BCB are at the same  $k$  vector. In contrast, for an indirect band gap the  $k$  vector of the TVB and the BCB differ and therefore a phonon has to provide the necessary momentum change. Fig. 2.11 shows schematically the difference between a direct and indirect band gap.

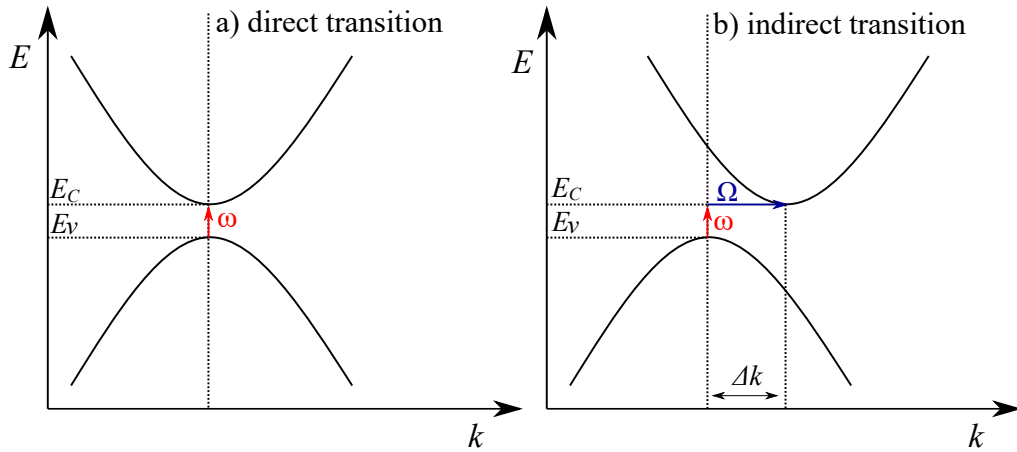


**Figure 2.11:** In a) a direct optical transition is shown. The valence band maximum and the conduction band minimum are at the same  $k$ -vector. The optical transition changes the  $k$ -vector only insignificantly, since the photon (frequency  $\omega$ ) momentum is small compared to the electrons momentum. For this reason, the transition is vertical. In b) an indirect transition is shown. Both photon and phonon (frequency  $\Omega$ ) are necessary for this transition. A photon alone cannot provide the necessary momentum change  $\Delta k$ .

When a photon with energy  $\hbar\omega$  and wave vector  $k$  is absorbed, an electron is excited from the valence band into the conduction band and a hole is created in the valence band. For such an interband transition, both the energy conservation and the momentum conservation must be given:

$$\hbar\omega \pm \hbar\Omega = E_G \quad \hbar k \pm \hbar q = \hbar\Delta k. \quad (2.37)$$

$\Omega$  is the phonon frequency and  $q$  is the phonon's wave vector.  $\Delta k$  is the momentum vector difference between the valence band state and the conduction band state. The photon wave vector  $k$  is very small and therefore for interband transitions involving only photons,  $\Delta k$  must be very small. Such transitions are vertical in the  $E(k)$  diagram. Indirect transitions with larger  $\Delta k$  are only possible with phonon participation. Usually  $\hbar\Omega \ll \hbar\omega$  and  $|q| \gg |k|$  applies. The photon provides the required energy and the phonon provides the necessary momentum for the indirect transition [12].

### 2.5.2 Tauc plots

Tauc et al. proposed a method for determining the band gap for amorphous germanium using the energy-dependent absorption coefficient  $\alpha$  [53]. Since then, this method has been widely applied, including for crystalline semiconducting thin film systems [3, 19].

Tauc's method is based on the expression

$$(\alpha h\nu)^{1/n} = A(h\nu - E_G). \quad (2.38)$$

It is assumed, that the difference between the photon energy  $h\nu$  and the band gap energy  $E_G$  is proportional to the product of the absorption coefficient  $\alpha$  and the photon energy. Here,  $A$  is a proportionality factor that describes the slope of the Tauc plot in the linear regime. The exponent  $n$  in Eq. (2.38) denotes the type of optical transition. It can be distinguished between direct and indirect transitions as well as between allowed and forbidden transitions:

- $n = 1/2$  : direct allowed transition
- $n = 3/2$  : direct forbidden transition
- $n = 2$  : indirect allowed transition
- $n = 3$  : indirect forbidden transition

The allowed transitions typically dominate the absorption processes [6], which is why this work will solely have its focus on the allowed direct and indirect transitions. To determine the band gap, it is first necessary to calculate the energy-dependent absorption coefficient  $\alpha(h\nu)$  by using Eq. (2.36). Here, it is essential to measure the energy range below the band gap energy and above the band gap energy. Subsequently, for the direct allowed transition,  $(\alpha h\nu)^2$  is plotted against  $h\nu$  and for the indirect allowed transition,  $(\alpha h\nu)^{1/2}$  is plotted against  $h\nu$ . Afterwards, the linear regime of the Tauc plot is fitted. The band gap is given by the intersection of the energy axis and the linear extrapolation. If it is unknown what type of optical transition the material under consideration might have, the Tauc plots should be evaluated for both  $n = 1/2$  and  $n = 2$ . Fig. 2.12 shows a typical Tauc plot.

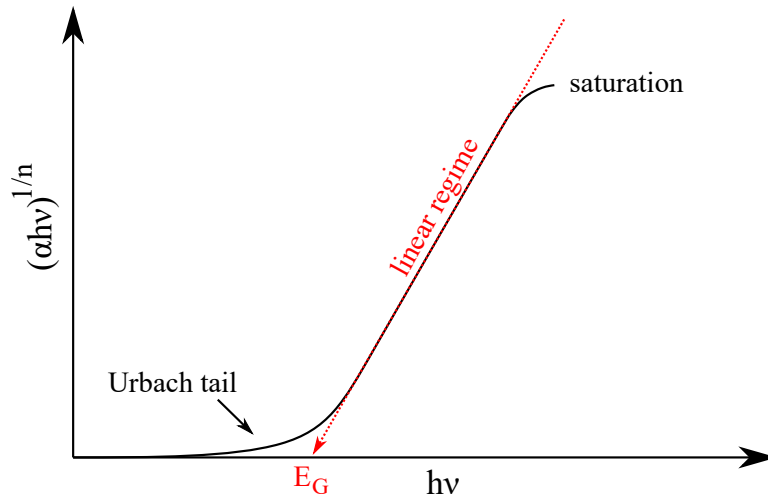


**Figure 2.12:** Typical shape of a Tauc plot.  $(\alpha h\nu)^{1/n}$  initially increases exponentially (Urbach tail) with increasing photon energy  $h\nu$  and then increases linearly. At a certain photon energy, saturation sets in.  $E_G$  is given by the intersection of the energy axis and the linear extrapolation.

For an ideal material,  $(\alpha h\nu)^{1/n}$  would be zero for  $h\nu < E_G$  and would then increase linearly for  $h\nu > E_G$ . In real measurements, there are deviations from the linear behaviour in the lower as well as in the upper energy range. In the lower energy range ( $h\nu < E_G$ ), the deviation from the linear behaviour can be explained by defect states or other sub-bands. This phenomenon was first investigated by Urbach [57] and is known today as the so-called Urbach tail. In the Tauc plot this range can be

described as an exponential function. In the higher energetic range ( $h\nu \gg E_G$ ), saturation usually takes place and therefore this region is often not further analyzed.

### 2.5.3 X-ray reflectivity - XRR

The determination of the thickness of ultra-thin films is of great importance in research as well as in technical applications. To determine the thickness of a film deposited on a solid substrate, X-ray reflectometry (XRR) has proven to be a suitable method [50]. Using XRR, the sample is illuminated with X-rays at very low angles of incidence ( $< 5^\circ$ ).

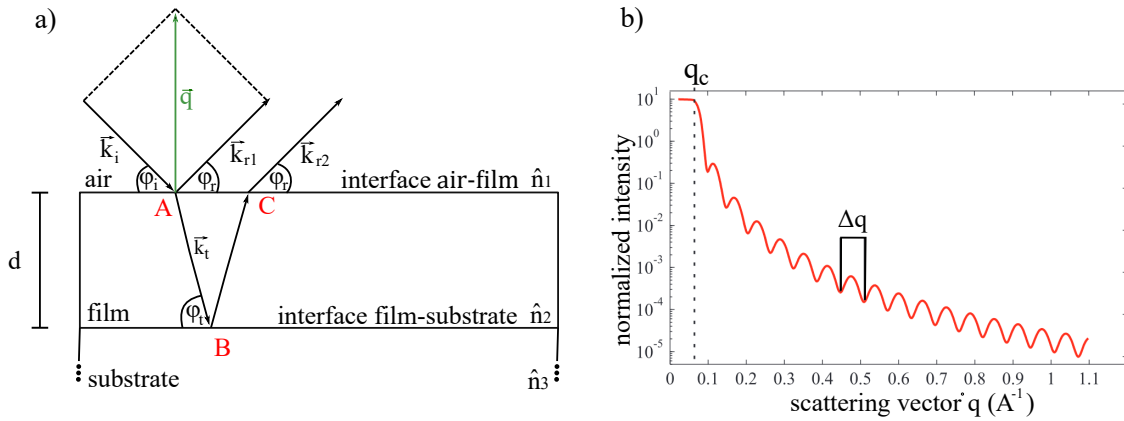


**Figure 2.13:** a) Schematic representation of the beam path in an XRR measurement. The X-ray beam  $\vec{k}_i$  is incident on the film surface (point A) where it is partly reflected ( $\vec{k}_{r1}$ ) and partly transmitted ( $\vec{k}_t$ ). The transmitted beam is again partly reflected and partly transmitted at the film-substrate interface.  $\vec{k}_{r1}$  and  $\vec{k}_{r2}$  may interfere which eventually leads to an oscillating intensity curve due to constructive and destructive interference. b) Intensity curve as a function of the scattering vector  $q$ . Up to a scattering vector of  $q_c$  total reflection occurs, thus all light is reflected. After that a periodic oscillation can be observed caused by interference effects between the beams  $\vec{k}_{r1}$  and  $\vec{k}_{r2}$ . The film thickness can be calculated from the distance  $\Delta q$  between two adjacent oscillations.

Fig. 2.13 a) shows the beam path of an XRR measurement for a monolayer system. An X-ray with the wave vector  $\vec{k}_i$  hits the surface with an angle of incidence of  $\varphi_i$  (point A). Note, that  $\varphi_i$  is defined as the angle between  $\vec{k}_i$  and the surface (contrary to the usual convention in optics). The electromagnetic wave  $\vec{k}_i$  is partly reflected and partly transmitted, if no total reflection occurs. This results in a transmitted wave vector  $\vec{k}_t$  and a reflected wave vector  $\vec{k}_{r1}$ . The transmitted component  $\vec{k}_t$  can be reflected at the film-substrate interface (point B) and then propagate towards the surface of the film and into the vacuum (point C), resulting in  $\vec{k}_{r2}$ . The beams  $\vec{k}_{r1}$  and  $\vec{k}_{r2}$  will subsequently superimpose leading to constructive and destructive interferences and thus, to an oscillating behavior of the intensity as a function of  $\varphi_i$ . Here, the periodicity of these oscillations is directly related to the thickness of the film.

From the law of reflection it follows that the angle of incidence  $\varphi_i$  is always equal to the angle of reflection  $\varphi_r$ , therefore  $\varphi_i = \varphi_r$ . The scattering vector is defined by  $\vec{q} = \vec{k}_{r1} - \vec{k}_i$  and is always perpendicular to the sample's surface. Assuming that the scattering is elastic, the conservation of

energy applies and therefore  $|\vec{k}_i| = |\vec{k}_r| = \frac{2\pi}{\lambda}$ .  $\lambda$  denotes the wavelength of the X-ray. Consequently, the magnitude of  $\vec{q}$  amounts to

$$|\vec{q}| = \frac{4\pi}{\lambda} \sin \varphi_i. \quad (2.39)$$

Fig. 2.13 b) shows the intensity as a function of the scattering vector  $q$  for a film grown on a substrate. When X-rays are incident on the surface at an angle less than the critical angle  $\varphi_c$  (which corresponds to the critical scattering vector  $q_c$ ), total reflection occurs and all X-rays are reflected. For incidence angles greater than  $\varphi_c$ , part of the radiation is transmitted, resulting in a decrease of the total intensity. Different interfaces exist in a film-substrate system and at each interface there is transmission and reflection. The X-rays reflected at the different interfaces can interfere constructively and destructively, which is why periodic oscillations, called Kiessig fringes, occur.

For a monolayer system, the film thickness  $d$  can be determined from the periodicity of the oscillations of the Kiessig fringes:

$$d = \frac{2\pi}{\Delta q}. \quad (2.40)$$

$\Delta q$  is the scattering vector difference of two adjacent Kiessig fringes [50].

### 3. Material system

The materials used in this work are described in this chapter. Magnesium oxide serves as a substrate for cobalt ferrite ultrathin films.

#### 3.1 Magnesium oxide - MgO

In this thesis, MgO serves as a substrate for the epitaxial deposition of thin cobalt ferrite films. MgO crystallizes in the rock salt structure. It consists of  $\text{Mg}^{2+}$  and  $\text{O}^{2-}$  ions in a ratio of 1:1. The unit cell has a length of  $a_{\text{MgO}} = 4.2117 \text{ \AA}$  [13] with a distance between the  $\text{Mg}^{2+}$  and  $\text{O}^{2-}$  ions of  $2.105 \text{ \AA}$ . Both types of ions form a fcc sublattice, which are shifted from each other by half the length of the unit cell. The surface unit cell is rotated by  $45^\circ$  in relation to the bulk unit cell and has a length of  $a_s = a_{\text{MgO}}/\sqrt{2}$ . MgO has band gap energy of  $7.8 \text{ eV}$  [17], making MgO an insulator and transparent to visible light.

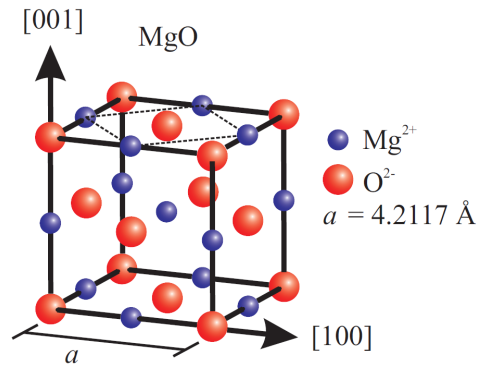


**Figure 3.1:** Schematic representation of the MgO unit cell. The surface unit cell is shown as a dashed line. Taken from [54].

#### 3.2 Cobalt ferrite - $\text{CoFe}_2\text{O}_4$

Stoichiometric cobalt ferrite is described by the chemical formula  $\text{CoFe}_2\text{O}_4$  and crystallizes in the inverse spinel structure [46].

The spinel is a common crystal structure consisting of a cubic close-packed arrangement of anions, in which one eighth of the tetrahedral sites and half of the octahedral sites are occupied by cations [18]. The spinel consists of two types of cations A and B and one type of anion X. One can distinguish between two extremes: In the normal spinel  $(\text{A})[\text{B}_2]\text{X}_4$  all cations of type B occupy octahedral sites (square brackets), while all cations of type A occupy tetrahedral sites (round brackets). Analogous

to this, the inverse spinel  $(B)[AB]X_4$  can be defined, where cations of type B occupy tetrahedral and octahedral sites and cations of type A are only located at octahedral sites. However, other cation distributions, which do not correspond to the extremes mentioned above, are also possible. Consequently, the general formula for spinels is

$$(A_{1-j}B_j)[A_jB_{2-j}]X_4, \quad (3.1)$$

where  $j$  is the degree of inversion. For  $j = 0$  the resulting cation distribution corresponds to that of a normal spinel and for  $j = 1$  to that of an inverse spinel.  $0 < j < 1$  defines the intermediate state with mixed spinel structure [49].

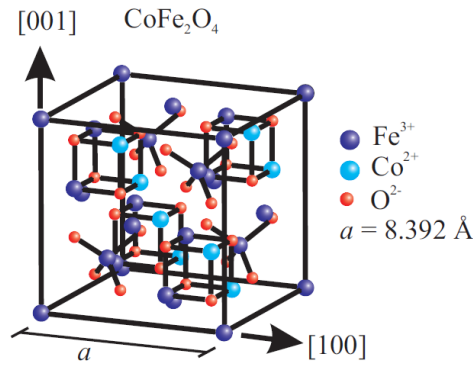


**Figure 3.2:** Schematic representation of the cobalt ferrite unit cell. Taken from [54].

The inverse spinel  $\text{CoFe}_2\text{O}_4$  (cf. Fig. 3.2) consists of a cubic close-packed array of  $\text{O}^{2-}$  anions, in which one eighth of the tetrahedral sites are occupied by  $\text{Fe}^{3+}$  cations and half of the octahedral sites are occupied evenly by  $\text{Co}^{2+}$  and  $\text{Fe}^{3+}$  cations. Hence, stoichiometric cobalt ferrite can be expressed by



according to Eq. (3.1). The lattice constant is  $8.392 \text{ \AA}$  [22], which is about twice as large as the lattice constant of  $\text{MgO}$ . Therefore, the lattice mismatch between  $\text{MgO}$  and  $\text{CoFe}_2\text{O}_4$  is small (about  $-0.37\%$ ), which makes  $\text{MgO}$  an excellent substrate for cobalt ferrite films. The (001) surface unit cell is rotated by  $45^\circ$  relative to the bulk unit cell.

Apart from stoichiometric cobalt ferrite, there is also a Co-deficient phase and the Co-rich phase of cobalt ferrite, depending on the amount of Co relative to the amount of Fe. Here, the stoichiometry parameter  $x$  defines the Co content relative to the Fe content, so that the chemical formula of cobalt ferrite can be generalized to

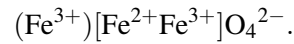


The increase of the Co-concentration influences the structural, magnetic and electronic properties of the material [31, 43]. For instance, Nlebedim et al. were able to show, that an increase in  $x$  led to the formation of an additional rock salt phase  $(\text{Co}_{1-y}\text{Fe}_y\text{O})$ , whereas a decrease led to the formation of an additional  $\alpha\text{-Fe}_2\text{O}_3$  phase [31]. In addition, studies on  $\text{Co}_x\text{Fe}_{3-x}\text{O}_4$  powder samples suggest, that



an increase in  $x$  beyond  $x = 1$  leads to a coexistence of  $\text{Co}^{3+}$  cations with  $\text{Co}^{2+}$  and  $\text{Fe}^{3+}$  in the crystal lattice, which affects the physical properties [31].

$\text{Co}_x\text{Fe}_{3-x}\text{O}_4$  is often considered a Co-substituted variant of magnetite ( $x = 0$ ). By analogy with Eq. (3.1), magnetite has the chemical composition



When the Co content is increased ( $0 < x < 1$ ),  $\text{Fe}^{2+}$  cations are gradually replaced by  $\text{Co}^{2+}$  cations on octahedral B-sites. For stoichiometric cobalt ferrite ( $x = 1$ ), all  $\text{Fe}^{2+}$  cations is replaced by  $\text{Co}^{2+}$  and therefore Eq. (3.2) applies. Increasing the Co content even beyond  $x = 1$  results in a further substitution of Fe for Co. For reasons of charge balance,  $\text{Fe}^{3+}$  cations are now substituted for  $\text{Co}^{3+}$  cations.

However, the cation distribution described is only correct for an ideal inverse spinel structure. It has been reported that cobalt ferrite often adopts a partial inverse structure ( $0 < j < 1$ ) [29, 31], which means that  $\text{Co}^{2+}$  cations are localized at both A and B sites. In addition, a recent study has shown that  $\text{Co}^{3+}$  can also be found at tetrahedral A-sites of Co-rich phases [24].

In summary, the cation distribution of cobalt ferrite is generally highly complicated and requires structural analysis by Mössbauer spectroscopy or other methods.



## 4. Experimental setup

In this chapter, the different experimental setups used in this thesis are briefly presented and explained.

### 4.1 Ultra high vacuum system

The preparation and characterization of thin films is usually performed under ultra-high vacuum (UHV) conditions. For surface sensitive characterization methods such as XPS or LEED, a clean surface is essential, since adsorbates can negatively influence the measurements.

The time required for a monolayer of adsorbates to deposit on the surface is called monolayer time  $\tau$ . It depends, among other parameters, on the pressure  $p$  inside the UHV chamber. According to the kinetic theory of gases,  $\tau$  can be estimated by

$$\tau = \frac{n_0 \sqrt{2\pi m k_B T}}{p}. \quad (4.1)$$

$n_0$ ,  $m$ ,  $T$  and  $p$  are the number of atoms in a monolayer, the molecule mass, the temperature and the pressure, respectively. Based on Eq. (4.1), it directly follows that the monolayer time  $\tau$  increases the smaller the pressure  $p$  becomes. For example, at a pressure of 1013 mbar the monolayer arrival time is about 3 ns. Under UHV conditions (about  $10^{-8}$  mbar)  $\tau$  is about 1 h [32].

In the context of this work, the UHV chambers shown schematically in Fig. 4.1 are used. All chambers are connected by air locks and can be evacuated separately. The substrates are attached to a sample holder and enter the vacuum system via the load lock. Using transfer rods, the sample holder can be moved within the system. The preparation chamber I serves exclusively as a cleaning chamber. The infiltrated substrate can be thermally cleaned using a filament to remove adsorbates. The preparation chamber II is used for the deposition of the films. Iron and cobalt effusion cells generate particle beams for RMBE. Oxygen can be added both in the cleaning chamber and in the preparation chamber. An *in-situ* characterization of the sample is performed in the analysis chamber. Here, the sample can be analyzed by means of LEED and XPS. All chambers are equipped with pressure gauges. In the cleaning chamber as well as the preparation chamber there is a pressure of about  $1 \times 10^{-8}$  mbar to  $5 \times 10^{-9}$  mbar, whereas in the analysis chamber there is a pressure of at least  $1 \times 10^{-10}$  mbar.

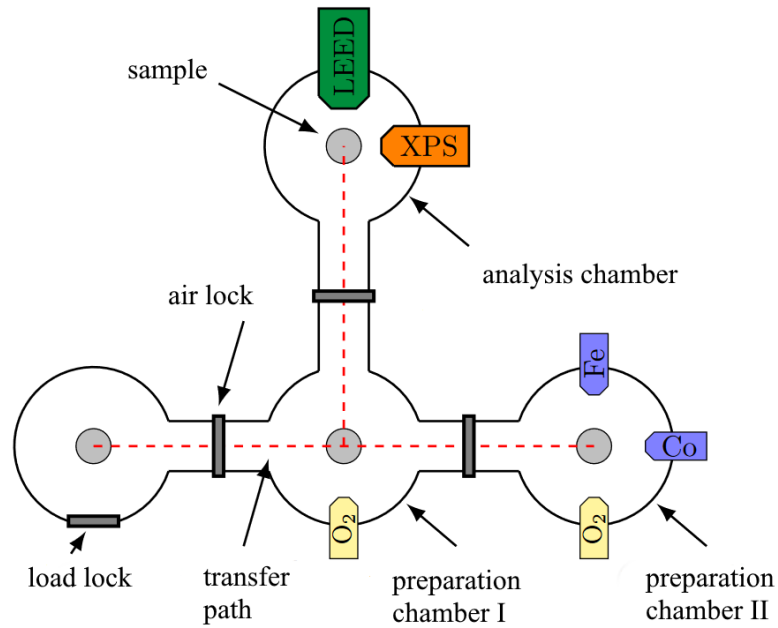


**Figure 4.1:** Schematic overview of the UHV system. The substrates enter the system via the load lock. All chambers are connected via air locks and can be evacuated independently. In the preparation chamber I, the substrates are thermally cleaned and in the preparation chamber II, the deposition of the films takes place. The preparation chamber II is equipped with a cobalt and an iron evaporator. Both preparation chambers can be filled with oxygen. The characterization of the samples with XPS and LEED is performed in the analysis chamber. Adapted from [41].

## 4.2 Sample preparation

All  $\text{Co}_x\text{Fe}_{3-x}\text{O}_4$  films are prepared in the UHV system (cf. Fig. 4.1). Commercially available  $\text{MgO}(001)$  substrates made by CrysTec are used. The substrates are polished on one side and have a size of  $10 \times 10 \times 0.5$  mm. Before the films are grown by RMBE, the substrates are thermally cleaned in the preparation chamber I at a temperature of  $400^\circ\text{C}$  for 1 h in a diluted oxygen atmosphere of  $1 \times 10^{-4}$  mbar. This allows carbon compounds and other impurities on the substrate's surface to be easily desorbed and also prevents oxygen vacancies from forming [32]. After cleaning, XPS and LEED measurements are performed to check whether adsorbates are still present on the surface. If the substrates are clean, the film can be grown in preparation chamber II, else the cleaning procedure is repeated.

The evaporators in the preparation chamber II generate a beam of atoms or molecules that is directed towards the substrate. They contain a metal rod made of iron or cobalt and a filament to heat the rod. High voltage is applied between the filament and the metal rod to accelerate the electrons emitted from the filament towards the rod. This causes the metal to heat up strongly and as soon as the sublimation temperature is reached, evaporation begins. The onset of film growth can be controlled by a shutter which is located in front of the evaporator. The material flux is controlled via the distance of the metal rod and the filament. The deposition rate is measured with a flux monitor.

In the first series of experiments, the stoichiometry  $x$  of thin  $\text{Co}_x\text{Fe}_{3-x}\text{O}_4$  films on  $\text{MgO}(001)$  is varied.

After thermal cleaning, the MgO(001) substrate is simultaneously evaporated with Co and Fe in the preparation chamber II. To obtain the different stoichiometries, the flux of the Co evaporator is always kept constant whereas the flux of the Fe evaporator is varied. For all sample preparations, the substrate temperature during evaporation is controlled to 250 °C and the diluted oxygen atmosphere is set to pressure of about  $5 \times 10^{-6}$  mbar.

In the second series of experiments, the stoichiometry  $x$  of  $\text{Co}_x\text{Fe}_{3-x}\text{O}_4$  thin films on MgO(001) is kept constant. The samples are prepared at varying diluted oxygen atmospheres of  $1 \times 10^{-6}$  mbar,  $5 \times 10^{-6}$  mbar and  $1 \times 10^{-5}$  mbar. The substrate temperature is kept at 250 °C.

### 4.3 XPS setup

The XPS measurements of the Fe (2p, 3p) and Co (2p, 3p) core-levels are performed with a commercial system from SPECS, consisting of a non-monochromatic X-ray source (SPECS XR 50), a lens system, a concentric hemispherical analyzer (Phoibos HSA 150) and a detector. Fig. 4.2 shows a schematic sketch of the XPS setup.

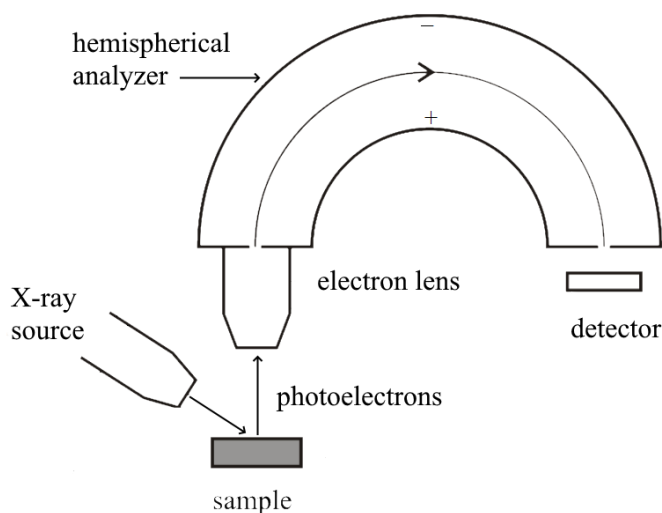


**Figure 4.2:** Schematic overview of the XPS instruments. The X-ray source irradiates the sample with high-energy photons, which subsequently emit photoelectrons. The photoelectrons pass through a lens system before entering the hemispherical analyzer. Only electrons with a certain pass energy enter the detector. Taken and adapted from [4].

The XPS system, like the LEED system, is located in the analysis chamber of the UHV system. The X-ray photons are generated by bombarding a target with high-energy electrons in the X-ray source. One can choose between aluminum and magnesium targets. The characteristic main line  $K_{\alpha 1,2}$  of Mg and Al have an energy of about 1253.6 eV and 1486.6 eV, respectively. Other important X-ray characteristic lines are  $K_{\alpha 3}$  and  $K_{\alpha 4}$  line. In this work, solely a Mg anode is used because the spectrum recorded with a Mg anode is less superimposed with Auger lines in the Fe 2p range. The  $K_{\alpha 3}$  line is shifted about 9.8 eV to higher photon energies and has an intensity of about 6.4 % relative to the main line. The  $K_{\alpha 4}$  line is shifted about 11.8 eV and its intensity is about 3.2 % relative to the

main line. There are other lines (e.g.  $K_{\alpha 5}$ ,  $K_{\alpha 6}$ ,  $K_{\beta}$ ), but due to their weak intensity their impact can be neglected [32].

The photoelectrons generated by the photoelectric effect, subsequently pass through the lens system and the hemisphere analyzer, before they are detected by the detector. The hemisphere analyzer consists of two concentric hemispheres between which a voltage is applied. The applied voltage ensures that only photoelectrons with a certain pass energy reach the detector.

For the measurement of the valence band, an ESCA PHI 5000 VersaProbe III has been used since it is equipped with a monochromatic X-ray source using an Al anode. The general setup does not differ from Fig. 4.3. The ESCA is used because it can reach a higher resolution and there are no parasitic effects due to the use of a monochromatic X-ray source.

#### 4.4 LEED setup

For the LEED measurements the ErLEED 150 instrument from Specs is used. This system consists of an electron gun and a hemispherical fluorescent screen to observe the diffraction pattern. The sample is located at the center of the curvature of the screen. A CCD camera is used to record the resulting diffraction patterns. Fig. 4.3 schematically shows the experimental setup.

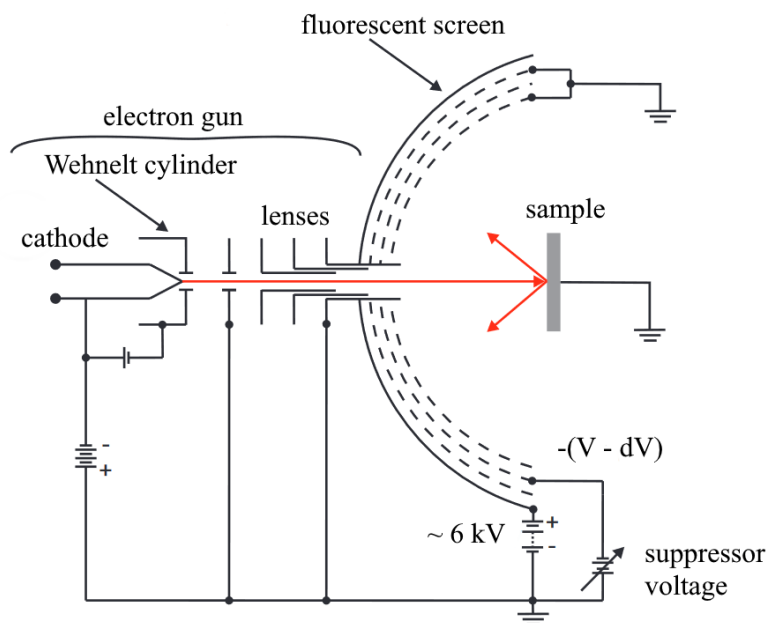


**Figure 4.3:** Schematic representation of the LEED experimental setup. The electron gun, consisting of a cathode, a Wehnelt cylinder and an electrostatic lens system, generates a focused and collimated electron beam. The electrons are subsequently diffracted at the surface of the sample and the diffracted electrons reach the fluorescent screen after passing a grid system which ensures that no inelastically scattered electrons reach the screen. Adapted from [32].

The cathode ( $I_{cat} \approx 2.25$  A) emits electrons, which are subsequently focused and collimated by a Wehnelt cylinder and an electrostatic lens system. The electrons propagate perpendicular to the sample's surface and are diffracted at the surface. The diffracted electrons hit the fluorescent screen

allowing the pattern to be observed.

In front of the fluorescence screen there is a grid system, which minimizes the influence of inelastically scattered electrons on the diffraction pattern. The first grid is at earth potential, which means that the space between sample and grid is field-free. The diffracted electrons therefore move in a linear path to the fluorescence screen. The second grid is at the so-called suppressor potential  $V_{sup}$ . This filters out the inelastically scattered electrons, which leads to an improvement of the spot-to-background contrast. The third grid, like the first one, is at earth potential. After the electrons have passed the third grid, they are accelerated to the fluorescent screen ( $V_{screen} \approx 6\text{ kV}$ ).

## 4.5 XRR setup

The XRR measurements are performed *ex-situ* using a Philips X'Pert PRO MPD X-ray diffractometer. Fig. 4.4 schematically shows the measuring principle.

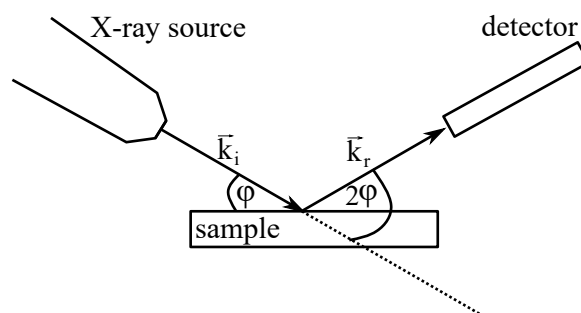


**Figure 4.4:** A light source irradiates the sample with X-rays. The incident light is described by the wave vector  $\vec{k}_i$  and the reflected part is denoted with  $\vec{k}_r$ . The angle  $\varphi$  is variable and the detector moves in turn according to  $2\varphi$ .

The X-ray source is equipped with a copper anode that generates X-ray photons with an energy of 8.048 keV (Cu  $K_{\alpha 1}$  line). This corresponds to a wavelength of about 1.54 Å. The measurement is performed in a  $\varphi$ - $2\varphi$ -geometry. The angle of incidence between the sample and the X-ray beam is  $\varphi$  and the angle between the X-ray beam and the detector is  $2\varphi$ . The intensity of the reflected beam is measured as a function of the angle of incidence.

## 4.6 UV-Vis setup

The transmission and reflection measurements are performed with a Perkin Elmer Lambda 650 UV-Vis spectrometer. Simplified, the UV-Vis spectrometer consists of a halogen lamp made of deuterium and tungsten that generates light in the wavelength range from about 200 nm to about 1200 nm. The light is aligned and focused by an optical system, and subsequently a monochromator is used to sweep the wavelength. Afterwards, the light is incident on an integrating sphere. Dependent on the location of the sample, a distinction can be made between two measurement modes, which are shown in Fig. 4.5 a) and b).

In a) the reflection mode is displayed. The light enters the integrating sphere via the entrance and is incident on the sample, which is located at the end of the sphere. The light is specularly reflected at

the sample surface. In addition, diffuse light reflection in all directions is possible. The geometry of the integrating sphere is such that all light (specularly reflected and diffuse reflected) is directed to the detector after various reflections on the inner sphere surface. Therefore, the total reflection can be determined with this simple setup. Fig. 4.5 b) shows the transmission mode. The sample is located in front of the integrating sphere entrance and any transmitted light is focused on the detector after various reflections on the inner sphere surface. The baffle is used in both modes, as it blocks light which is directly coming from the sample.

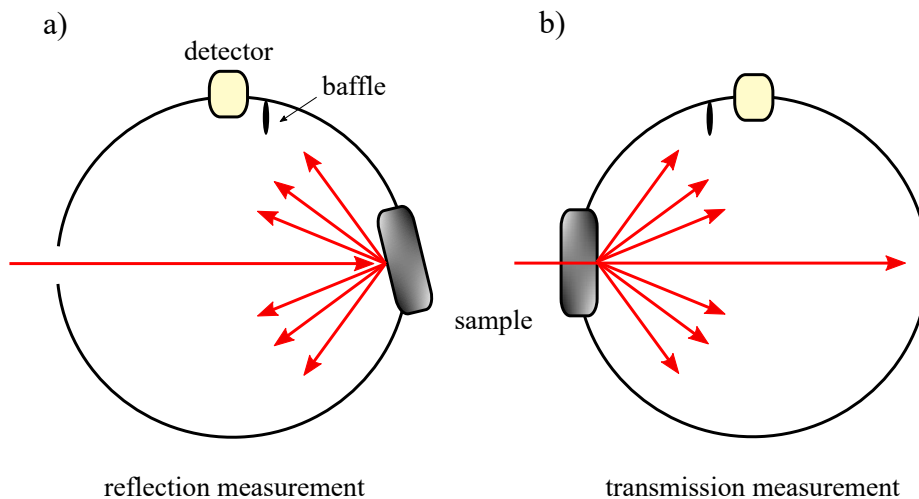


**Figure 4.5:** Integrating sphere setup for a) reflection measurements and b) transmission measurements. The baffle is used to block direct light coming from the sample.

## 4.7 Van der Pauw setup

The resistivities of the samples are measured with the setup shown in Fig. 4.6.

The sample is located at the end of a sample rod and is fixated by four contacts. The contacts are spring-mounted which prevents damage to the sample surface. A power supply unit is used to apply a current between two contacts and a voltmeter simultaneously measures the potential difference between the other two contacts. The wiring is regulated by a switching matrix. There are 16 different wiring possibilities, however, only 8 wirings (cf. Fig. 4.7) are used for resistivity measurements.

A heating filament is mounted above the sample, with which the temperature of the sample can be varied. A thermoelement provides the measurement of the temperature. The sample rod is located in a cryostat, which can be filled with liquid nitrogen ( $\text{LN}_2$ ). The rod does not come into contact with  $\text{LN}_2$  as it is contained in a stainless steel case which can be evacuated by a rotary vane pump. For optimal thermal coupling, the case can be filled with nitrogen gas  $\text{N}_2$ . By simultaneously cooling the sample with  $\text{LN}_2$  and heating it with the heating element a temperature dependent measurement can be achieved. The magnet is not used in this work.



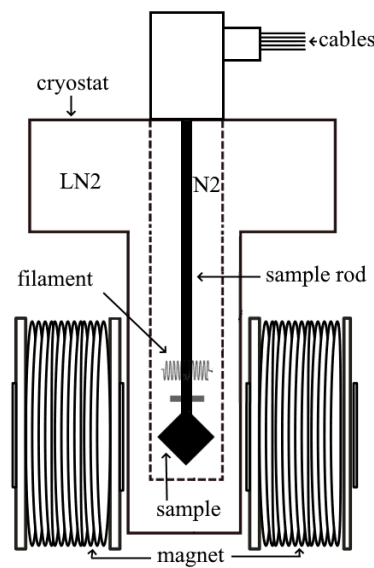


**Figure 4.6:** Schematic representation of the van der Pauw measuring system. The sample is located between two magnetic coils inside a sample rod, which in turn is surrounded by a cryostat. The cryostat can be filled with liquid nitrogen. A heating coil can be used to control the sample temperature. For a better thermal coupling, the sample rod can be evacuated and filled with nitrogen gas.

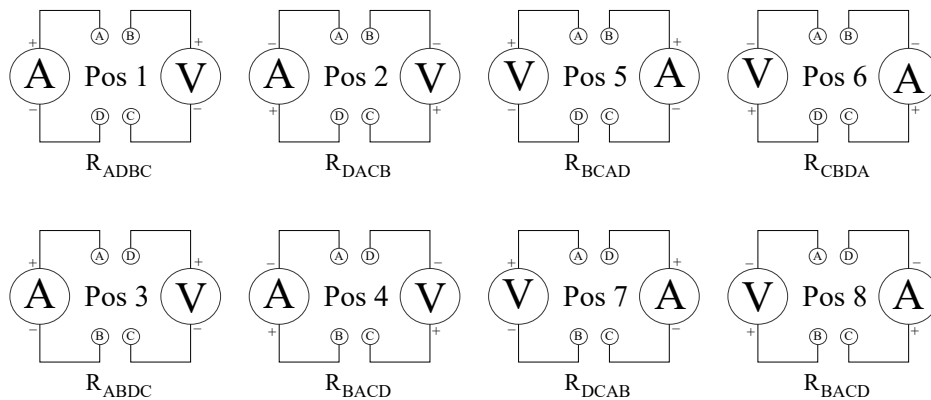


**Figure 4.7:** Eight different wirings for the Van der Pauw measurement. The wiring of the upper row and the wiring of the lower row are equivalent.

### Van der Pauw method

The van der Pauw method is widely used to determine the sheet resistances of thin films. The great advantage of this method is the independence of the sample geometry. In order for the van der Pauw method to work, a few conditions must be met. First, the film thickness must be small compared to the bulk and should be uniform. The film should be homogeneous and should not have any holes or islands. Furthermore, the contact pins should be small and dot-shaped and positioned at the edge of the sample [34].

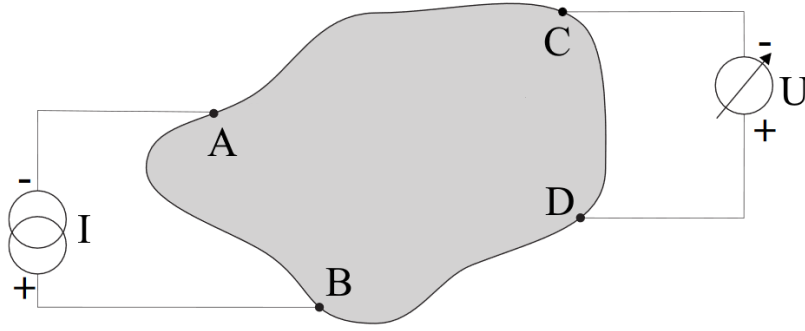


**Figure 4.8:** Schematic representation of the Van der Pauw 4-point measuring method. An electric current is conducted from A to B and the voltage is measured between C and D. This specific arrangement measures the resistance  $R_{ABCD}$ .

### Measurement of sheet resistances

The sheet resistance is defined by

$$R_s = \frac{\rho}{d}. \quad (4.2)$$

$\rho$  is the resistivity and  $d$  is the film thickness.  $R_s$  can be measured with van der Pauw's 4-point method. Consider the van der Pauw geometry shown in Fig. 4.8. If an electric current  $I_{AB}$  is applied from pin A to pin B, a voltage  $U_{CD}$  can be measured between pin C and pin D. The resistance  $R_{ABCD}$  can be calculated using Ohm's law:

$$R_{ABCD} = \frac{U_{CD}}{I_{AB}}. \quad (4.3)$$

The resistance  $R_{ACBD}$  can be calculated analogously. Assuming a two-dimensional radial current propagation and using the conformal transformation in combination with the superposition principle, the relation

$$1 = \exp\left\{-\frac{\pi}{R_s}R_{ABCD}\right\} + \exp\left\{-\frac{\pi}{R_s}R_{ACBD}\right\} \quad (4.4)$$

is obtained. Eq. (4.4) cannot be solved analytically. However,

$$R_s = \frac{\pi}{\ln 2} \cdot \frac{R_{ABCD} + R_{ACBD}}{2} \cdot f \quad (4.5)$$

is a valid approximate solution. The sample's shape is taken into account by the form factor  $f$ , which depends on the ratio  $R_{ABCD}/R_{ACBD}$ . In this work symmetrical samples are used, therefore  $R_{ABCD} \approx R_{ACBD}$  and  $f \approx 1$ .

From Eq. (4.5), it can be seen that only two wiring positions are needed to measure and calculate the sheet resistance  $R_s$ . The resistances  $R_{ADBC}$ ,  $R_{DACB}$ ,  $R_{BCAD}$  and  $R_{CBDA}$  as well as  $R_{ABDC}$ ,  $R_{BACD}$ ,  $R_{DCAB}$  and  $R_{CDBA}$  are equivalent. To increase the accuracy of the measurement, they can be averaged [34].

## 5. Properties of ultrathin $\text{Co}_x\text{Fe}_{3-x}\text{O}_4$ films on $\text{MgO}(001)$ depending on the Co content $x$

In the first part of this thesis,  $\text{Co}_x\text{Fe}_{3-x}\text{O}_4$  ultrathin films with varying stoichiometry  $x$  are grown on  $\text{MgO}(001)$ . Electronic, optical and transport properties of the films are studied as a function of  $x$ .

### 5.1 XPS results

The XP spectra are recorded to investigate the chemical composition as well as the electronic properties of the  $\text{Co}_x\text{Fe}_{3-x}\text{O}_4$  thin films. The film stoichiometry, i.e. the Co content relative to the Fe content, is determined using the Co 3p and Fe 3p spectra. The Fe 2p and Co 2p spectra are used to determine the predominant oxidation states of the Fe and Co cations, respectively. The last part of this section investigates the influence of the stoichiometry on the valence band structure.

#### 5.1.1 Analysis of the Fe 3p and Co 3p core-level spectra

The stoichiometry of the prepared  $\text{Co}_x\text{Fe}_{3-x}\text{O}_4$  films is determined from the Fe 3p and Co 3p spectra. The calculation is performed by means of the formalism described in Sec. 2.3.3. The basis of this method is the intensity ratio

$$Y_{\text{Co}} = \frac{I_{\text{Co}}^{3p}/\sigma_{\text{Co}}^{3p}}{I_{\text{Co}}^{3p}/\sigma_{\text{Co}}^{3p} + I_{\text{Fe}}^{3p}/\sigma_{\text{Fe}}^{3p}}, \quad (5.1)$$

as given by Eq. (2.24). The photoionization cross sections  $\sigma_A^j$  ( $A$  and  $j$  denote the element and the orbital, respectively) are taken from the work of Scofield [42]. The Fe 3p and Co 3p peaks have been chosen for stoichiometry determination because the peaks are positioned closely together. Hence, the kinetic energy dependent IMFP is similar for both peaks and thus, negligible.

In principle, both the Fe 3p peak and the Co 3p peak should be split into two separate peaks due to spin orbit coupling. However, only one peak is observable for each element. The reason for this is that the energy difference between the  $j = 1/2$  and  $j = 3/2$  states is too small to be resolved with the used analyzer. Still, both peaks are accompanied by a satellite structure that must be taken into account. In order to determine  $I_{\text{Co}}^{3p}$  and  $I_{\text{Fe}}^{3p}$  as accurately as possible, it is crucial to take into account every contribution (main peak and satellites) of the respective element. The modeling of the peaks (cf. Fig. 5.1) is guided by the results of McIntyre et al. [27] and Kim et al. [21].

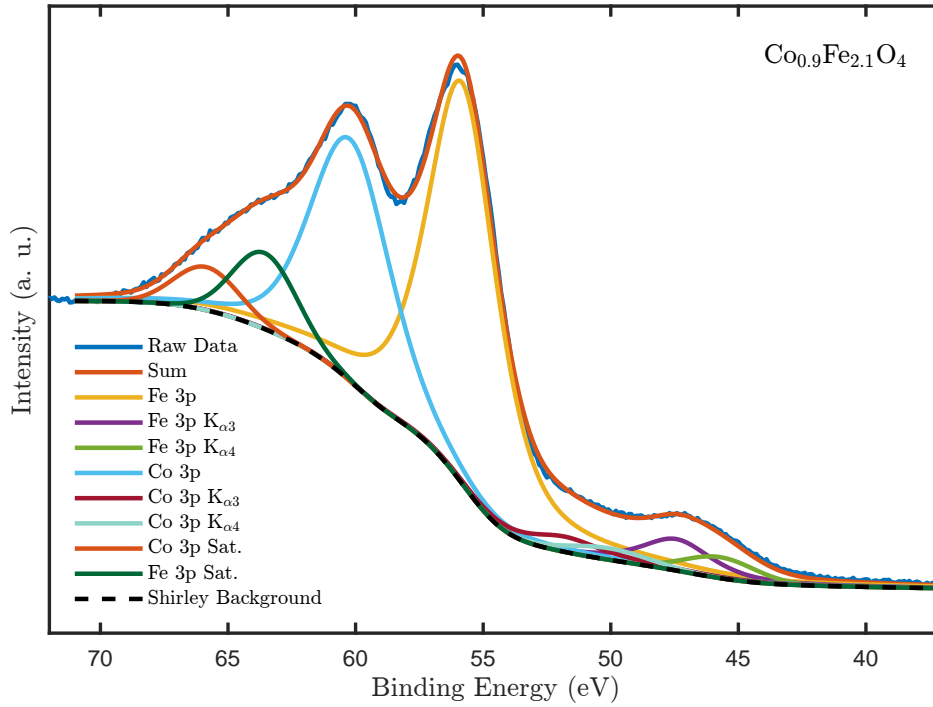


**Figure 5.1:** Exemplary analysis of a Fe 3p and Co 3p XP spectrum. A Shirley background was assumed. The main peaks were fitted with a single Pseudo-Voigt function, since the doublet structure of the peaks due to spin-orbit coupling cannot be resolved. In addition, one satellite was assumed for each main peak. Since a non-monochromatic X-ray source was used, the impact of higher excitations ( $K_{\alpha 3}$  and  $K_{\alpha 4}$ ) have been taken into account for the Fe 3p and Co 3p main peaks. The  $K_{\alpha 3}$  peaks for the Co 3p and Fe 3p satellites have also been taken into account, however, to increase the plots clarity they were not included in the plot.

According to McIntyre et al. the Fe 3p main peak is located at a binding energy of  $(55.9 \pm 0.2)$  eV and shows a clear asymmetric shape. In addition, a satellite is reported to be at a binding energy located about 7 eV higher than the 3p peak. This satellite cannot be explained by multiplet splitting, but rather by electron correlation effects [27].

According to Kim et al. the Co 3p peak consists of one 3p main line located at a binding energy of  $(60.4 \pm 0.2)$  eV. Additionally, there is a Co 3p satellite, which is located between 64.4 eV and 69.5 eV and is caused by multiplet splitting and by multielectron excitation [21].

The aforementioned signals are taken into account in the reconstruction. In addition, other contributions due to the non-monochromatic X-ray source have to be considered. For this analysis, the Fe 3p and Co 3p peak due to the  $K_{\alpha 3}$  and  $K_{\alpha 4}$  excitation lines are considered. Moreover, both satellites due to the  $K_{\alpha 3}$  excitation are taken into account. Satellites due to  $K_{\alpha 4}$  are neglected because they are very small compared to the 3p main peaks. However, the intensity and shape of these contributions are linked to the respective peaks via constraints (cf. Sec. 4.3). In sum, the 3p region is approximated with ten signals, which leads to a relatively high inaccuracy. Although the binding energies of the peaks are known relatively precisely from the work of Kim and McIntyre, other parameters such as the peak shape (Gaussian or Lorentzian), the FWHM or the peak area remain unspecified. Taking into account all the contributions, the Co content  $x$  of the  $\text{Co}_x\text{Fe}_{3-x}\text{O}_4$  films can be determined by

multiplying the intensity ratio (cf. Eq. (5.1)) by three. This results in the stoichiometries shown in Fig. 5.2. The uncertainty of  $x$  is estimated to be at least 0.2.

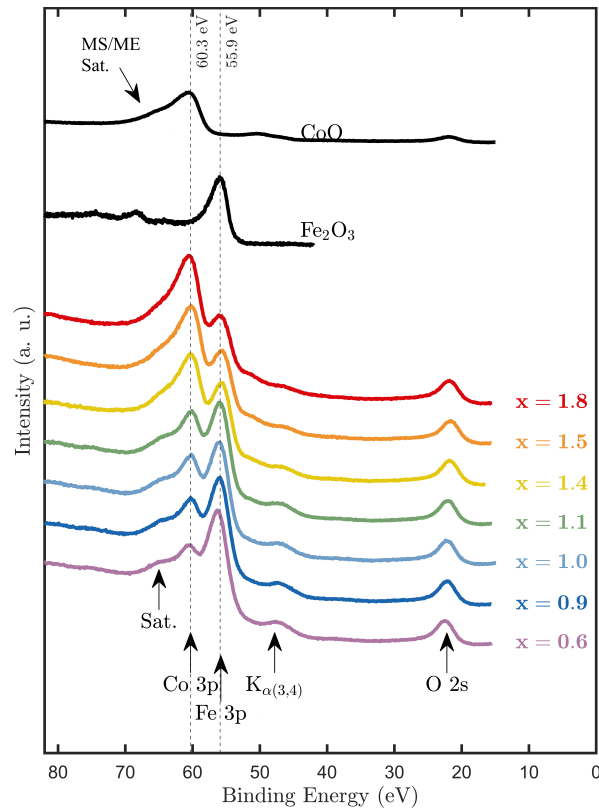


**Figure 5.2:** Co 3p, Fe 3p and O 2s spectra of all prepared  $\text{Co}_x\text{Fe}_{3-x}\text{O}_4$  films. The splitting of the 3p peaks due to the spin orbit coupling can not be resolved. The vertical dashed lines denote the energy of the respective 3p peak. The Co 3p satellite of the CoO reference sample is clearly visible, however, the Fe 3p satellite is barely observable for the  $\text{Fe}_2\text{O}_3$  reference sample.

Fig. 5.2 shows the XP spectra of the Fe 3p/Co 3p region for all  $\text{Co}_x\text{Fe}_{3-x}\text{O}_4$  films, including the O 2s signals. All spectra have been calibrated according to the C 1s core-level at 285 eV binding energy. Reference spectra of a CoO and a  $\text{Fe}_2\text{O}_3$  sample are added for comparison. The binding energy of the Co 3p signal is  $(60.3 \pm 0.2)$  eV and is independent of the Co content  $x$ . The binding energy of the Fe 3p peak is  $(55.9 \pm 0.2)$  eV and is also constant for all samples. With increasing  $x$ , the intensity of the Co 3p signal increases constantly, whereas the intensity of the Fe 3p peak decreases, which is expected due to the rising Co content in the films.

### 5.1.2 Qualitative analysis of the Fe 2p core-level spectra

Due to a larger spin-orbit coupling compared to the 3p spectra, the Fe 2p signal shows a doublet structure, consisting of a Fe  $2p_{3/2}$  peak and a Fe  $2p_{1/2}$  peak. It has been shown in previous studies [58] that the peak positions of Fe  $2p_{1/2}$  and Fe  $2p_{3/2}$  depend on the oxidation states of the Fe ion. Both peaks are accompanied by a charge-transfer satellite on their high-energy shoulder. The positions of the satellite peaks are also very sensitive to the oxidation states and these peaks have been used for qualitatively determining the oxidation states of iron [58].

Fig. 5.3 shows the Fe 2p region of all prepared  $\text{Co}_x\text{Fe}_{3-x}\text{O}_4$  ( $0.6 \leq x \leq 1.8$ ) films and, for comparison, Fe 2p reference spectra of the most common iron oxides ( $\text{Fe}_3\text{O}_4$ ,  $\text{Fe}_2\text{O}_3$  and  $\text{FeO}$ ). All spectra have been calibrated according to the C 1s core-level at 285 eV binding energy.

$\text{FeO}$  is expected to contain only divalent iron, whereas  $\text{Fe}_2\text{O}_3$  should contain solely trivalent iron. In contrast,  $\text{Fe}_3\text{O}_4$  contains both divalent and trivalent iron. Since the Fe 2p spectra of these species differ greatly as evident in Fig. 5.3, the predominant oxidation state of the iron in the cobalt ferrite films can be determined from the Fe 2p spectra.

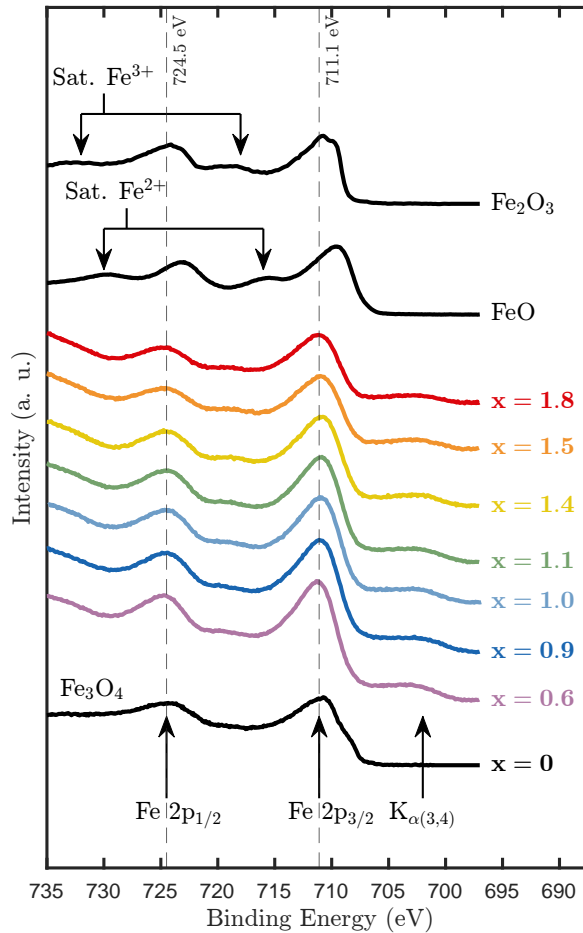


**Figure 5.3:** Fe 2p core-level spectra of all  $\text{Co}_x\text{Fe}_{3-x}\text{O}_4$  films. Due to spin-orbit coupling, Fe 2p<sub>1/2</sub> and Fe 2p<sub>3/2</sub> peaks are evident. The vertical dashed lines denote the energy of the respective peak. Reference spectra of  $\text{Fe}_3\text{O}_4$ ,  $\text{Fe}_2\text{O}_3$ ,  $\text{FeO}$  are shown in black.

The binding energies of the main peak of  $\text{Fe}_2\text{O}_3$  are reported to be between 710.6 eV to 711.2 eV for Fe 2p<sub>3/2</sub> and 724.6 eV for Fe 2p<sub>1/2</sub>. Similar values are reported for  $\text{Fe}_3\text{O}_4$ . However,  $\text{FeO}$  deviates significantly from these values. The Fe 2p<sub>3/2</sub> and Fe 2p<sub>1/2</sub> main peaks of  $\text{FeO}$  are located at binding energies of 709.5 eV and 723.2 eV, respectively, which is considerably lower than the main peaks binding energies of  $\text{Fe}_2\text{O}_3$  and  $\text{Fe}_3\text{O}_4$  [58].

Both  $\text{FeO}$  and  $\text{Fe}_2\text{O}_3$  reference spectra show distinct satellite structures at higher binding energy sides of the Fe 2p main peaks. The distance between the  $\text{FeO}$  satellite and the associated Fe 2p peak are about 6 eV. The existence of this shoulder is a clear evidence for the existence of  $\text{Fe}^{2+}$ . In comparison,

the binding energy difference between the Fe 2p<sub>3/2</sub> peak of Fe<sub>2</sub>O<sub>3</sub> and its satellite is about 8 eV, which is an indicator for Fe<sup>3+</sup>. It is noticeable that Fe<sub>3</sub>O<sub>4</sub> does not show any satellite structure between the Fe 2p main peaks. It consists of both divalent and trivalent Fe atoms, so both satellites should in principle appear. The reason why no satellite is visible is the superposition of both peaks, which results in an intensity plateau between the Fe 2p main peaks [58].

For the Co<sub>x</sub>Fe<sub>3-x</sub>O<sub>4</sub> (0.6 ≤ *x* ≤ 1.8) films prepared in this work, the Fe 2p<sub>1/2</sub> and Fe 2p<sub>3/2</sub> peaks are at binding energies of (724.5 ± 0.2) eV and (711.1 ± 0.2) eV, respectively. No significant change of the binding energies with increasing Co content can be observed. Moreover, the Fe 2p spectra reveal for all Co<sub>x</sub>Fe<sub>3-x</sub>O<sub>4</sub> films charge-transfer satellites located at (719 ± 1) eV. The position and shape of the satellite does not change significantly with increasing Co content. The spectra of the prepared cobalt ferrite films are superimposed with a O KLL Auger line and consequently the intensity increases strongly at the Fe 2p<sub>1/2</sub> high-energy shoulder. Due to this superposition, the charge-transfer satellite associated with the Fe 2p<sub>1/2</sub> peak cannot be analyzed thoroughly. Therefore, the Fe 2p<sub>3/2</sub> charge-transfer satellite is mainly used for the analysis of the oxidation state of the Fe cations. The shape of the 2p spectra and the positions of the peaks are comparable to the Fe<sub>2</sub>O<sub>3</sub> reference spectra. This strongly indicates a majority of Fe<sup>3+</sup> cations. Furthermore, the intensity of the main peaks decrease as the Co content *x* increases. This is as expected, since with increasing *x* the Fe content is reduced.

### 5.1.3 Qualitative analysis of the Co 2p core-level spectra

As with the Fe 2p peak, the Co 2p peak splits into two individual components Co 2p<sub>3/2</sub> and Co 2p<sub>1/2</sub> due to spin-orbit coupling. The predominant oxidation state of the Co cations can be derived using the Co 2p spectra. It is known from previous studies that the Co 2p spectra of the most common cobalt oxides CoO and Co<sub>3</sub>O<sub>4</sub> differ significantly, as CoO contains only Co<sup>2+</sup> and Co<sub>3</sub>O<sub>4</sub> contains both Co<sup>2+</sup> and Co<sup>3+</sup> [5].

In contrast to the position of the Fe 2p peaks, the binding energies of the Co 2p peaks are less indicative for the oxidations state of the Co cations due to similar chemical shifts of CoO and Co<sub>3</sub>O<sub>4</sub>. Rather, the corresponding information can be derived from the positions of the present shake-up satellites which are characteristic for the oxidation state. According to Chuang et al. the binding energies for the shake-up satellites of CoO are 786.4 eV and 803.0 eV, respectively. In contrast, the shake-up satellites for Co<sub>3</sub>O<sub>4</sub> are positioned at 789.5 eV and 804.5 eV and are less pronounced [5]. The binding energies of the Co 2p shake-up satellites therefore differ significantly, making it possible to determine the predominant oxidation state.

Fig. 5.4 shows the Co 2p core-level spectra of the prepared Co<sub>x</sub>Fe<sub>3-x</sub>O<sub>4</sub> (0.6 ≤ *x* ≤ 1.8) samples and, for comparison, a CoO reference spectrum. All spectra have been calibrated according to the C 1s core-level at 285 eV binding energy. The binding energy of the Co 2p<sub>1/2</sub> peak is (796.0 ± 0.2) eV for all cobalt ferrite samples, whereas the binding energy of the Co 2p<sub>3/2</sub> is (780.3 ± 0.2) eV. The determined binding energies agree within the limits of inaccuracy with the work of Chuang [5]. However, as mentioned above, the main peak binding energies cannot be used to determine the predominant oxidation state. For this reason the binding energies of the shake-up satellites are determined. The Co 2p<sub>3/2</sub> shake-up satellite is centered at (786.4 ± 0.2) eV and the Co 2p<sub>1/2</sub> shake-up is positioned

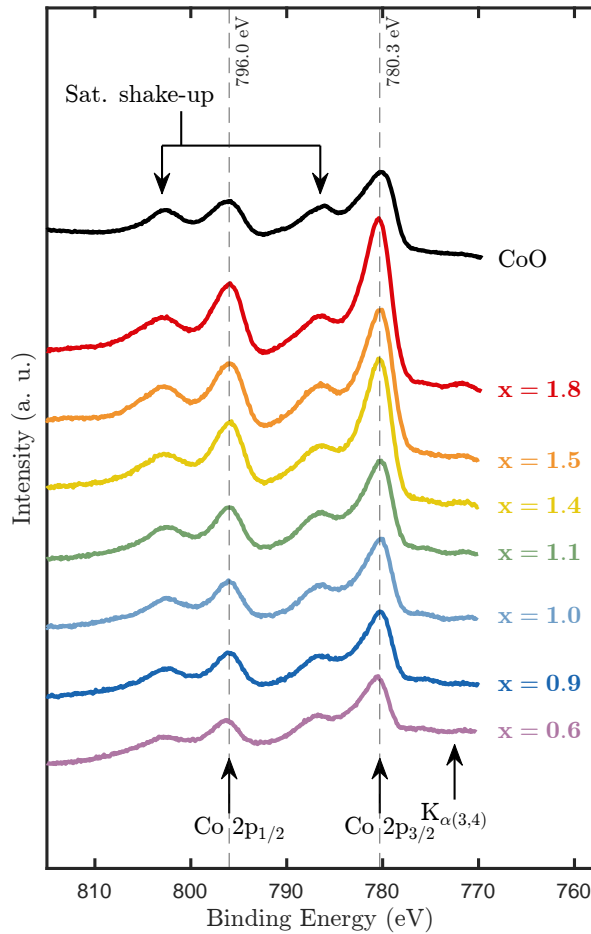


**Figure 5.4:** Co 2p core-level spectra of the prepared  $\text{Co}_x\text{Fe}_{3-x}\text{O}_4$  films. Due to spin-orbit coupling, a Co  $2p_{1/2}$  and a Co  $2p_{3/2}$  peak with the respective shake-up satellites can be seen. The vertical dashed lines denote the energy of the respective peak.

at  $(803.0 \pm 0.2)$  eV. Thus, the binding energies of the shake-up satellites agree with the positions of the CoO shake-up satellites, considering experimental uncertainties. Consequently, the predominant oxidation state of Co in the prepared cobalt ferrite films is  $\text{Co}^{2+}$ .

Moreover, studies by Nlebedim et al. showed that increasing the Co content  $x$  beyond  $x = 1.0$  leads to a coexistence of  $\text{Co}^{2+}$  and  $\text{Co}^{3+}$  [31]. Increasing  $x$  beyond 1.0 should therefore manifest itself in a shake-up satellite shift and in a decrease in the satellite intensity. This, however, cannot be confirmed for the  $\text{Co}_x\text{Fe}_{3-x}\text{O}_4$  ( $0.6 \leq x \leq 1.8$ ) samples prepared in this work. Neither the satellites nor the main peaks undergo a significant change in binding energies. Still, the increasing  $x$  is manifesting itself in the Co 2p peak intensity, which increases as  $x$  increases.

#### 5.1.4 Qualitative analysis of the valence band

Fig. 5.5 shows the valence band (VB) of CoO and  $\text{Fe}_3\text{O}_4$  reference samples as well as the VB of the prepared  $\text{Co}_x\text{Fe}_{3-x}\text{O}_4$  ( $0.6 \leq x \leq 1.5$ ) films. All spectra have been calibrated according to the C 1s core-level at 285 eV binding energy. All VB consist of main band ranging from 0 eV to about 15 eV.

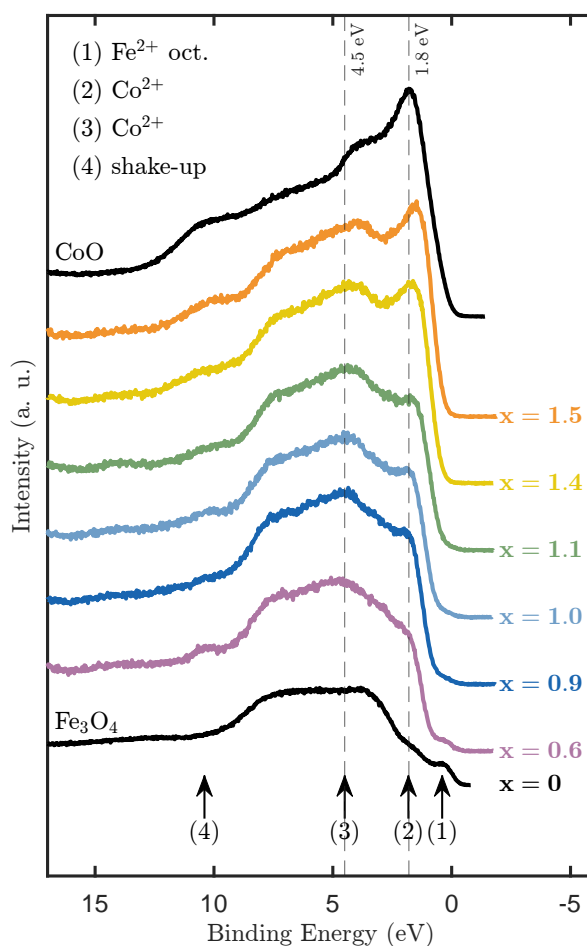
Feature (1), located at a binding energy of about  $(0.4 \pm 0.1)$  eV, is seen exclusively in the  $\text{Fe}_3\text{O}_4$  VB and in the  $\text{Co}_x\text{Fe}_{3-x}\text{O}_4$  ( $x < 1.0$ ) XP spectra. This peak is linked to the existence of octahedrally



coordinated  $\text{Fe}^{2+}$  cations [33]. Feature (1) becomes smaller with increasing Co content  $x$  and disappears completely at  $x = 1$ . From this observation, it can be assumed that the number of octahedrally coordinated  $\text{Fe}^{2+}$  cations is shrinking with increasing  $x$ . It can be concluded that Co cations substitute for  $\text{Fe}^{2+}$  cations on the octahedral sites as  $x$  increases.

The VB spectrum of CoO has a complicated shape because many individual attributions overlap. According to Chuang et al. [5] and Kim et al. [21], feature (2) as well as feature (3) are caused by 3d electrons emitted from  $\text{Co}^{2+}$  cations. Therefore, it is not unexpected that these features are not found in the  $\text{Fe}_3\text{O}_4$  VB spectrum. Additionally, feature (2) increases significantly with increasing Co content and furthermore the peak shifts to lower binding energies as  $x$  increases. It has been shown that for  $x > 1$   $\text{Co}^{2+}$  and  $\text{Co}^{3+}$  ions can coexist in cobalt ferrite [31], so it can be assumed that the shift of feature (2) is related to an increase of the amount of  $\text{Co}^{3+}$  cations.

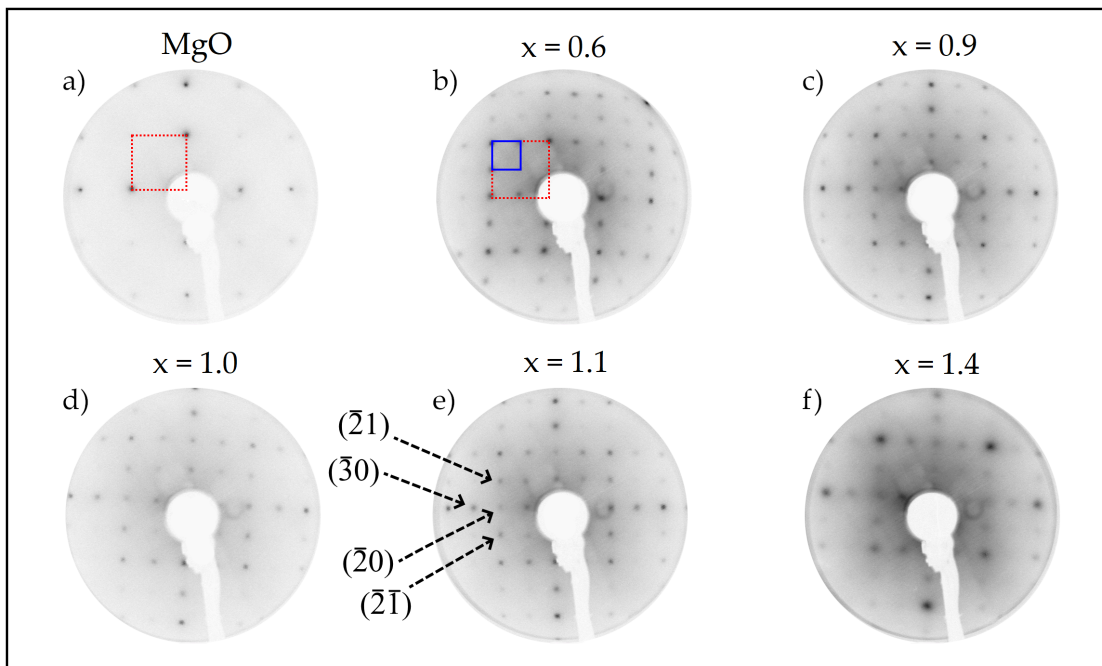
Feature (4) at a binding energy of about 10 eV is due to a shake-up process ( $\text{O } 2p \rightarrow \text{Co } 3d$ ) [21]. Consequently, feature (4) is more pronounced the higher the Co content  $x$  of the cobalt ferrite films. All spectra are superimposed by broad O 2p emission, located between 2 eV and 8 eV binding energy [33].



**Figure 5.5:** Valence band XP spectra of  $\text{Co}_x\text{Fe}_{3-x}\text{O}_4$  ( $0.6 \leq x \leq 1.5$ ). CoO and  $\text{Fe}_3\text{O}_4$  reference spectra are shown in black.

## 5.2 LEED results

LEED measurements to analyze the surface structure of the  $\text{Co}_x\text{Fe}_{3-x}\text{O}_4$  films are performed *in situ* in an electron energy range from approximately 150 eV to 300 eV. Prior to film preparation, the cleaned MgO(001) substrates were analyzed by LEED to investigate the quality of the substrate surfaces and to check for the existence of unwanted adsorbates. Since the individual LEED patterns of the substrates do not differ significantly, only one pattern is shown as an example. Fig. 5.6 a) shows the pattern of a cleaned MgO(001) substrate acquired at 165 eV. The pattern reveals a low background intensity with sharp and high-contrast reflexes. This implies a well-ordered surface structure with only few defects. In addition, the  $(1 \times 1)$  structure (drawn in red) is visible, indicating a square surface unit cell.



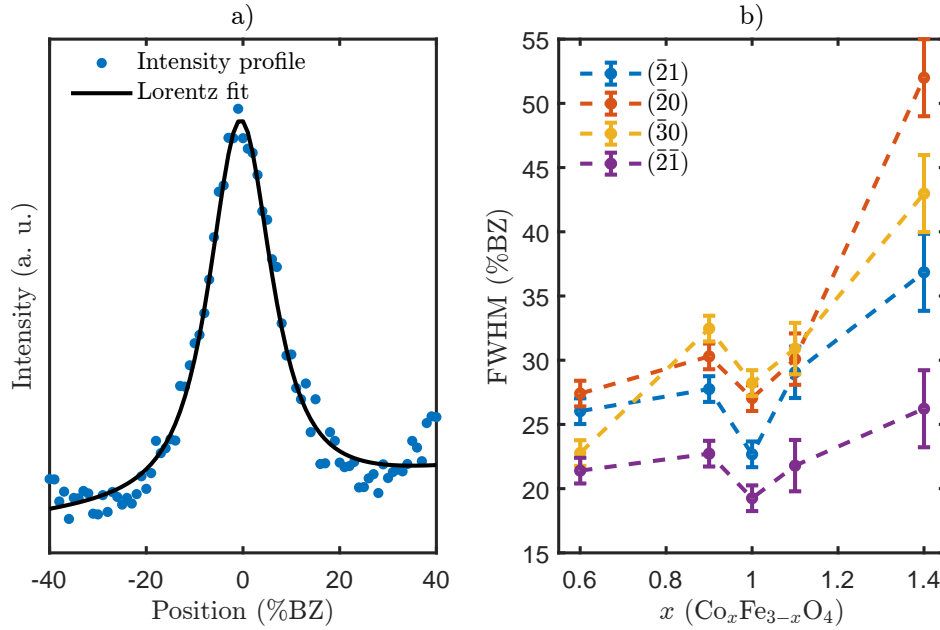
**Figure 5.6:** LEED pattern of a MgO(001) substrate and  $\text{Co}_x\text{Fe}_{3-x}\text{O}_4$  on MgO(001) samples with varying Co content  $x$ . a) shows the diffraction pattern of the substrate with the square unit cell drawn in red and in b) - f) the CFO LEED pattern are shown. The cubic unit cell of CFO is drawn in blue. The patterns were acquired at an electron energy of 165 eV. The arrows in e) point to the spots which are analyzed using a Lorentzian reconstruction.

Fig. 5.6 b) - f) show the  $\text{Co}_x\text{Fe}_{3-x}\text{O}_4$  ( $0.6 \leq x \leq 1.4$ ) LEED patterns. Samples with  $x > 1.4$  could not be analyzed because they were strongly charged, pointing to an increased insulating character the higher the amount of Co in the cobalt ferrite films. All patterns show a  $(1 \times 1)$  surface structure (drawn in blue), suggesting a cubic surface unit cell. It is noticeable that the reciprocal unit cell length of MgO is approximately twice the reciprocal unit cell length of cobalt ferrite. The reason for this is the unit cell length in real space. It is 8.392 Å for  $\text{CoFe}_2\text{O}_4$  [22] and thus about twice as large as the unit cell length of MgO with 4.2117 Å [13].

In addition, an increased background intensity with increasing Co content  $x$  is observable. However, the stoichiometric cobalt ferrite sample with  $x = 1.0$  (cf. Fig. 5.6 d)) seems to have a lower background intensity than the non-stoichiometric samples. The higher background intensity combined

with a larger spot width suggests that with increasing Co content the crystalline surface becomes more disordered and more defective [32].

This observation can be quantitatively confirmed with a LEED spot analysis. An intensity profile along the spot cross-section is created for selected spots and subsequently the profile is reconstructed using Lorentzians. The FWHM of the intensity profiles are evaluated, since the widths of the peaks provide information about the ordering of the surface and scale with the defect density. Fig. 5.7 a) shows an representative intensity profile of one LEED spot with Lorentzian reconstruction and linear background.



**Figure 5.7:** a) Intensity profile (blue) of a LEED spot cross-section and Lorentzian reconstruction (black) with linear background (not shown in the figure). b) FWHM of the intensity profiles of selected LEED spots as a function of the Co content  $x$ . The FWHM is normalized to the first Brillouin zone.

In Fig. 5.7 b) it can be seen that the FWHM of all analyzed spots increases overall almost continuously with increasing Co content  $x$ . However, it is striking that all spots show a sharp decrease in FWHM at  $x = 1.0$ , manifesting as a dip in the FWHM curve for all spots. It might be suggested that the crystalline surface of stoichiometric cobalt ferrite is better ordered and has fewer defects than the non-stoichiometric samples. It is also evident that for strongly overstoichiometric samples ( $x > 1.0$ ), the FWHM of the spots increases dramatically to as high as 53%BZ, pointing to a more disordered and defective surface.

### 5.3 XRR results

The film thicknesses of the  $\text{Co}_x\text{Fe}_{3-x}\text{O}_4$  ( $0.6 \leq x \leq 1.8$ ) samples are determined by XRR measurements in  $\theta - 2\theta$  geometry. The  $\theta$ -dependence of the intensity measurement was converted to a scattering vector  $q$ -dependence using Eq. (2.39). Fig. 5.8 shows the measured data and the corresponding fits.

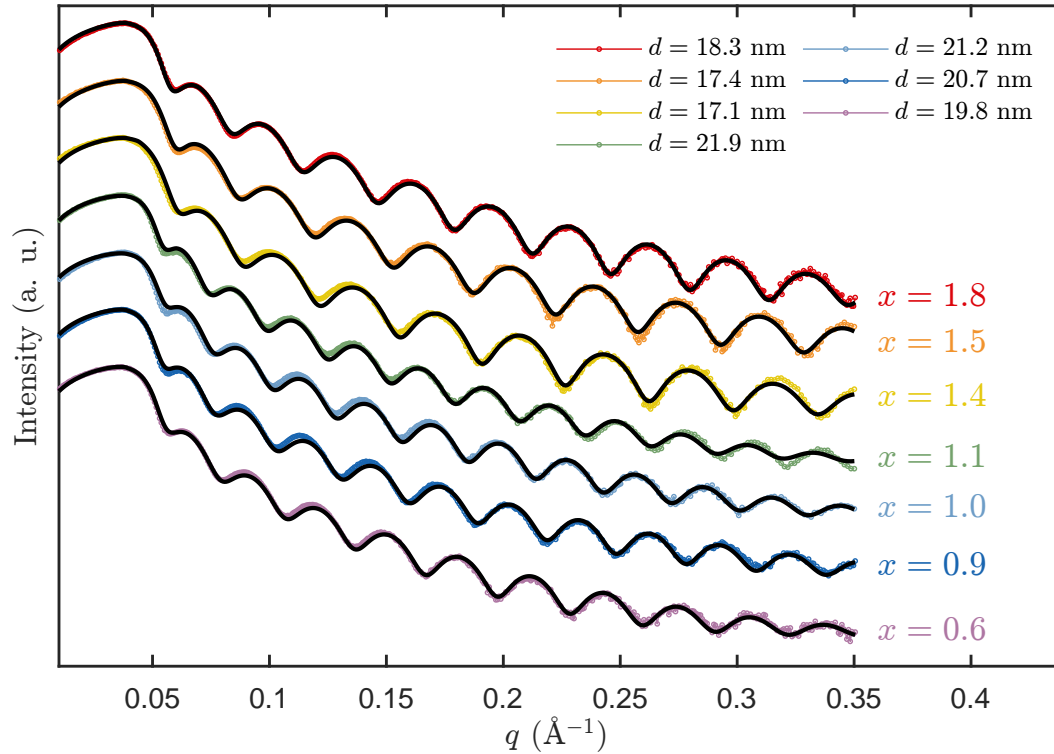


**Figure 5.8:** XRR measurement of all prepared  $\text{Co}_x\text{Fe}_{3-x}\text{O}_4$  ( $0.6 \leq x \leq 1.8$ ) samples. The intensity curve suggests a monolayer system. The reconstructed intensity curves are shown in black.

The intensity as a function of the scattering vector  $q$  clearly shows oscillations, called Kiessig fringes, which are caused by constructive and destructive interferences from smooth film and substrate interfaces, as described in Sec. 2.5.3. All samples show a single periodicity, indicating a monolayer system. Due to almost matching periods, it can be assumed that the film thicknesses are of the same order of magnitude.

For the exact determination of the film thicknesses the measured intensity is analyzed with the software iXRR [1]. This software reconstructs the intensity profile and accepts the complex refractive index of film material and substrate material as fitting parameters, as well as the film thickness and the surface roughness of film and substrate. The literature values of the complex refractive index of MgO and stoichiometric cobalt ferrite [16] are set as the initial value for the approximation algorithm and a deviation of 5% is allowed for the cobalt ferrite refractive index during the fitting procedure. The film thickness as well as roughnesses were left completely variable.

The fitting algorithm therefore contains a large number of parameters, which has a negative effect on reproducibility. The roughness parameter varied too much between different fit runs to be evaluated in a meaningful way. Furthermore, it is not clear to what extent the stoichiometry of the cobalt ferrite films influences the complex refractive index. However, the thicknesses were perfectly reproducible. The film thicknesses of all samples are comparable with  $(19.5 \pm 2.4)$  nm.

## 5.4 UV-Vis results

The optical properties of the  $\text{Co}_x\text{Fe}_{3-x}\text{O}_4$  ( $0.6 \leq x \leq 1.5$ ) samples are investigated using UV-Vis spectroscopy and Tauc plots. The basis of this method is the measurement of the transmission  $T$  and reflectance  $R$  of both the film-substrate system and the substrate alone. From the transmission and reflectance data, the energy-dependent absorption coefficient  $\alpha(h\nu)$  can be extracted. A Tauc plot  $((\alpha h\nu)^{1/n}$  vs.  $h\nu$ ) can subsequently be used to determine the direct ( $n = 1/2$ ) and indirect ( $n = 2$ ) band gaps.

Fig. 5.9 a) shows exemplarily the transmission  $T$  of MgO(001) and  $\text{Co}_{0.6}\text{Fe}_{2.4}\text{O}_4/\text{MgO}(001)$ . Note, that the  $\lambda$ -axis is in reverse. Up to a wavelength of 355 nm (2), the transmission of the MgO(001) substrate is approximately constant with about 80%. After that, the transmission drops rapidly to about 0%. The transmission of  $\text{Co}_{0.6}\text{Fe}_{2.4}\text{O}_4/\text{MgO}(001)$  shows a slightly different behaviour. From a wavelength of about 890 nm (1), the transmission decreases approximately linearly to about 30%. After that, the transmission of  $\text{Co}_{0.6}\text{Fe}_{2.4}\text{O}_4/\text{MgO}(001)$  also drops to about 0%.

Fig. 5.9 b) shows the reflectance  $R$  as a function of  $\lambda$ . The reflectance of  $\text{Co}_{0.6}\text{Fe}_{2.4}\text{O}_4/\text{MgO}(001)$  and MgO(001) are increasing with decreasing wavelength. At wavelengths smaller than 800 nm the reflectance of  $\text{Co}_{0.6}\text{Fe}_{2.4}\text{O}_4/\text{MgO}(001)$  is greater than the reflectance of MgO. (3) points to a measurement inaccuracy because the light source of the spectrometer changes at this wavelength. At a wavelength of about 245 nm (4), a dip can be observed in the reflectance curve of MgO. However, this dip is not observable for  $\text{Co}_{0.6}\text{Fe}_{2.4}\text{O}_4/\text{MgO}(001)$ .

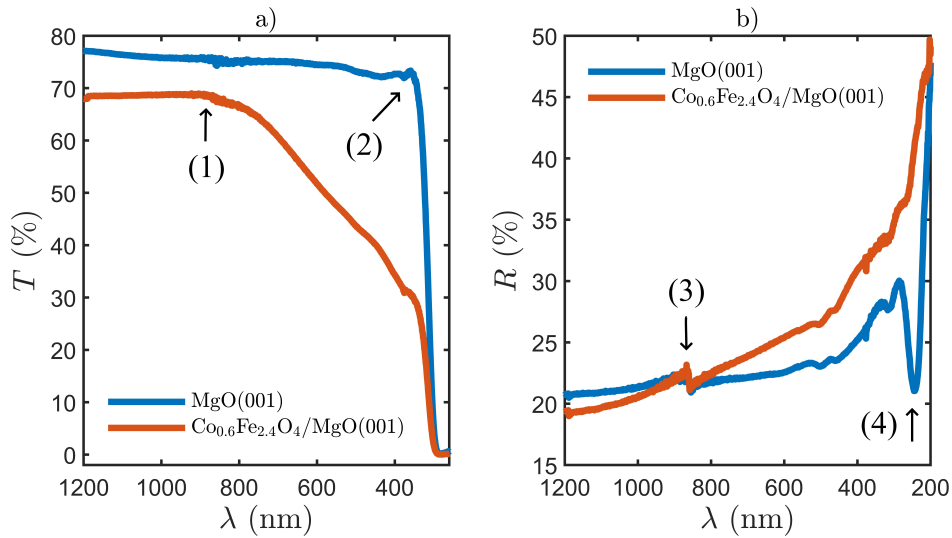


**Figure 5.9:** Transmission  $T$  and reflectance  $R$  as a function of wavelength  $\lambda$  of the MgO(001) substrate and the  $\text{Co}_{0.6}\text{Fe}_{2.4}\text{O}_4/\text{MgO}(001)$  system.

The absorption coefficient  $\alpha$  can be calculated from  $T$  and  $R$  using Eq. (2.36). Fig. 5.10 shows  $\alpha(h\nu)$  of the MgO substrate as well as of a  $\text{Co}_{0.6}\text{Fe}_{2.4}\text{O}_4/\text{MgO}(001)$  sample. The absorption coefficient of the MgO substrate is nearly constant up to an energy of about 3.5 eV. At photon energies greater than 3.5 eV, the coefficient increases precipitously. The reason for this sharp increase can only be speculated, as the optical band gap for bulk MgO is typically around 7.8 eV [40]. It may originate from color centers, crystal defects or other unspecified sub-band transitions.

The absorption coefficient of the  $\text{Co}_{0.6}\text{Fe}_{2.4}\text{O}_4/\text{MgO}(001)$  sample shows a similar curve as the MgO substrate. There is also a strong increase at about 3.5 eV, which can be attributed to the MgO. However, it is also clearly evident that the absorption coefficient increases from about 1.5 eV, which could not be observed with the pure MgO sample. From this it can be deduced that this is related to the cobalt ferrite film.

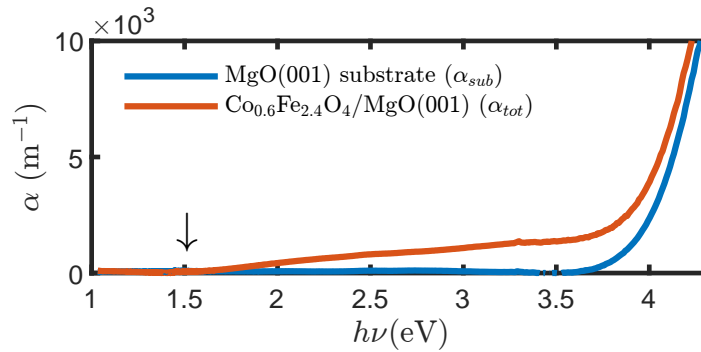


**Figure 5.10:** Comparison between the energy dependent absorption coefficient curves of the MgO(001) substrate ( $\alpha_{sub}$ ) and the  $\text{Co}_{0.6}\text{Fe}_{2.4}\text{O}_4/\text{MgO}(001)$  system ( $\alpha_{tot}$ ). Both curves increase rapidly from an energy of about 3.5 eV. The absorption coefficient of the  $\text{Co}_{0.6}\text{Fe}_{2.4}\text{O}_4/\text{MgO}(001)$  sample (red) additionally shows an increase starting at about 1.5 eV (see arrow).

#### 5.4.1 Determination of direct and indirect band transitions

To determine the direct band gaps of the  $\text{Co}_x\text{Fe}_{3-x}\text{O}_4$  ( $0.6 \leq x \leq 1.5$ ) thin films, the squared product of the absorption coefficient and the photon energy  $(\alpha h\nu)^2$  is plotted against the photon energy  $h\nu$ . One exemplary Tauc plot of the  $x = 1.5$  sample is shown in Fig. 5.11. The plot shows two regions with different slopes (plotted in red and blue) which are found in all samples. It can be speculated that the two different slopes indicate two different optical transitions. Based on the red slope, direct band gaps between  $(1.91 \pm 0.03)$  eV and  $(1.95 \pm 0.03)$  eV can be determined by analyzing the intersection of the linear fit with the zero line. This value is very consistent with the value of 1.95 eV documented for a CFO/SrTiO<sub>3</sub> system [19]. The band gap increases slightly with increasing  $x$  (cf. Fig. 5.12 a)), however, no clear trend can be identified. Based on the blue slope, direct band gaps between  $(2.62 \pm 0.07)$  eV and  $(2.73 \pm 0.07)$  eV are obtained. The band gap increases almost linearly as  $x$  increases (cf. Fig. 5.12 b)). A similar value of 2.6 eV was reported for a CFO/LaAlO<sub>3</sub>(001) system [37].

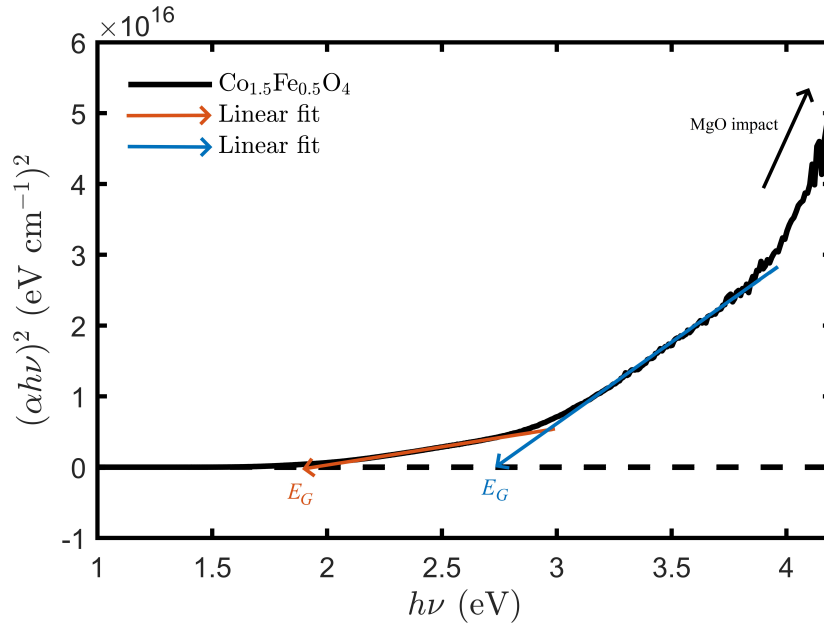


**Figure 5.11:** Tauc plot ( $(\alpha h\nu)^2$  vs.  $h\nu$ ) to determine the direct band gaps. Two regions with linear slope are visible. The red region is linearly fitted from 2.2 eV to 2.7 eV and the blue region is fitted from 3.1 eV to 3.9 eV.

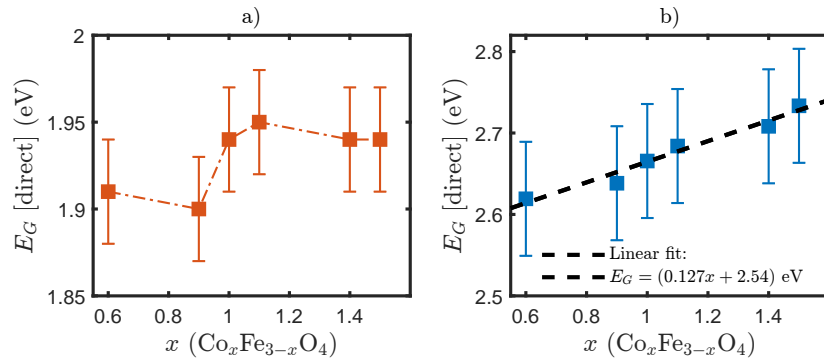


**Figure 5.12:** Direct band gaps  $E_G$  as a function of the Co content  $x$  determined via the red a) and blue b) slope.

To determine the indirect band gap,  $(\alpha h\nu)^{0.5}$  is plotted against  $h\nu$ . Fig. 5.13 shows an exemplary Tauc plot ( $x = 0.6$ ) which is linearly fitted from 1.6 eV to 2.2 eV. The indirect band gap is again obtained from the intersection of the linear fit with the zero line. The Tauc plot shows two (or even three) distinct slopes, resulting in a characteristic S-shape which was present in all prepared samples. This observation typically arises from a phonon involvement in the optical transition [19].

As shown in Fig. 5.14, the indirect band gap  $E_G$  decreases with increasing  $x$ . The sample with the lowest Co content ( $x = 0.6$ ) has a band gap of  $(1.53 \pm 0.03)$  eV, which then decreases approximately linearly with increasing  $x$ . The stoichiometric CFO sample ( $x = 1.0$ ) can be characterized with an indirect band gap of  $(1.45 \pm 0.03)$  eV. A similar value is documented by Himcinschi et al. [19] who reported an indirect band gap of  $(1.42 \pm 0.03)$  eV for stoichiometric cobalt ferrite on Nb-doped SrTiO<sub>3</sub>, which is in excellent agreement with  $E_G$  obtained for stoichiometric cobalt ferrite.

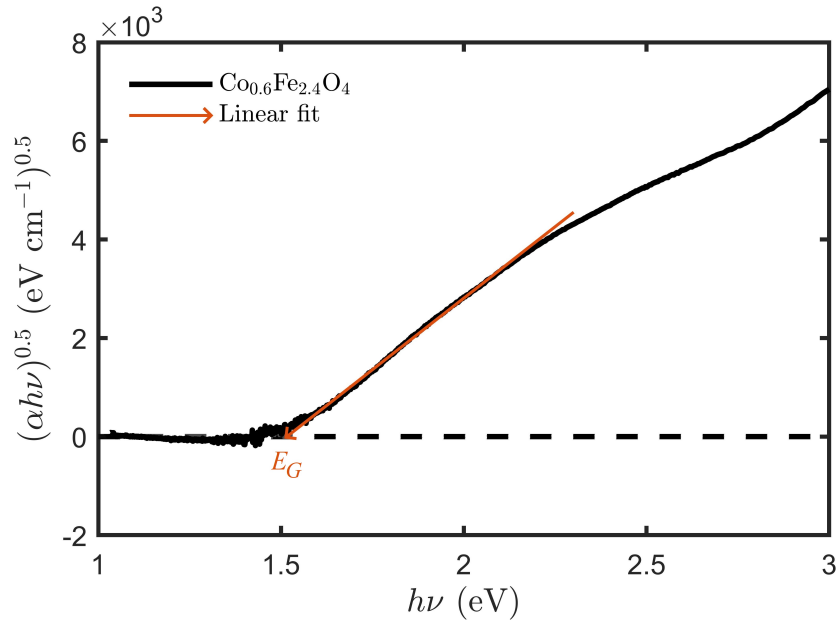


**Figure 5.13:** Tauc plot ( $(\alpha h\nu)^{0.5}$  vs.  $h\nu$ ) to determine the first indirect band gap. The data is fitted from 1.6 eV up to 2.2 eV.

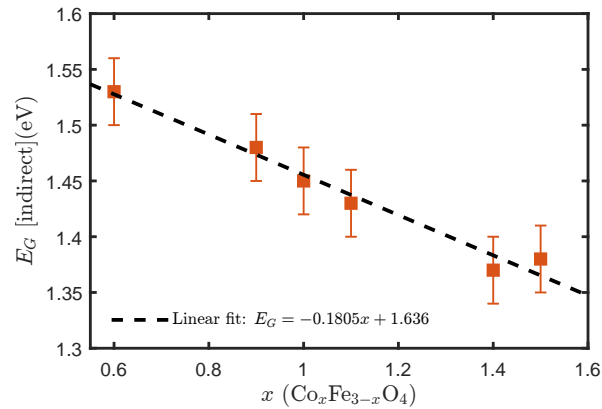


**Figure 5.14:** First indirect band gaps of  $\text{Co}_x\text{Fe}_{3-x}\text{O}_4$  as a function of the Co content  $x$ .

Many studies show that the optical band gaps of ferrites depend on several parameters. It has been reported that the band gap is strongly temperature dependent due to spin charge coupling effects [35]. In addition, studies show that a decrease in the cobalt ferrite film thickness results in an increase in the optical band gap. This is explained by quantum size effects and misfit dislocations [37]. Since the temperature was kept constant during the measurement and the thickness of the individual cobalt ferrite samples does not vary much, these factors are probably negligible.

The optical band gap of ferrites is due to  $d-d$  transitions [60]. The cations are in a crystal lattice and the surrounding crystal field caused by the surrounding oxygen ligands splits the  $d$  level into an  $e_g$  and a  $t_{2g}$  level. The energy difference between  $e_g$  and  $t_{2g}$  is different for octahedral and tetrahedral coordinated cations and therefore it can be deduced that the cation distribution among the A and B sites has a strong influence on the optical band gaps. For instance, Sharma et al. have shown that the direct optical band gap of cobalt ferrite is strongly dependent on the  $\text{Co}^{2+}$  distribution between the



octahedral and tetrahedral sites [45].

It has been mentioned that in Co-rich ( $x > 1$ ) cobalt ferrite films additional crystalline rock salt phases ( $\text{Co}_{1-y}\text{Fe}_y\text{O}$ ) are formed [31]. This phase has a different crystalline structure and therefore a different electronic structure. Thus, this most likely has a strong influence on the change of the band gap.

To investigate the cause of the change in the band gap more precisely, further experiments are necessary. For example, structural analysis by diffraction methods, Raman spectroscopy or Mössbauer spectroscopy as well as XMCD measurements could be used to analyze the cation distribution in detail.

## 5.5 Temperature dependent sheet resistivity

Using the van der Pauw method, the sheet resistivities of the  $\text{Co}_x\text{Fe}_{3-x}\text{O}_4$  ( $0.6 \leq x \leq 1.1$ ) films are measured as a function of temperature, ranging between 100 and 278 K. Samples with  $x > 1.1$  could not be measured because the resistivities were too high for the given setup, which is reconcilable with the assumed increasing insulating character for these films based on the prior LEED results (cf. Sec. 5.2). Fig. 5.15 shows the variation of resistivity  $\rho$  as a function of temperature  $T$ .

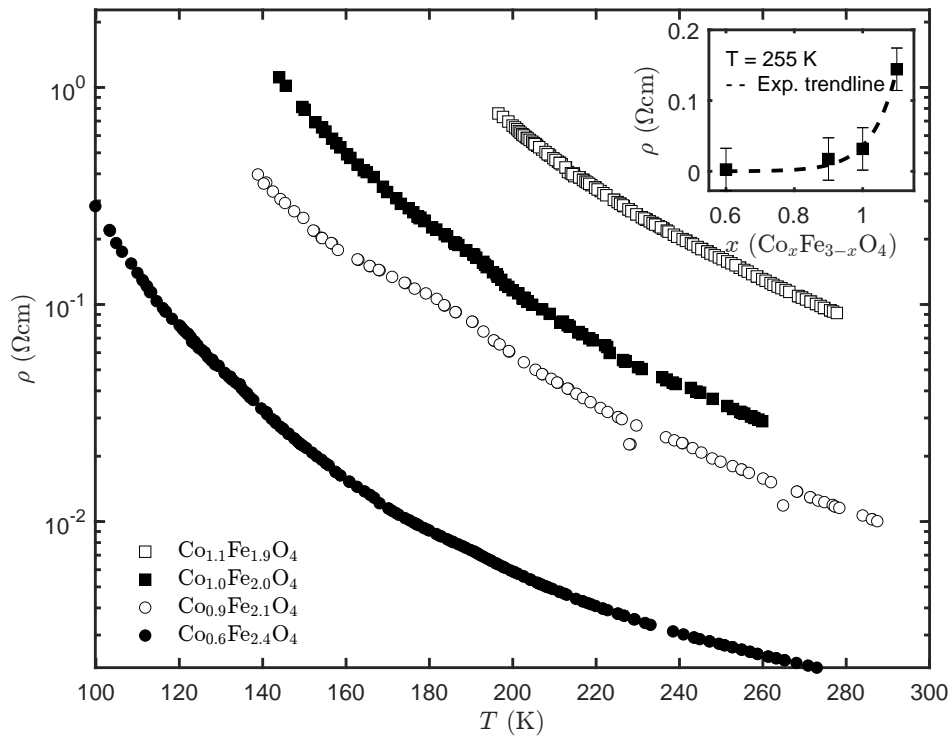


**Figure 5.15:** Temperature dependence of the electrical resistivity for the  $\text{Co}_x\text{Fe}_{3-x}\text{O}_4$  ( $0.6 \leq x \leq 1.1$ ) thin films. Samples with  $x > 1.1$  could not be measured because the resistivities are too high for the given setup. Note the logarithmic scale for  $\rho$ . The inset shows the resistivity  $\rho$  as a function of the Co content  $x$  at a temperature of 255 K.

All samples show, as expected from cobalt ferrite [20], a semiconducting behaviour, since the resistivity increases exponentially with decreasing temperature. Additionally, the resistivity also increases

with increasing Co content  $x$ . The inset shows the resistivity as a function  $x$  at a temperature of 255 K.  $\rho$  increases exponentially as  $x$  increases.

The conduction in ferrites is mainly attributed to electron hopping from  $\text{Fe}^{3+}$  to  $\text{Fe}^{2+}$  at octahedral B-sites [51]. The amount of such ion pairs depends strongly on the stoichiometry  $x$ . In this work it is found that the resistivity increases exponentially as the stoichiometry increases. When the Co content is increased, the Fe content of the film decreases at the same time, as it can be assumed that with increasing  $x$ , Co cations are substituted for Fe cations. This decreases the number of  $\text{Fe}^{3+}$  and  $\text{Fe}^{2+}$  pairs between which hopping is possible and as a result, the resistivity increases.

However,  $\text{Co}^{3+}$  to  $\text{Co}^{2+}$  charge carrier hopping in cobalt ferrite also contributes to the transport properties [15]. With increasing Co content,  $\text{Co}^{3+}$  to  $\text{Co}^{2+}$  hopping should in principle increase. Still, the resistivity increases strongly with increasing  $x$ . This leads to the assumption, that hopping between Co cations is much more unlikely than hopping between Fe cations.

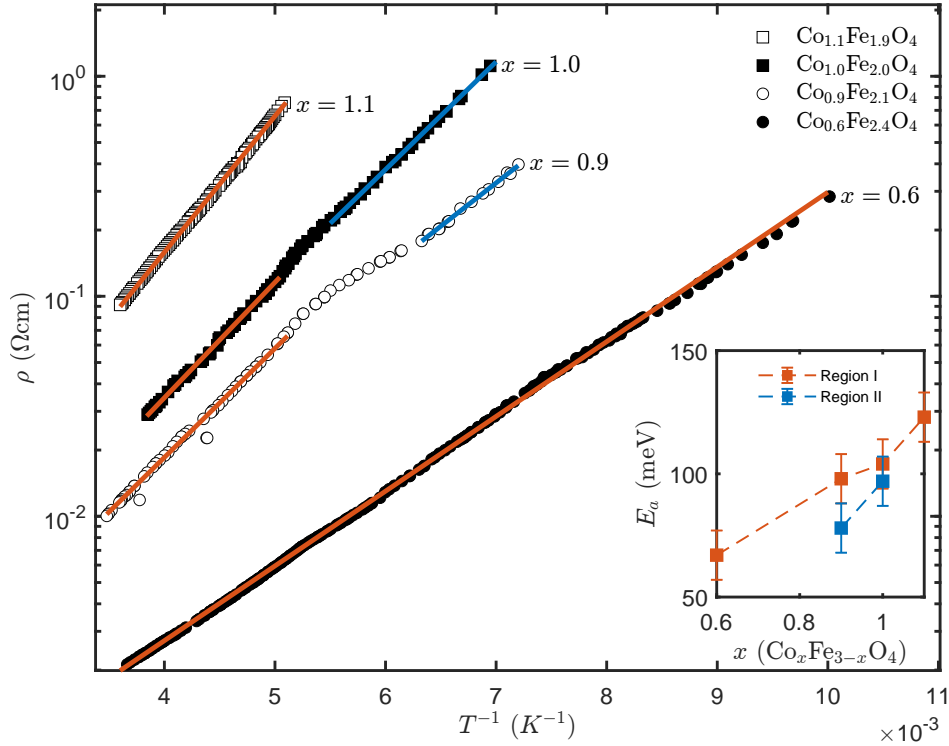


**Figure 5.16:** Temperature dependence of the electrical resistivity shown in an Arrhenius plot ( $\log \rho$  vs.  $1/T$ ) for  $\text{Co}_x\text{Fe}_{3-x}\text{O}_4$  ( $0.6 \leq x \leq 1.1$ ) thin films. The inset shows the dependence of the activation energies resulting from DC resistivity measurements on the Co content  $x$ . Red and blue are fits for the high temperature region and the low temperature region, respectively, for the films exhibiting more than one slope.

In the following, the conduction mechanism of the system will be investigated in more detail. First, the temperature dependent resistivity will be analyzed in a simple Arrhenius plot (cf. Fig. 5.16), meaning that the parameter  $\beta$  in

$$\rho = \rho_0 \exp \left\{ \left( \frac{E_t}{k_B T} \right)^\beta \right\} \quad (5.2)$$

(cf. Sec. 2.4) will be equal to 1 (NNH or band conduction). It is evident that the  $x = 0.6$  and  $x = 1.1$  samples can be fitted very well using a single straight line over the full temperature range. However, the  $x = 0.9$  and  $x = 1.0$  samples show a more complex behaviour. Here the data can only be fitted decently if two different slopes are assumed in a high temperature range and also in a low temperature range. However, different regions with a slope changing have been noticed in conductivity studies for many ferrites [7, 26]. The reason for the kink in the  $\rho$  vs.  $1/T$  plot is not clear. Possible explanations are a change in the conduction mechanism (cf. Sec. 2.4) or a change in the ions involved in the hopping process. Some authors try to explain the kink with the Curie temperature, but this can be excluded in this work, because the Curie temperature for bulk cobalt ferrite is 793 K [55] and the kink is found at a temperature of about 190 K.

From the slopes of the linear regressions, the thermal activation energies  $E_a$  could be determined. The inset in Fig. 5.16 shows the activation energies as a function of the temperature. The activation energies increase constantly with increasing Co content  $x$  for both regions. The  $x = 0.6$  sample has the lowest activation energy with an energy of 67 meV. In contrast, the sample with  $x = 1.1$ , which is the sample with the highest Co content that could still be measured, has an activation energy of 123 meV. These values are comparable to the results of similar studies [3, 46]. The thermal activation energy of nickel ferrite  $\text{NiFe}_2\text{O}_4$  was determined to be 190 meV [3], which is in the same order of magnitude. Furthermore, it has been shown that cobalt ferrite nano powders have an activation energy of 172 meV [46].

It is noticeable that the thermal activation energies are considerably lower than the optical band gaps determined in Sec. 5.4. A similar result was observed by Bougiatioti et al. who determined the band gaps and thermal activation energies of nickel ferrite films using similar methods [3]. The optical band gap is in the range of a few eV, indicating that this is the energy required to excite an electron from the valence band to the conduction band. The thermal activation energy, on the other hand, is much lower in the range of meV. This energy reflects the energy required to excite an electron from the impurity band into the conduction band or to move an electron from one localized site to an adjacent localized site [3].

### 5.5.1 Hopping mechanisms

In the following, the hopping mechanisms of the samples will be analyzed in more detail. Basis of the in-depth analysis is Eq. (2.27). In this equation, the  $\beta$  parameter characterizes the type of the dominant hopping mechanism. For  $\beta = 1$ , band conduction or nearest-neighbor hopping (NNH) is the dominant conduction mechanism. For  $\beta = 0.25$  or  $\beta = 0.5$  the dominating hopping mechanism is Mott-VRH or ES-VRH, respectively (cf. Sec. 2.4).

To determine which hopping mechanism is dominant  $\log \rho$  vs.  $T^{-\beta}$  is plotted. The exponent  $\beta$  is varied from 0.1 to at most 2.7 and the data for each  $\beta$  is fitted by a linear function. The sum of squared estimate of errors (SSE) is a value which characterizes the goodness of the linear fit and it is subsequently plotted as a function of  $\beta$ . Figure 5.17 shows the  $\beta$  dependence of the SSE for all investigated samples.

Samples  $x = 0.6$  and  $x = 1.0$  are analyzed in a  $\beta$  interval of 0.1 to 1.6. However, exponents larger than 1.0 have no physical meaning, but are only used to determine the SSE minimum using a parabola fit. The SSE decreases with increasing exponent  $\beta$ . Both samples show a clear minimum close to  $\beta = 1.0$ . The data is fitted using a parabola to estimate the minimum of the corresponding data. For  $x = 0.6$  and  $x = 1.0$  a minimum of 0.89 and 0.85 could be calculated. These values are close to 1.0 indicating the existence of band conduction or NNH to be the prevailing hopping mechanism. Still, there might be other conduction mechanisms involved, hence the deviation from 1.0.

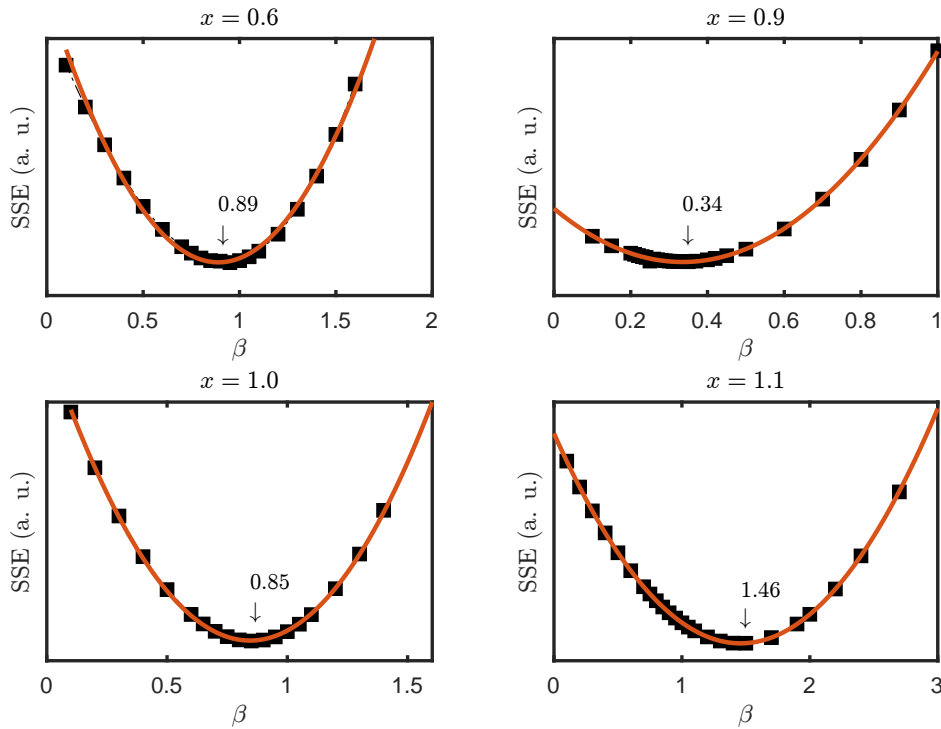


**Figure 5.17:** Sum of squared estimate of errors (SSE) plotted against the exponent  $\beta$  from Eq. (2.27) and fitted with parabolas to determine the minimum.

The SSE of sample  $x = 1.1$  also shows a parabolic behaviour with varying  $\beta$ . The minimum is 1.46. However,  $\beta$  values greater than 1 do not have any physical significance. Therefore, it is not possible for sample  $x = 1.1$  to see a tendency towards a specific hopping mechanism. The  $\beta$  dependence of the SSE of the  $x = 0.9$  sample also shows a parabolic curve. The minimum is estimated to be at  $\beta = 0.34$  and thus deviated significantly from the other samples. It is possible that the conduction mechanism is Mott-VHR or even ES-VHR. However, the calculated minimum does not show a clear tendency. It could also be possible that the value of  $\beta = 0.34$  points to Mott-VRH for 2D sample (cf. Eq. (2.29)).

## 6. Properties of Co-rich cobalt ferrite ultrathin films depending on the O<sub>2</sub> reactive atmosphere during RMBE

In the second part of this thesis, three superstoichiometric cobalt ferrite ultrathin films are grown on MgO(001). By varying the O<sub>2</sub> reactive atmosphere during RMBE, the O content  $\delta$  in the cobalt ferrite films is varied. Samples A, B and C are fabricated at pressures of  $1.0 \times 10^{-5}$  mbar,  $5.0 \times 10^{-6}$  mbar and  $1.0 \times 10^{-6}$  mbar, respectively. Electronic, optical and transport properties of the fabricated films are investigated as a function of pressure.

### 6.1 XPS results

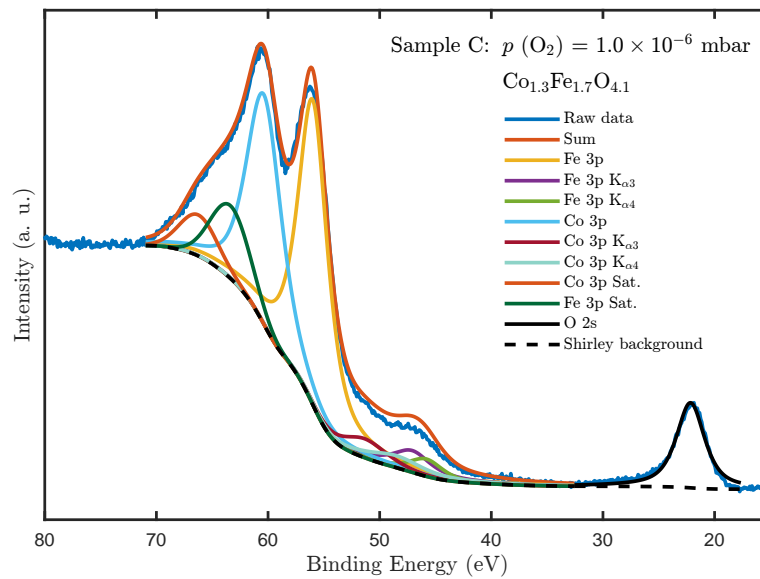


**Figure 6.1:** Exemplary analysis of a Fe 3p, Co 3p and O 2s XP spectrum. A Shirley background was assumed. The main 3p peaks were fitted with a single Pseudo-Voigt function, since the doublet structure of the peaks due to spin-orbit coupling cannot be resolved. In addition, one satellite was assumed for each main peak. Since a non-monochromatic X-ray source was used, the impact of higher excitations ( $K_{\alpha 3}$  and  $K_{\alpha 4}$ ) have been taken into account for the Fe 3p and Co 3p main peaks. The  $K_{\alpha 3}$  peaks for the Co 3p and Fe 3p satellites have also been taken into account, however, to increase the plots clarity they were not included in the plot.

The Co content  $x$  relative to the Fe content of the fabricated cobalt ferrite films is determined from the Fe 3p and Co 3p XP peak intensities. For the determination of  $x$ , the overall 3p spectrum has to

be decomposed into its individual components, as already described in Sec. 5.1.1. The modeling of the peaks is again guided by the results of McIntyre et al. [27] and Kim et al. [21]. Fig. 6.1 shows the modeling of the Co 3p and Fe 3p XP peaks for sample C, prepared at an oxygen atmosphere of  $1.0 \times 10^{-6}$  mbar. Additionally, the O 2s XP peak is included in the spectrum and approximated using a single Pseudo-Voigt function. The Co content  $x$  is determined on the basis of the intensity ratio

$$Y_{Co} = \frac{I_{Co}^{3p}/\sigma_{Co}^{3p}}{I_{Co}^{3p}/\sigma_{Co}^{3p} + I_{Fe}^{3p}/\sigma_{Fe}^{3p}}, \quad (6.1)$$

analogously to Sec. 5.1.1. As expected, all prepared cobalt ferrite ultrathin films are superstoichiometric with a Co content of  $x = (1.3 \pm 0.2)$ . Consequently, the chemical formula of the samples is  $Co_{1.3}Fe_{1.7}O_{\delta}$ , where  $\delta$  denotes the O content.

Fig. 6.2 a) shows the Fe 3p, Co 3p and O 2s spectra of all prepared cobalt ferrite films. Reference spectra of CoO and  $Fe_2O_3$  films are included for comparison. All spectra have been calibrated according to the C 1s core-level at 285 eV binding energy.

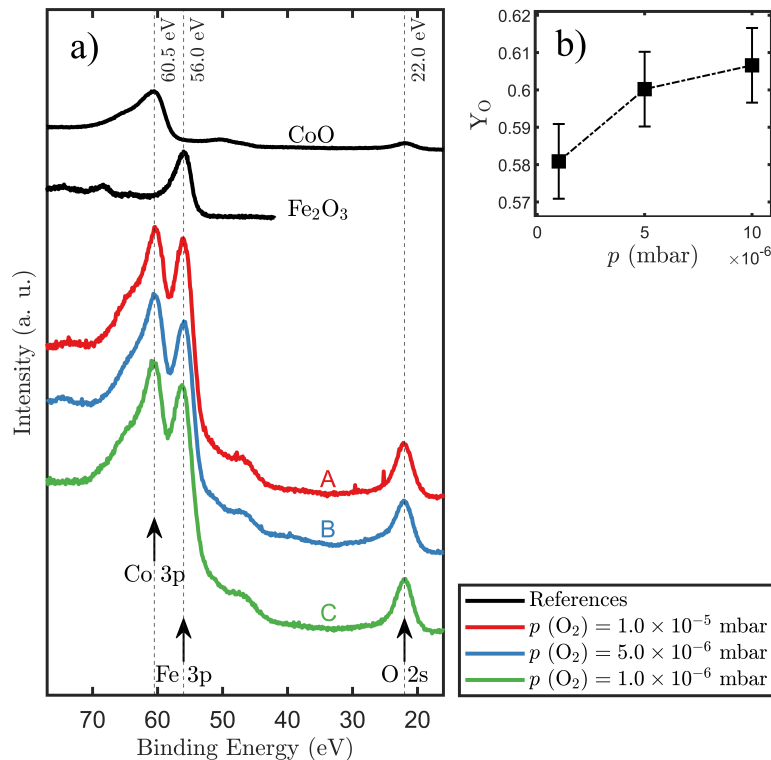


**Figure 6.2:** Fe 3p, Co 3p and O 2s core-level XP spectra of cobalt ferrite films prepared via RMBE at different oxygen partial pressures. Reference spectra of common oxides are shown in black.

The binding energies of the Co 3p and Fe 3p XP peaks are  $(60.5 \pm 0.2)$  eV and  $(56.0 \pm 0.2)$  eV, respectively, and thus agree with the values determined in Sec. 5.1.1. The spectra show no significant change depending on the oxygen pressure. The O 2s XP signal is localized at a binding energy of  $(22.0 \pm 0.2)$  eV and the peak intensity does not increase significantly with varying reactive  $O_2$  atmosphere. In order to exactly determine the O content  $\delta$  relative to the Fe and Co content, the

intensity ratio

$$Y_O = \frac{I_O^{2s}/\sigma_O^{2s}}{I_O^{2s}/\sigma_O^{2s} + I_{Co}^{3p}/\sigma_{Co}^{3p} + I_{Fe}^{3p}/\sigma_{Fe}^{3p}}, \quad (6.2)$$

is considered.  $Y_O$  increases with increasing oxygen pressure (cf. Fig. 6.2 b)).  $Y_O$  is about 0.58 for Sample C. This value increases with increasing  $O_2$  pressure to as much as 0.61 for Sample A. From  $Y_O$ ,  $\delta$  can be determined. For samples A, B and C, values of 4.3, 4.2 and 4.1 are obtained. The uncertainty in  $\delta$  is estimated to be 0.2. As expected, the O content  $\delta$  of the cobalt ferrite ultrathin films increases with increasing  $O_2$  pressure.

Fig. 6.3 shows the Fe 2p and Co 2p XP spectra of all prepared cobalt ferrite films. Reference spectra of the most common related oxides are shown in black. All spectra have been calibrated according to the C 1s core-level at 285 eV binding energy.

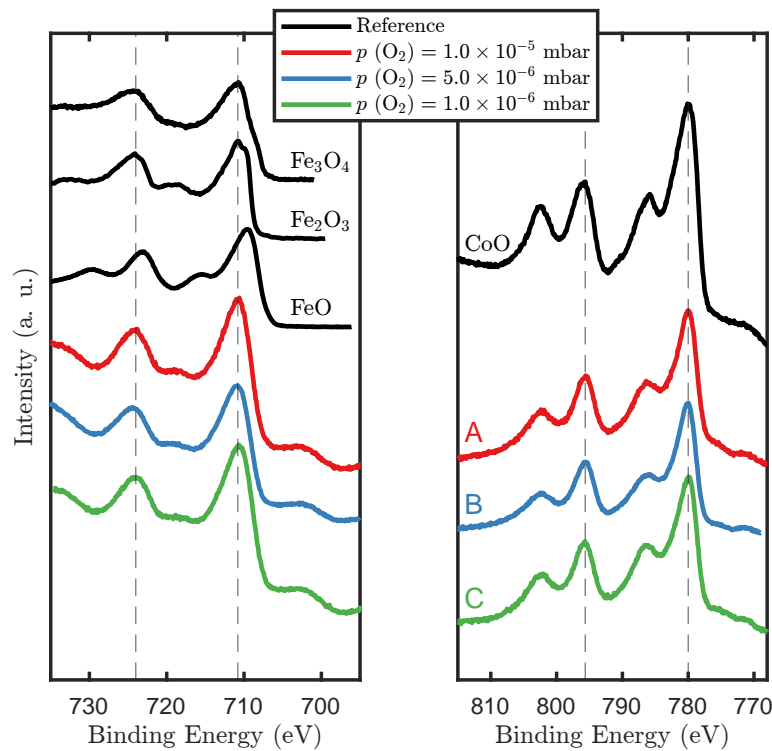


**Figure 6.3:** Fe 2p and Co 2p core-level XP spectra of cobalt ferrite films prepared via RMBE at different oxygen partial pressures. Reference spectra of common oxides are shown in black. The dashed lines indicate the respective main peaks 2p  $3/2$  and 2p  $1/2$ .

The binding energies of the Fe  $2p_{3/2}$  and Fe  $2p_{1/2}$  peaks are  $(710.6 \pm 0.2)$  eV and  $(724.2 \pm 0.2)$  eV, respectively. In addition, a charge-transfer satellites are located at  $(718.4 \pm 0.4)$  eV can be observed. Another charge-transfer satellite should be localized at the high binding energy side of the Fe 2p  $1/2$  peak which, however, is overlapped with the Auger O KLL line. The shape of the spectra and the peak positions are characteristic for trivalent iron, which is expected for cobalt ferrite [39]. A significant change in the peak positions or in the shape of the spectra with increasing oxygen pressure is not observed and also not expected due to the same Fe content in the films.

The Co 2p spectra also show the characteristic shape for cobalt ferrite with predominant  $Co^{2+}$  cations.

The Co  $2p_{3/2}$  and Co  $2p_{1/2}$  main peaks are located at binding energies of  $(780.0 \pm 0.2)$  eV and  $(795.6 \pm 0.2)$  eV, respectively. The associated shake-up satellites are located at  $(786.5 \pm 0.2)$  eV and  $(802.4 \pm 0.2)$  eV. No significant change in the spectra can be observed with increasing oxygen pressure since the Co content in the films is unchanged.

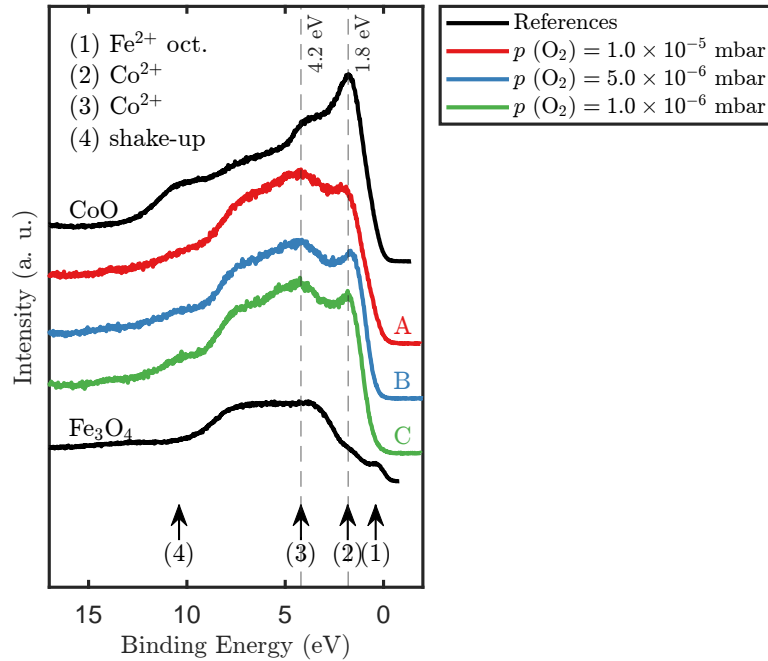


**Figure 6.4:** Valence band XP spectra of the cobalt ferrite films prepared via RMBE at different oxygen partial pressures. Reference spectra of CoO and  $Fe_3O_4$  are shown in black.

Fig. 6.4 shows the XP valence band (VB) spectrum of samples A, B and C and the VB spectra of a CoO and  $Fe_3O_4$  sample as reference. All spectra have been calibrated according to the C 1s core level at 285 eV.

Feature (1), positioned at a binding energy of about  $(0.4 \pm 0.1)$  eV, is only observed in the  $Fe_3O_4$  spectrum. It is suggested that this peak is linked to the existence of  $Fe^{2+}$  cations at octahedral B-sites [33]. From Sec. 5.1.4 it is known that feature (1) is only seen for cobalt ferrite samples with  $x < 1$ . Samples A, B and C do not show feature (1) as they are superstoichiometric. Furthermore, feature (2) and (3) are clearly visible. According to Chuang [5] and Kim [21], these features are due to 3d electrons emitted from divalent Co. Since the stoichiometry of the samples is constant, the amount of divalent Co is the same in all samples and therefore the size of feature (2) and (3) does not change significantly. Furthermore, feature (4), which is due to a shake-up process ( $O 2p \rightarrow Co 3d$ ) [21], is observed. This peak is barely variable with varying pressure. The valence band is superimposed by a broad O 2p XP peak ranging from 2 eV to about 8 eV [33]. However, no significant change in the VB can be observed as the O content increases. One possible reason could be that the photoionization cross section  $\sigma$  of O is very small compared to the cross section of Co and Fe. Hence, the O 2p intensity is very small compared to the dominant Fe 3d and Co 3d XP intensity.



## 6.2 LEED results

Fig. 6.5 shows the LEED patterns acquired at an electron energy of 200 eV for the cobalt ferrite ultra-thin films prepared at varying  $O_2$  reactive atmospheres. All patterns show a  $(1 \times 1)$  surface structure (blue), which arises from the cubic spinel structure of cobalt ferrite. The underlying cubic surface structure is shown in red for comparison. It is apparent that the background intensity decreases with increasing oxygen pressure and it also appears that the LEED spots become more contrasting with increasing oxygen pressure. Both observations indicate that the crystalline surface becomes better ordered and less defective with increasing oxygen pressure. This finding is quantified by analyzing the FWHM of a chosen LEED spot as a function of oxygen partial pressure. The FWHM of the investigated  $(\bar{2}2)$  spot decreases with increasing pressure (cf. Fig. 6.6), which confirms quantitatively that the ordering of the surface structure improves as the oxygen pressure increases.

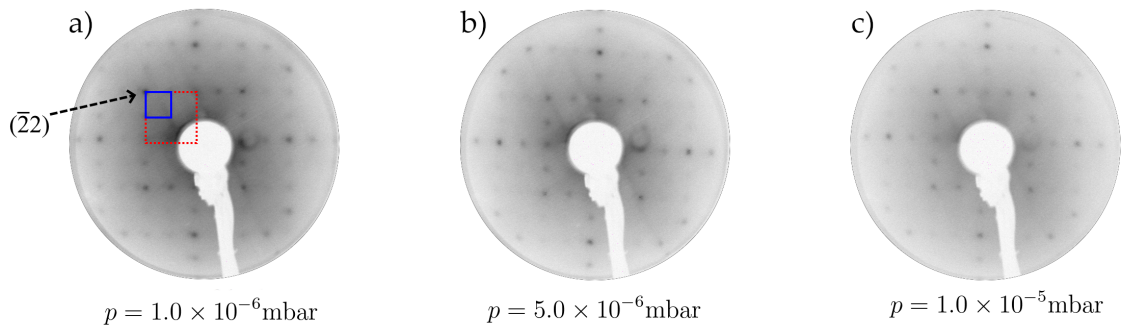


**Figure 6.5:** LEED patterns of CFO/MgO(001) samples prepared at varying diluted oxygen atmospheres during RMBE. The cubic unit cell of CFO is shown in blue and the unit cell of MgO is, for comparison, shown in red.

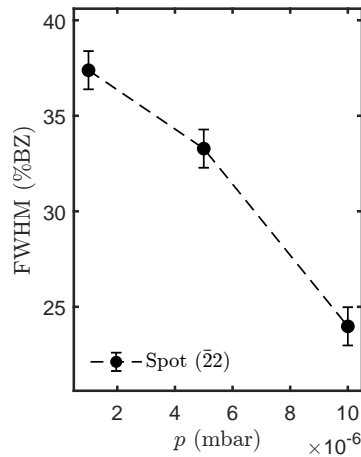


**Figure 6.6:** FWHM of the intensity profile of the  $(\bar{2}2)$  spot as a function of pressure  $p$  during RMBE. The FWHM is normalized to the first Brillouin zone.

### 6.3 XRR results

The film thicknesses are determined by XRR measurements in  $\theta - 2\theta$  geometry. Fig. 6.7 shows the measured reflected intensity as a function of the scattering vector  $q$ . Kiessig fringes due to constructive and destructive interference are clearly visible. The shapes of the XRR curves suggest that all films are monolayer systems. The distances of adjacent local minima or maxima are nearly the same for all samples, implying that all film thicknesses are in the same order of magnitude.

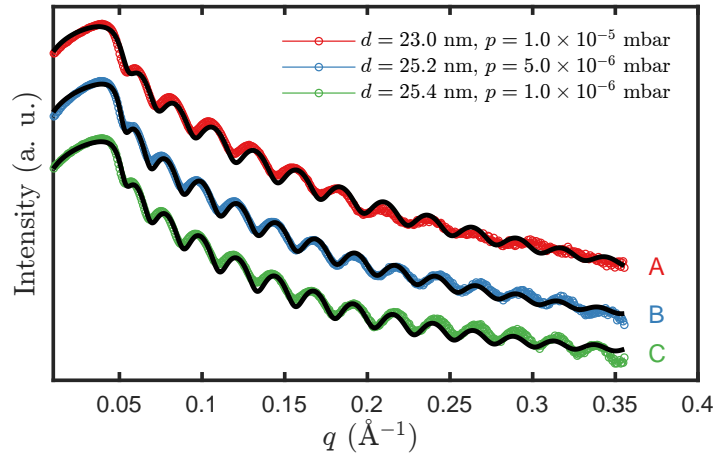


**Figure 6.7:** XRR measurement of the cobalt ferrite samples prepared under varying pressures ( $1 \times 10^{-5}$  mbar,  $5 \times 10^{-6}$  mbar,  $1 \times 10^{-6}$  mbar). The intensity curve suggests a monolayer system. The reconstructed intensity curves are shown in black.

It is noticeable that the fringes of sample A, which was prepared under the highest diluted oxygen atmosphere of  $1.0 \times 10^{-5}$  mbar, are significantly more damped than the samples prepared at lower pressures. This suggests a higher surface roughness and a higher surface disorder for sample A. This result contradicts the results from the LEED spot analysis and reasons for this are unclear. For the exact determination of the film thickness, the measured intensity is fitted using the iXRR software [1]. All cobalt ferrite films have film thicknesses of  $(24.2 \pm 1.2)$  nm.

### 6.4 UV-Vis results

The direct and indirect band gaps of the cobalt ferrite samples prepared under varying diluted oxygen atmospheres are determined using UV-Vis spectroscopy and Tauc plots. The exact approach is already discussed in Sec. 2.5.2 and 5.4, therefore only the relevant results are presented here. However, it should be mentioned that again only allowed transitions are evaluated.

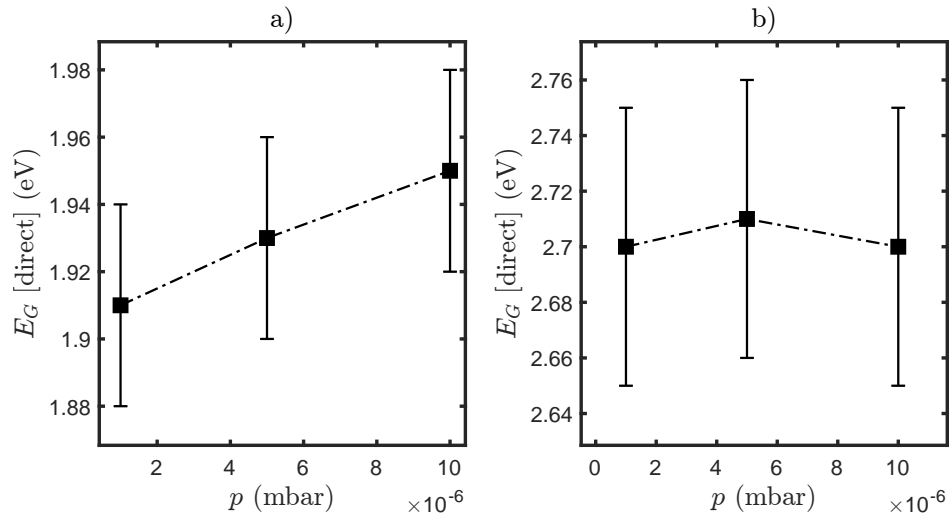


**Figure 6.8:** Direct band gaps of thin cobalt ferrite samples prepared under varying diluted oxygen atmospheres. The Tauc plot (not included) reveal two linear regions, hence, two possible direct band gaps.

Fig. 6.8 a) and b) show the direct band gap of all prepared cobalt ferrite thin films as a function of the oxygen pressure  $p$ . The Tauc plots for the determination of the direct band gap again reveal two linear regions, which is why both regions are approximated with a linear fit function. The first determined direct band gap (Fig. 6.8 a)) ranges from  $(1.91 \pm 0.03)$  eV to  $(1.95 \pm 0.03)$  eV. It increases continuously with increasing pressure. The second band gap (Fig. 6.8 b)) has a value of about  $(2.70 \pm 0.05)$  eV and does not change significantly with varying pressure. The band gaps are comparable to the values determined in Sec. 5.4.1.

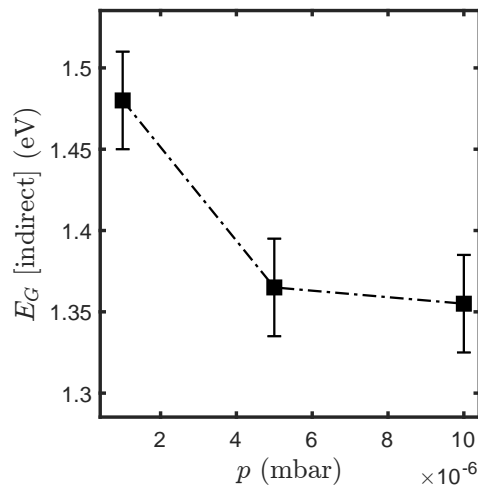


**Figure 6.9:** First indirect band gaps of  $\text{Co}_{1.3}\text{Fe}_{1.7}\text{O}_4$  as a function of the oxygen pressure during RMBE

The indirect band gap (cf. Fig. 6.9) for the cobalt ferrite thin film prepared at an oxygen pressure of  $1.0 \times 10^{-6}$  mbar is  $(1.48 \pm 0.03)$  eV, which is consistent with the results from Sec. 5.4.1. However, the indirect band gap decreases significantly as the pressure increases. At a pressure of  $5.0 \times 10^{-6}$  mbar the band gap is only  $(1.37 \pm 0.03)$  eV and at an even higher pressure of  $1.0 \times 10^{-5}$  mbar the indirect band gap drops to  $(1.36 \pm 0.03)$  eV.

## 6.5 Temperature dependent sheet resistivity

The sheet resistivities  $\rho$  as a function of temperature  $T$  of samples B and C are determined using the van der Pauw method (cf. Fig. 6.10 a)). Sample A, the sample prepared under the highest oxygen pressure of  $1.0 \times 10^{-5}$  mbar, could not be measured because the films's resistivity is too high for the given experimental setup. The sheet resistivities were measured from 304 K to 343 K. Compared to the measurement from Sec. 5.5, the temperature interval was reduced because the resistivities of the samples were too high for temperatures lower than 304 K and could not be measured with the given setup.

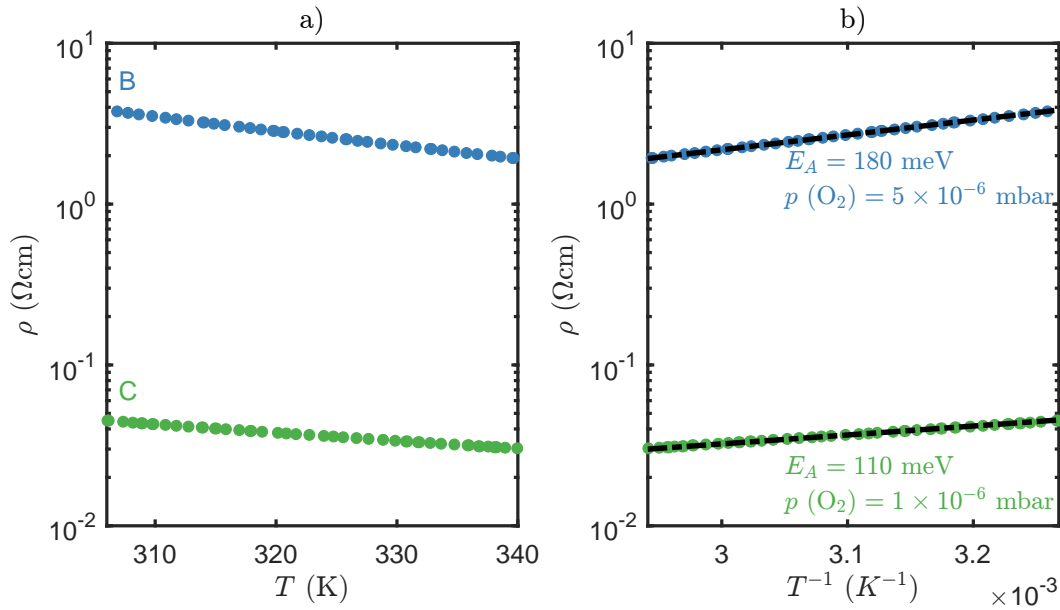


**Figure 6.10:** Temperature dependence of the electrical resistivity. In a) the resistivity  $\log \rho$  is plotted against the temperature  $T$  and in b)  $\log \rho$  is plotted against  $1/T$  to determine the activation energy  $E_A$  in an Arrhenius plot.

As expected for cobalt ferrite, samples B and C show a semiconducting behaviour, since the sheet resistivity decreases exponentially with increasing temperature. Furthermore, the resistivity increases with increasing oxygen pressure  $p$ . A similar result has been reported for  $\text{NiFe}_2\text{O}_x$  thin films on  $\text{MgAl}_2\text{O}_4$  [3]. In Sec. 5.5 it was already mentioned that the conductivity in ferrites is mainly attributed to electron hopping from  $\text{Fe}^{3+}$  to  $\text{Fe}^{2+}$  [51]. It could be the case that due to a higher oxygen pressure more iron is oxidized on the surface and these iron atoms are therefore no longer available for a hopping process. This would lead to an increase in resistivity.

Using a simple Arrhenius plot (cf. Fig. 6.10 b)), the thermal activation energy  $E_A$  of the charge carriers can be determined. Plotting  $\rho$  vs.  $T^{-1}$ , the activation energy can be determined by the slope of a linear regression. The thermal activation energy for sample B is determined to be 180 meV and for sample C the activation energy is 110 meV. These values are comparable to the values determined in Sec. 5.5.

## 7. Summary and outlook

The aim of this thesis is to investigate the electronic, optical and transport properties of ultrathin cobalt ferrite films on MgO(001), depending on the amount of Co and the amount of O, in order to enhance the performance of cobalt ferrite for thin applications as spin-filters. All samples studied in this thesis are fabricated by RMBE. Soft-XPS is used to investigate the electronic structure and to determine the surface stoichiometry. The structure and ordering of the surfaces are analyzed by LEED. XRR is mainly used to measure the film thickness. Optical properties, in particular the direct and indirect optical band gaps, are investigated by UV-Vis spectroscopy and Tauc plots. Electrical transport properties such as resistivity are measured as a function of temperature using the van der Pauw method.

### Properties of ultra thin $\text{Co}_x\text{Fe}_{3-x}\text{O}_4$ films on MgO(001)

In the first part of this thesis,  $\text{Co}_x\text{Fe}_{3-x}\text{O}_4$  ( $0.6 \leq x \leq 1.8$ ) films with a thickness of about 20 nm are prepared using RMBE. The physical properties of the samples are studied as a function of  $x$ .

The stoichiometry is determined from the intensities of the Fe 3p and Co 3p XP peaks. The Fe XP peaks (3p, 2p) shrink with increasing  $x$  and the Co peaks (3p, 2p) grow with increasing  $x$  due to the varying amount of Co in the  $\text{Co}_x\text{Fe}_{3-x}\text{O}_4$  thin films. Based on the Fe 2p and Co 2p spectra, it can be concluded that the predominant oxidation state of Fe and Co is  $\text{Fe}^{3+}$  and  $\text{Co}^{2+}$ , respectively. The general shape of the spectra as well as the binding energies of the 3p and 2p peaks of Fe and Co, respectively, do not change with varying Co content. All  $\text{Co}_x\text{Fe}_{3-x}\text{O}_4/\text{MgO}(001)$  films grow (001)-orientated and exhibit a  $(1 \times 1)$  surface structure. The crystalline quality of the surface decreases with increasing Co content  $x$ . Using the Tauc method, two direct optical band gaps with an energy of about 1.9 eV and 2.6 eV were determined. Both direct band gaps increase with increasing  $x$ . In contrast, an indirect band gap of about 1.5 eV is determined, which decreases almost linearly with increasing  $x$ . The van der Pauw measurement reveals that all  $\text{Co}_x\text{Fe}_{3-x}\text{O}_4$  films show semiconducting behaviour. The resistivity increases exponentially with decreasing temperature and also increases as  $x$  increases. By analyzing the data in an Arrhenius plot, the thermal activation energies are determined. Here, activation energies ranging 67 meV ( $x = 0.6$ ) to 123 meV ( $x = 1.1$ ) are obtained.

### **Influence of oxygen partial pressure during RMBE on CFO properties**

In the second part of this thesis, cobalt ferrite ultrathin films are grown on MgO(001) by RMBE, varying the oxygen pressure during evaporation and thus, varying the O content in the films. Three samples with a thickness of about 25 nm are prepared at pressures of  $1.0 \times 10^{-5}$  mbar,  $5.0 \times 10^{-6}$  mbar and  $1.0 \times 10^{-6}$  mbar. Based on the LEED results, epitaxial and crystalline growth can be assumed. All films grow (001)-orientated and show a  $(1 \times 1)$  superstructure, as expected for cobalt ferrite. The quality of the surface structure increases with increasing pressure. The Fe (2p, 3p), Co (2p, 3p) and valence band XP spectra have no significant dependence on the oxygen amount. The shape and position of the Fe 2p and Co 2p main peaks are characteristic of cobalt ferrite as Fe is predominantly in the trivalent oxidation state and Co is predominantly in the divalent oxidation state. Using the Tauc method, two direct optical band gaps are determined. The first direct band gap of about 1.9 eV increases almost linearly with increasing O<sub>2</sub> pressure and the second direct band gap of about 2.7 eV does not change significantly with varying pressure. The indirect band gap for the sample prepared at  $1.0 \times 10^{-6}$  mbar is about 1.48 eV, which decreases as the oxygen partial pressure increases. Conductivity measurements reveal that all samples exhibit semiconducting behaviour. The resistivity increases strongly with as the pressure is increased. By analyzing the data in an Arrhenius plot, the thermal activation energies can be determined. Activation energies from 110 meV to 180 meV are obtained.

### **Outlook**

In this work, electronic, optical and transport properties of ultrathin cobalt ferrite films on MgO(001) have been successfully investigated as a function of stoichiometry and oxygen content, respectively. However, magnetic properties have not been investigated so far. A further study could answer the question to what extent the Co content or the O content in ultrathin cobalt ferrite films influences the magnetic properties such as the magnetization curve, coercivity or remanence. For this purpose, a VSM (vibrating sample magnetometry) measurement or a SQUID (superconducting quantum interference device) measurement would be suitable.

In addition, some studies on cobalt ferrite show that the cation distribution between the octahedral and tetrahedral sites have significant influence on the physical properties. For this reason, in order to better interpret the results presented in this work, it is absolutely necessary to investigate the samples structurally. For example, the distribution of the cations among A and B sites could be analyzed using XMCD (X-ray magnetic circular dichroism) or Mössbauer spectroscopy.

## Bibliography

- [1] F. Bertram. *Röntgenreflektometrie an ultra dünnen Schichten*. 2007.
- [2] A. E. Bocquet et al. “Electronic structure of 3d-transition-metal compounds by analysis of the 2p core-level photoemission spectra”. In: *Phys. Rev. B* 46 (7 1992), pp. 3771–3784. DOI: 10.1103/PhysRevB.46.3771.
- [3] P. Bougiatioti et al. “Electrical transport and optical band gap of NiFe<sub>2</sub>O<sub>x</sub> thin films”. In: *Journal of Applied Physics* 122.22 (2017). DOI: 10.1063/1.4999428.
- [4] R. Buß. *Studies on the Epitaxial Growth of Ultrathin Metal Oxide Films*. 2015.
- [5] T. J. Chuang et al. “Interpretation of the x-ray photoemission spectra of cobalt oxides and cobalt oxide surfaces”. In: *Surface Science* 59.2 (1976), pp. 413–429. DOI: [https://doi.org/10.1016/0039-6028\(76\)90026-1](https://doi.org/10.1016/0039-6028(76)90026-1).
- [6] J. B. Coulter et al. “Assessing Tauc Plot Slope Quantification: ZnO Thin Films as a Model System”. In: *physica status solidi (b)* 255.3 (2018), p. 1700393. DOI: <https://doi.org/10.1002/pssb.201700393>.
- [7] R. S. Devan et al. “Effect of cobalt substitution on the properties of nickel–copper ferrite”. In: *Journal of Physics: Condensed Matter* 18.43 (2006), pp. 9809–9821. DOI: 10.1088/0953-8984/18/43/004.
- [8] P. Durga Prasad and J. Hemalatha. “Enhanced magnetic properties of highly crystalline cobalt ferrite fibers and their application as gas sensors”. In: *Journal of Magnetism and Magnetic Materials* 484 (2019), pp. 225–233. ISSN: 0304-8853. DOI: <https://doi.org/10.1016/j.jmmm.2019.04.026>.
- [9] Jaroslav Fabian et al. “Spintronics: Fundamentals and applications”. In: *Rev. Mod. Phys.* 76 (2 2004), pp. 323–410. DOI: 10.1103/RevModPhys.76.323.
- [10] M. Furlan. “Electronic transport and the localization length in the quantum Hall effect”. In: *Phys. Rev. B* 57 (23 1998), pp. 14818–14828. DOI: 10.1103/PhysRevB.57.14818.
- [11] V. F. Gantmakher et al. *Electrons and Disorder in Solids*. International Series of Monographs on Physics. OUP Oxford, 2005. ISBN: 9780198567561.
- [12] R. Gross et al. *Festkörperphysik*. De Gruyter Oldenbourg, 2014. DOI: <https://doi.org/10.1524/9783110358704>.
- [13] W. M. Haynes. *CRC Handbook of Chemistry and Physics*. CRC Press, 2011.
- [14] P. Heide. *X-ray Photoelectron Spectroscopy - An introduction to Principles and Practices*. New York: John Wiley and Sons, 2011. ISBN: 978-1-118-16290-3.
- [15] O.M. Hemedda et al. “Effect of hopping rate and jump length of hopping electrons on the conductivity and dielectric properties of CoCd ferrite”. In: *Journal of Magnetism and Magnetic*

- Materials* 223.2 (2001), pp. 127–132. ISSN: 0304-8853. DOI: 10.1016/S0304-8853(00)00521-7.
- [16] B. L. Henke et al. “X-Ray Interactions: Photoabsorption, Scattering, Transmission, and Reflection at  $E = 50 - 30000$  eV,  $Z = 1 - 92$ ”. In: *Atomic Data and Nuclear Data Tables* 54.2 (1993), pp. 181–342. ISSN: 0092-640X. DOI: <https://doi.org/10.1006/adnd.1993.1013>.
- [17] S. Heo et al. “Band gap and defect states of MgO thin films investigated using reflection electron energy loss spectroscopy”. In: (2015).
- [18] R. J. Hill et al. “Systematics of the spinel structure type”. In: *Physics and Chemistry of Minerals* 4.4 (1979), pp. 317–339. DOI: 10.1007/bf00307535.
- [19] C. Himcinschi et al. “Optical and magneto-optical study of nickel and cobalt ferrite epitaxial thin films and submicron structures”. In: *Journal of Applied Physics* 113.8 (2013), p. 084101. DOI: 10.1063/1.4792749.
- [20] G. H. Jonker. “Analysis of the semiconducting properties of cobalt ferrite”. In: *Journal of Physics and Chemistry of Solids* 9.2 (1959), pp. 165–175. ISSN: 0022-3697. DOI: [https://doi.org/10.1016/0022-3697\(59\)90206-9](https://doi.org/10.1016/0022-3697(59)90206-9).
- [21] K. S. Kim. “X-ray-photoelectron spectroscopic studies of the electronic structure of CoO”. In: *Phys. Rev. B* 11 (6 1975), pp. 2177–2185. DOI: 10.1103/PhysRevB.11.2177.
- [22] S. J. Kim et al. “Mössbauer Studies on Exchange Interactions in  $\text{CoFe}_2\text{O}_4$ ”. In: *Japanese Journal of Applied Physics* (2001).
- [23] O. Kuschel. *From initial growth of ultrathin  $\text{Fe}_3\text{O}_4$  films up to  $\text{NiFe}_2\text{O}_4$  formation through interdiffusion of  $\text{Fe}_3\text{O}_4/\text{NiO}$  bilayers on  $\text{Nb:SrTiO}_3(001)$* . 2020.
- [24] H. Le Trong et al. “Mössbauer characterisations and magnetic properties of iron cobaltites  $\text{Co}_x\text{Fe}_{3-x}\text{O}_4$  ( $1 \leq x \leq 2.46$ ) before and after spinodal decomposition”. In: *Journal of Magnetism and Magnetic Materials* 334 (2013), pp. 66–73. ISSN: 0304-8853. DOI: 10.1016/j.jmmm.2013.01.007.
- [25] S. Matzen et al. “Nanomagnetism of cobalt ferrite-based spin filters probed by spin-polarized tunneling”. In: *Applied Physics Letters* 101.4 (2012), p. 042409. DOI: 10.1063/1.4738790.
- [26] S. A. Mazen et al. “Studies on micro-structure and dc conductivity of polycrystalline  $\text{Li}_{0.5+0.5x}\text{Si}_x\text{Fe}_{2.5-1.5x}\text{O}_4$  spinel ferrites”. In: *Powder Technology* 317 (2017), pp. 339–347. ISSN: 0032-5910. DOI: <https://doi.org/10.1016/j.powtec.2017.05.011>.
- [27] N. S. McIntyre et al. “X-ray photoelectron spectroscopic studies of iron oxides”. In: *Analytical Chemistry* 49.11 (1977), pp. 1521–1529. DOI: 10.1021/ac50019a016.
- [28] N. F. Mott et al. *Electronic Processes in Non-Crystalline Materials* -. New York, London: OUP Oxford, 2012. ISBN: 978-0-199-64533-6.
- [29] J. Moussy. “From epitaxial growth of ferrite thin films to spin-polarized tunnelling”. In: *Journal of Physics D: Applied Physics* 46.14 (2013), p. 143001. DOI: 10.1088/0022-3727/46/14/143001.
- [30] J. Newberg et al. “Formation of hydroxyl and water layers on MgO films studied with ambient pressure XPS”. In: *Surface Science* 605 (Jan. 2011), pp. 89–94. DOI: 10.1016/j.susc.2010.10.004.
- [31] I. C. Nlebedim et al. “Non-stoichiometric cobalt ferrite,  $\text{Co}_x\text{Fe}_{3-x}\text{O}_4$  ( $x = 1.0$  to  $2.0$ ): Structural, magnetic and magnetoelastic properties”. In: *Journal of Magnetism and Magnetic Materials*



- 343 (2013), pp. 49–54. ISSN: 0304-8853. DOI: <https://doi.org/10.1016/j.jmmm.2013.04.063>.
- [32] K. Oura et al. *Surface Science - An Introduction*. Berlin Heidelberg: Springer Science & Business Media, 2013. ISBN: 978-3-662-05179-5.
- [33] Markus Christian Paul. “Molecular beam epitaxy and properties of magnetite thin films on semiconducting substrates”. doctoralthesis. Universität Würzburg, 2010.
- [34] L. J. van der Pauw. “A method of measuring specific resistivity and Hall effect of discs of arbitrary shape”. In: *Semiconductor Devices: Pioneering Papers*, pp. 174–182. DOI: 10.1142/9789814503464\_0017.
- [35] R. C. Rai et al. “Optical and electronic properties of NiFe<sub>2</sub>O<sub>4</sub> and CoFe<sub>2</sub>O<sub>4</sub> thin films”. In: *Applied Physics A* 106.1 (Aug. 2011), pp. 207–211. DOI: 10.1007/s00339-011-6549-z.
- [36] A. V. Ramos et al. “Room temperature spin filtering in epitaxial cobalt-ferrite tunnel barriers”. In: *Applied Physics Letters* 91.12 (2007), p. 122107. DOI: 10.1063/1.2787880.
- [37] A. V. Ravindra et al. “Electronic structure and optical band gap of CoFe<sub>2</sub>O<sub>4</sub> thin films”. In: *Applied Physics Letters* 101.16 (2012), p. 161902. DOI: 10.1063/1.4759001.
- [38] J. Rodewald. “Advancement of growth and characteristics of ultrathin ferrite films”. doctoralthesis. Universität Osnabrück, 2020.
- [39] J. Rodewald et al. “Formation of ultrathin cobalt ferrite films by interdiffusion of Fe<sub>3</sub>O<sub>4</sub>/CoO bilayers”. In: *Phys. Rev. B* 100 (15 2019), p. 155418. DOI: 10.1103/PhysRevB.100.155418.
- [40] D. M. Roessler and W. C. Walker. “Electronic Spectrum and Ultraviolet Optical Properties of Crystalline MgO”. In: *Physical Review* (1967).
- [41] K. Ruwisch. *Charakterisierung des Exchange Bias-Systems Fe<sub>3</sub>O<sub>4</sub>/CoO mit SQUID und VSM*. 2018.
- [42] J. H. Scofield. “Hartree-Slater subshell photoionization cross-sections at 1254 and 1487 eV”. In: *Journal of Electron Spectroscopy and Related Phenomena* 8.2 (1976), pp. 129–137. ISSN: 0368-2048. DOI: [https://doi.org/10.1016/0368-2048\(76\)80015-1](https://doi.org/10.1016/0368-2048(76)80015-1).
- [43] Hamed Sharifi Dehsari and Kamal Asadi. “Impact of Stoichiometry and Size on the Magnetic Properties of Cobalt Ferrite Nanoparticles”. In: *The Journal of Physical Chemistry C* 122.51 (2018), pp. 29106–29121. DOI: 10.1021/acs.jpcc.8b09276.
- [44] D. Sharma et al. “Tailoring the optical bandgap and magnetization of cobalt ferrite thin films through controlled zinc doping”. In: *AIP Advances* 6.8 (2016), p. 085005. DOI: 10.1063/1.4960989.
- [45] D. Sharma et al. “Tuning of optical bandgap and magnetization of CoFe<sub>2</sub>O<sub>4</sub> thin films”. In: *Applied Physics Letters* 105.3 (2014), p. 032404. DOI: 10.1063/1.4890863.
- [46] A. B. Shinde et al. “Structural and Electrical Properties of Cobalt Ferrite Nanoparticles”. In: *International Journal of Innovative Technology and Exploring Engineering* (2013).
- [47] D. A. Shirley. “High-Resolution X-Ray Photoemission Spectrum of the Valence Bands of Gold”. In: *Phys. Rev. B* 5 (12 1972), pp. 4709–4714. DOI: 10.1103/PhysRevB.5.4709.
- [48] B. I. Shklovskii et al. *Electronic Properties of Doped Semiconductors*. Berlin Heidelberg: Springer Science and Business Media, 2013. ISBN: 978-3-662-02403-4.

- [49] K. E. Sickafus et al. “Structure of Spinel”. In: *Journal of the American Ceramic Society* 82.12 (1999), pp. 3279–3292. DOI: <https://doi.org/10.1111/j.1151-2916.1999.tb02241.x>.
- [50] L. Spieß et al. *Moderne Röntgenbeugung: Röntgendiffraktometrie für Materialwissenschaftler, Physiker und Chemiker*. Vieweg Teubner Verlag / GWV Fachverlage GmbH, Wiesbaden, 2009.
- [51] R. Srivastava et al. “Ferrite Materials: Introduction, Synthesis Techniques, and Applications as Sensors”. In: *International Journal of Green Nanotechnology* 4.2 (2012), pp. 141–154. DOI: [10.1080/19430892.2012.676918](https://doi.org/10.1080/19430892.2012.676918).
- [52] S. Tanuma et al. “Calculation of electron inelastic mean free paths (IMFPs) VII. Reliability of the TPP-2M IMFP predictive equation”. In: *Surface and Interface Analysis* 35.3 (2003), pp. 268–275. DOI: <https://doi.org/10.1002/sia.1526>.
- [53] J. Tauc. “Optical properties and electronic structure of amorphous Ge and Si”. In: *Materials Research Bulletin* 3.1 (1968), pp. 37–46. ISSN: 0025-5408. DOI: [https://doi.org/10.1016/0025-5408\(68\)90023-8](https://doi.org/10.1016/0025-5408(68)90023-8).
- [54] J. Thien. *Bildung und Charakterisierung von Cobaltferritschichten durch Interdiffusion von Cobaltoxid- und Magnetitschichten*. 2017.
- [55] J. Thien and others. “Effects of Post-deposition Annealing on Epitaxial CoO/Fe<sub>3</sub>O<sub>4</sub> Bilayers on SrTiO<sub>3</sub>(001) and Formation of Thin High-Quality Cobalt Ferrite-like Films”. In: *The Journal of Physical Chemistry C* 124.43 (2020), pp. 23895–23904. DOI: [10.1021/acs.jpcc.0c05503](https://doi.org/10.1021/acs.jpcc.0c05503).
- [56] S. Tougaard et al. “Test of algorithm for background correction in XPS under variation of XPS peak energy”. In: *Surface and Interface Analysis* 13.4 (1988), pp. 225–227. DOI: <https://doi.org/10.1002/sia.740130409>.
- [57] F. Urbach. “The Long-Wavelength Edge of Photographic Sensitivity and of the Electronic Absorption of Solids”. In: *Phys. Rev.* 92 (5 1953), pp. 1324–1324. DOI: [10.1103/PhysRev.92.1324](https://doi.org/10.1103/PhysRev.92.1324).
- [58] T. Yamashita et al. “Analysis of XPS spectra of Fe<sup>2+</sup> and Fe<sup>3+</sup> ions in oxide materials”. In: *Applied Surface Science* 254.8 (2008), pp. 2441–2449. ISSN: 0169-4332. DOI: <https://doi.org/10.1016/j.apsusc.2007.09.063>.
- [59] A. Yildiz et al. “Crossover from Nearest-Neighbor Hopping Conduction to Efros–Shklovskii Variable-Range Hopping Conduction in Hydrogenated Amorphous Silicon Films”. In: 48.11 (2009), p. 111203. DOI: [10.1143/jjap.48.111203](https://doi.org/10.1143/jjap.48.111203).
- [60] B. Zhou et al. “Correlation between structure and intervalence charge-transfer transitions in nanocrystalline CoFe<sub>2-x</sub>M<sub>x</sub>O<sub>4</sub> (M = Mn, Al, Sc) thin films”. In: *Phys. Rev. B* 68 (2 2003), p. 024426. DOI: [10.1103/PhysRevB.68.024426](https://doi.org/10.1103/PhysRevB.68.024426).

## Erklärung zur selbstständigen Abfassung der Masterarbeit

Name: Sven Berlekamp  
Geburtsdatum: 30.08.1994 in Osnabrück  
Matrikelnummer: 959295  
Titel der Masterarbeit:

*Electronic, optical and transport properties  
of ultrathin cobalt ferrite films on MgO(001)*

Ich versichere, dass ich die eingereichte Masterarbeit selbstständig und ohne erlaubte Hilfe verfasst habe. Anderer als der von mir angegebenen Hilfsmittel und Schriften habe ich mich nicht bedient. Alle wörtlich oder sinngemäß den Schriften anderer Autoren entnommen Stellen habe ich kenntlich gemacht.

Ort, Datum:

---

Unterschrift:

---

